Non-thermal optical engineering of strongly-correlated quantum materials

Thesis by
Junyi Shan

In Partial Fulfillment of the Requirements for the
Degree of
Doctor of Philosophy in Physics

Caltech

CALIFORNIA INSTITUTE OF TECHNOLOGY
Pasadena, California

2022
Defended May 5, 2022

ACKNOWLEDGMENTS

First of all, I would like to thank my adviser David Hsieh. Without his vision and guidance I would not have written this thesis and would not have come to this fruitful final point of my graduate studies.

I would also like to express my deepest gratitude to other members on my thesis committee, including Thomas F. Rosenbaum, Patrick A. Lee, Joseph Falson, and James P. Eisenstein. Their sharp questions during my candidacy exam and our annual meetings helped me refine my science and choose the next steps.

As an experimentalist I am always grateful to all my collaborators, including Leon Balents and Mengxing Ye from University of California, Santa Barbara, Danilo Puggioni and James Rondinelli from Northwestern University, Costel Rotundu and Young Lee from Stanford, Sungmin Lee, Je-Geun Park, Chang Jae Roh, and Tae Won Noh from Seoul National University, and Jong Seok Lee from GIST.

I would also like to thank the Hsieh lab members past and present, including John W. Harter, Liuyan Zhao, Alberto de la Torre, Alon Ron, Nicholas J. Laurita, Kyle L. Seyler, Xinwei Li, Tianwei Tang, Ryo Noguchi, Hao Chu, Tejas Deshpande, Honglie Ning, Chen Li, Omar Mehio, Morgan Foley, Yuchen Han, and Daniel Van Beveren.

Last but not least, I would like to thank Jiarui Li from MIT, Jiaqing Wang and Xinghui Lu from Caltech, Luming Liang from Hong Kong, and Ge Cao from Beijing for being my best collaborators in physics and in life. This thesis is dedicated to them and to my family, Ying Shan, Wenru Zhang, and Bingzhen Shen, to whom I owe everything.

ABSTRACT

This thesis develops multiple optical engineering mechanisms to modulate the electronic, magnetic, and optical properties of strongly-correlated quantum materials, including polar metals, transition metal trichalcogenides, and copper oxides. We established the mechanisms of Floquet engineering and magnon bath engineering, and used optical probes, especially optical nonlinearity, to study the dynamics of these quantum systems.

Strongly-correlated quantum materials host complex interactions between different degrees of freedom, offering a rich phase diagram to explore both in and out of equilibrium. While static tuning methods of the phases have witnessed great success, the emerging optical engineering methods have provided a more versatile platform. For optical engineering, the key to success lies in achieving the desired tuning while suppressing other unwanted effects, such as laser heating.

We used sub-gap optical driving in order to avoid electronic excitation. Therefore, we managed to directly couple to low-energy excitation, or to induce coherent light-matter interactions. In order to elucidate the exact microscopic mechanisms of the optical engineering effects, we performed photon energy-dependent measurements and thorough theoretical analysis. To experimentally access the engineered quantum states, we leveraged various probe techniques, including the symmetry-sensitive optical second harmonic generation (SHG), and performed pump-probe type experiments to study the dynamics of quantum materials.

I will first introduce the background and the motivation of this thesis, with an emphasis on the principles of optical engineering within the big picture of achieving quantum material properties on demand (Chapter I). I will then continue to introduce the main probe technique used in this thesis: SHG. I will also introduce the experimental setups which we developed and where we conducted the works contained in this thesis (Chapter II). In Chapter III, I will introduce an often overlooked aspect of SHG studies – using SHG to study short-range structural correlations. Chapter IV will contain the theoretical analysis and experimental realizations of using sub-gap and resonant optical driving to tune electronic and optical properties of $MnPS_3$. The main tuning mechanism used in this chapter is Floquet engineering, where light modulates material properties without being absorbed. In Chapter V, I will turn to another useful material property: magnetism. First I will describe the extension of

the Floquet mechanism to the renormalization of spin exchange interaction. Then I will switch gears and describe the demagnetization in $Sr_2Cu_3O_4Cl_2$ by resonant coupling between photons and magnons. I will end the thesis with a brief closing remark (Chapter VI).

PUBLISHED CONTENT AND CONTRIBUTIONS

Shan, Jun-Yi, M. Ye, et al. (2021). "Giant modulation of optical nonlinearity by Floquet engineering". In: *Nature* 600, pp. 235–239. DOI: `10.1038/s41586-021-04051-8`.
J.-Y.S. performed the optical measurements, performed the single-ion model-based static and Floquet dynamical calculations, and wrote the paper.

Shan, Jun-Yi, A. de la Torre, et al. (2020). "Evidence for an extended critical fluctuation region above the polar ordering transition in LiOsO$_3$". In: *Physical Review Research* 2, p. 033174. DOI: `10.1103/PhysRevResearch.2.033174`.
J.-Y.S. performed the optical measurements, performed the simplified hyper-polarizable bond model calculations, and wrote the paper.

Laurita, N. J. et al. (2019). "Evidence for the weakly coupled electron mechanism in an Anderson-Blount polar metal". In: *Nature Communications* 10, p. 3217. DOI: `10.1038/s41467-019-11172-2`.
J.-Y.S determined the crystal alignment.

TABLE OF CONTENTS

Pocket Material
   The optical spectrum in Hsieh lab:
   Physics and techniques

LIST OF ILLUSTRATIONS

NOMENCLATURE

(Hyper-)Raman scattering. The scattering process where the scattered light has a photon energy smaller than the fundamental (or SHG for hyper-Raman) photon energy due to the loss of energy to excitations such as phonons.

Curie temperature. The temperature above which ferromagnetic materials become paramagnetic.

Dzyaloshinskii–Moriya interaction. An exchange interaction between spins $\mathbf{S}_i$ and $\mathbf{S}_j$ which has the form $\mathbf{D}_{ij} \cdot (\mathbf{S}_i \times \mathbf{S}_j)$.

Exchange interaction. The interaction between electron spins due to the quantum mechanical effects of identical particles.

Fermi level. The highest energy level occupied by electrons in a material at absolute zero.

Fluence. The energy of a pulse divided by the spot size.

Fundamental frequency. The frequency of the incident light, without any harmonic optical nonlinear processes.

Monochromatic. Containing only one wavelength or frequency.

Mott insulator. Insulating materials due to electron correlations despite being predicted to be metallic by the band theory.

Néel temperature. The temperature above which antiferromagnetic materials become paramagnetic.

Point group. A mathematical group containing all the spatial symmetry operation elements in a crystal.

Population inversion. A state where the excited states have higher electron occupation than the ground state.

Quantum materials. An umbrella term for unconventional materials with strong electronic correlations or orders, nontrivial band topology, or other effects that are true revelations of quantum mechanics.

Quantum phase transition. Phase transitions that occur as a function of a non-thermal tuning parameter.

Scattering plane. The plane spanned by the incident light and the reflected light.

Spin canting. Spins that are not oriented in a collinear way, but are tilted by a small canting angle.

Telescope. Two lenses placed with a distance equal to the sum of the two focal lengths, which is used, e.g., to change the beam size. The beam size ratio after and before the telescope is equal to the focal length of the second length divided by the the focal length of the first lens.

Thermalize. Come into thermal equilibrium.

Chapter 1

INTRODUCTION

1.1 Quantum material properties on demand

The prospects

Part of our job as condensed matter physicists is to discover and to design new phases of matter. Room-temperature superconductors can lead to an energy revolution. Simulating the global warming pattern or the cancer proteins require material platforms that can perform fast computation, classical or quantum. Since the early centuries of chemistry, scientists have successfully synthesized a library of compounds, which never ceased to surprise us with novel properties, from exotic types of magnetism, to strange phases of (or out of) unconventional superconductivity, to the puzzling plateaus in the Hall conductivity, to ultra-thin materials which contain just one layer of atoms. With all this success, however, there are still important mysteries that we cannot answer at this moment. Can we really find suitable topological superconductors for robust quantum computation? Are we able to create room temperature superconductors? Or even, how do we understand the existing high-T_c superconductors and the proximate phases?

Or maybe, can we *do something more* than synthesis, and create new (unheard of) phases of matter while understanding the existing materials simultaneously? At the end of the day, we are limited by what nature gives us, but adding some external stimuli to these natural materials we would have almost infinite possibilities.

This leads to the idea of quantum material properties on demand (Basov, Averitt, and Hsieh, 2017), where one does not have to worry about getting the *correct* material that does the *correct* thing. Alternatively, we get a reasonable material platform to start with, and then smartly design the physical environment where this material lives, to achieve some properties or functions that we desire.

Quantum materials are ideal for completing this task, because they are so complicated. In a traditional solid-state physics class, we learn about how electrons orbiting a lattice of ions form energy bands and how the lattice deforms. However, in quantum materials there exist several comparable energy scales: the kinetic energy of electrons, the spin-orbit coupling, the electronic correlations, and more. The intricate balance between these energy scales determine the states of the lattice,

charge, orbit, and spin degrees of freedom in the system, and a quantum phase transition can happen if one of these energy scales is modified. When the quantum phase transition happens in the right direction, we achieve properties on demand, be it electronic, magnetic, or optical.

The methods

What all condensed matter physicists have witnessed in the past few years is a blooming field where we not only gain insights into existing materials, but also add more and more tuning knobs to the materials to achieve new properties foreign to the materials themselves. This trend is enabled by both a deeper theoretical/computational understanding of the interplay between the various degrees of freedom, and rapid technological developments in lasers, precision control, and microscopy capacities. Before we proceed to the main theme of this thesis, optical engineering methods, I would like to provide below an incomplete list of what scientists have tried for external control of quantum material properties. I will focus on the physics side, while I recommend readers to read the references to have a peek into the amazing techniques which enabled all the progress.

High pressure: All solid-state physics starts from the lattice, which is the periodic arrangements of the atoms. The inter-atomic distance determines how likely electrons can hop between neighboring atoms, therefore determining the Mott physics. The lattice also determines the phonon properties, which can be the driving force of superconductivity. Based on diamond anvil cells, scientists have applied hydrostatic pressure to materials, modulating their lattice. As a result, there have been reports of pressure-induced structural phase transitions, Mott transitions, and even potential room-temperature superconductivity (Drozdov et al., 2015; Snider et al., 2020)[1].

Static electric field: Two-dimensional (2D) materials are on the ascent. For some materials like graphene, scotch tape suffices to cleave monolayers. 2D materials also promise high tunabilities. Bringing in techniques from the semiconductor industry, a gate voltage can be applied to add or extract electrons from the thin film, changing its Fermi level thus its Fermi surface. Electric fields can also serve to break symmetries in 2D materials, allowing previously forbidden effects.

Heterostructuring and twistronics: The easy manipulation of 2D materials also enables heterostructuring, which is placing two different materials on top of each

---

[1]We note that there are concerns about the Snider et al. paper, regarding the data processing and interpretation.

other in order to induce emergent effects. One example is the superconducting proximity effect, where the supercurrent-carrying Copper pairs can enter a nearby normal material. By placing an iron atomic chain on top of a superconducting thin film, researchers have observed the Majorana modes (Nadj-Perge et al., 2014). Along comes the idea of twistronics, where a moiré pattern forms as one stacks two different monolayers or two of the same monolayers with a twisting angle. There has been an explosion of works related to twistronics/moiré in the past few years, including superconductivity in twisted bilayer graphene (Cao et al., 2018) and Wigner crystals realized in heterobilayers (H. Li et al., 2021), which are demonstrations of how uncommon theorized phases of matter can arise from synthetic matter. Combining moiré patterns with the application of static electric fields, researchers have achieved continuous tuning across the Mott transition (T. Li et al., 2021).

Static magnetic field: Magnetic fields are able to reorient the spin directions in magnets, to break the energy bands into discrete Laudau levels, or to suppress superconductivity. Pulsed magnets can generate magnetic fields exceeding 100 T, allowing the access of new phase diagrams and helping to elucidate the answers to old problems, such as the symmetry breaking in the pseudogap phase of cuprates (Chan et al., 2016).

Optical engineering: Light incorporates both the electric and magnetic fields, and light can be viewed both as a particle and a wave. Therefore, light can couple to materials in a plethora of ways. Light can excite phonons, electrons, and magnons, directly or indirectly, via the interaction of materials with the electric or the magnetic field within a light beam. Light can also change material properties without exciting anything (Floquet engineering). For more details, see the Chapter 1.2 and all the following chapters.

1.2   Principles of optical engineering of quantum materials
Principles of ultrafast optics: laser sciences and techniques

Though the sunlight can also modulate material properties, as evidenced by the developments in solar cells, we still need lasers to optical engineer condensed matter systems, because lasers are monochromatic, coherent, and easy to manipulate. Most coupling between light and matter requires strong light fields, and therefore, we use pulsed lasers to perform these tasks.

Compared to continuous wave (cw) lasers, the output of a pulsed laser can be

describe by the a sinusoidal wave modulated in the time domain,

$$E(t) = A(t) \sin{(\omega t + \phi)}, \tag{1.1}$$

where ω is the "center frequency" of the laser, $A(t)$ is the envelope of the pulse, and ϕ is called the carrier envelope phase.

In most outputs of pulsed lasers, the envelope $A(t)$ is a train of pulses, as illustrated in Figure 1.1. Each pulse has a Gaussian or a hyper-secant-squared shape, and the time duration of each pulse is labeled as Δt. The number of pulses per second is called the repetition rate (rep rate). The electric field at the peak of the pulses and the corresponding power are called the peak field and the peak power.
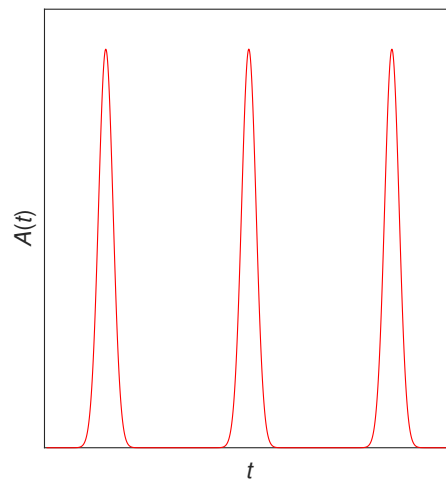
Figure 1.1: The envelope of a pulsed laser.

For cw lasers the energy is uniformly distributed in time. However, in pulsed lasers the energy is concentrated in pulses, enabling a much larger peak power than the average power. For a typical 5 W laser with a rep rate of 1 kHz and a pulse duration of 35 fs, a peak field on the order of 10^{11} V/m can be reached if the beam is focused down to 100 μm. This field is more than enough to induce dielectric breakdown in the air.

Apart from the large peak power, another advantage endowed by ultrafast femtosecond lasers is the high temporal resolution. A lot of energy scales in condensed matter systems are on the order of 1 to 100 meV, and a potential way to elucidate these energy scales is by measuring the system dynamics governed by these energy

scales. Therefore, we need a femtosecond laser in order to take stroboscopic snapshots of the system to discern the system states at different time delays after some events, such as the arrival of a previous strong optical pulse. This is the principle of pump probe type experiments, where a strong "pump" pulse induces modulations inside the materials, and some responses are probed as a function of the time delay between the pump and probe pulses.

The short duration of the optical pulses means that they cannot be monochromatic, since lasers with a single frequency can only be continuous wave lasers (the Fourier transform of $E(t)$ has a finite bandwidth centered around ω due to the envelope A). Therefore, an ultrafast laser must be generated by a gain medium[2] that can support multiple cavity modes. Assume the frequency separation between two adjacent cavity modes is $\Delta\nu$ and N modes participate in the pulse generation process, the shortest possible time duration is given by

$$\Delta t = \frac{0.441}{N\Delta\nu} \tag{1.2}$$

for Gaussian-shaped pulses. The titanium-doped sapphire (Ti:sapphire) lasers have a bandwidth of about 128 THz, corresponding to a range of 300 nm around the central 800 nm, supporting millions of modes for a meter-sized cavity.

In order to generate robust pulses periodically in time, the phase differences between all frequency modes propagating inside the cavity must be fixed and stable. This is accomplished by a process called mode locking. There are two major approaches of mode locking, active and passive, and most ultrafast femtosecond lasers operate with passive mode locking, unless a synchronization is required between the laser pulses and the electrical signal performing the active mode-locking process.

For passive mode locking, a saturable absorber, which is a material whose absorption decreases as the light intensity increases, is placed inside cavity. Thinking in the time domain, each time the peak of the pulse passes through the saturable absorber, the absorption is low, while when other parts of the pulse pass through the saturable absorber, the absorption is higher. Therefore, the pulse gets sharper and sharper in time, since the saturable absorber increases the relative intensity of the stronger part of the pulse to the weaker part of the pulse. Thinking in the frequency domain, since the absorption coefficient of the saturable absorber is modulated with a time period

---

[2]A laser emits light through a process of optical amplification based on the stimulated emission of electromagnetic radiation. The gain medium obtains energy from the laser pumping process, either electrically or optically, in order to stay in a population inversion state, so the gain medium can amplify the light. When the gain exceeds the loss from the cavity, a laser functions.

of the cavity round trip time $\tau = 1/\Delta\nu$, this process links the mode with frequency ν_0 and the side frequencies $\nu_0 + k\Delta\nu$ or $\nu_0 - k\Delta\nu$, enabling the mode-locking process.

Optical properties of quantum materials

As mentioned above, the optical engineering effects can be detected through pump probe type experiments. Although photoemission spectroscopy (Sie, Rohwer, et al., 2019) and electron diffraction (Vigliotti et al., 2004) can serve as the probes, the most versatile probes to use are optical probes—another laser pulse after the strong pump pulse. Therefore, we need to understand how the optical properties reflect the modulations to the electronic and magnetic properties of materials.

We start from the optical conductivity $\sigma(\omega)$, which relates the oscillating electric current and the electric field with $j(\omega) = \sigma(\omega)E(\omega)$. In a semiclassical model, we can calculate the real part of the optical conductivity as (Armitage, 2018)

$$\sigma_1(\omega) = \frac{\pi e^2}{m^2\omega}\frac{2}{(2\pi)^3}|\langle s'|p|s\rangle|^2 D_{s's}(\hbar\omega), \tag{1.3}$$

where $\langle s'|p|s\rangle$ is the dipole matrix element and $D_{s's}(\hbar\omega)$ is the joint density of states. From Equation 1.3 we can see that the real part of the optical conductivity reflects the density of states at the corresponding energies from the Fermi level. A typical conductivity spectrum is illustrated in Figure 1.2. The green part represents a Drude response, which is intraband excitation near the Fermi level from free electrons, normally seen in metals. The red part represents the interband excitation. The blue part represents the phonons and other low-frequency excitations.
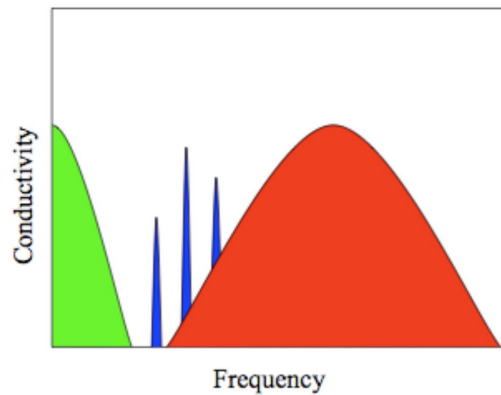

Figure 1.2: A typical optical conductivity versus frequency. From Armitage, 2018.

From the real part of the optical conductivity σ_1, many other optical constants of the material can be derived. The imaginary part of the optical conductivity σ_2 is

related to σ_1 by the Kramers-Kronig relation,

$$\sigma_2(\omega) = -\frac{2\omega}{\pi} \int_0^\infty d\omega' \frac{\sigma_1(\omega')}{\omega'^2 - \omega^2}. \tag{1.4}$$

The complex dielectric constant ϵ can be written in terms of the real part of the dielectric constant ϵ_1 and the real part of the optical conductivity σ_1 by

$$\epsilon = \epsilon_1 + \frac{4\pi i \sigma_1}{\omega}. \tag{1.5}$$

The refractive index n is the square root of the dielectric constant $n = \sqrt{\epsilon} = n_r + ik$, where n_r and k are the real and imaginary parts of the refractive index, respectively. The absorption coefficient α is related to the imaginary part of the refractive index k by $\alpha = 4\pi k/\lambda$, where λ is the wavelength of light in the vacuum. The reflectivity R can be inferred from n_r using the Fresnel equations,

$$r_s = \frac{n_1 \cos\theta_i - n_2 \cos\theta_t}{n_1 \cos\theta_i + n_2 \cos\theta_t}, \tag{1.6}$$

$$r_p = \frac{n_2 \cos\theta_i - n_1 \cos\theta_t}{n_2 \cos\theta_i + n_1 \cos\theta_t}, \tag{1.7}$$

where the light is entering medium 2 from medium 1, and r represents the complex amplitude reflection coefficient. s-polarization means that the electric field polarization is perpendicular to the scattering plane and p-polarization means that the electric field polarization is parallel to the scattering plane.

Equation 1.3 shows that modulations to the band structure of a material can be manifested in the optical properties. How does magnetism affect the optical properties of materials?

When magnetic orders break the symmetries of the system, they can be picked up by the second harmonic generation anisotropy, which is governed by nonlinear optical susceptibilities different from the linear optical constants as described above (the whole of Chapter II is dedicated to this subject). However, a more common probe of magnetic orders leverages the polarization of light. Here one needs to consider the dielectric constant ϵ not as a scalar but as a second-rank tensor ϵ_{ij}, where the indices i and j run through the spatial coordinates x, y, and z. Magnetism can induce changes to the off-diagonal elements of the tensor ϵ_{ij}, enabling the Faraday effect and the magneto-optical Kerr effect (MOKE).

The Faraday effect represents a rotation of the light polarization when a linearly polarized light passes through a magnetic material. The reason is that left- and

right-circularly polarized light travelling at different speed in magnetic media, and linearly polarized light is nothing but a linear superposition of left- and right-circularly polarized light. The Faraday polarization rotation can be calculated as (Němec et al., 2018)

$$\alpha_F = \frac{\omega d}{2c\sqrt{\text{Re}(\epsilon)}}\text{Im}(\epsilon_{ij}), \tag{1.8}$$

where ω is the light frequency, d is the sample thickness and ϵ_{ij} is the additional dielectric constant induced by magnetism. The Faraday effect requires that the light propagation direction is along the magnetization direction. The same holds true for MOKE.

The MOKE describes a rotation of the light polarization when a linearly polarized light is reflected from the surface of a magnetic material. Since a lot of materials which we studied are not transparent at our optical probe frequency, we mainly used the MOKE to detect both ferromagnetism and antiferromagnetism. Ferromagnetism is straightforward, since the material carries a macroscopic magnetization. There are three geometries for how we conduct the MOKE experiments, depending on the relative orientation between the magnetization, the sample surface and the scattering plane, as illustrated by Figure 1.3. When the magnetization is perpendicular to the sample surface normal, one can use a normally incident light and probe the polarization change. This is called polar MOKE. When the magnetization is along the sample surface normal, it will be perpendicular to the propagation of a normally incident light, so one will have to use obliquely incident light. Within this category, when the magnetization is parallel to the scattering plane, it makes the reflected light elliptically polarized and this geometry is called longitudinal MOKE. Or otherwise, when the magnetization is perpendicular to the scattering plane, it modifies the reflectivity of the sample surface, and this geometry is called transversal MOKE.
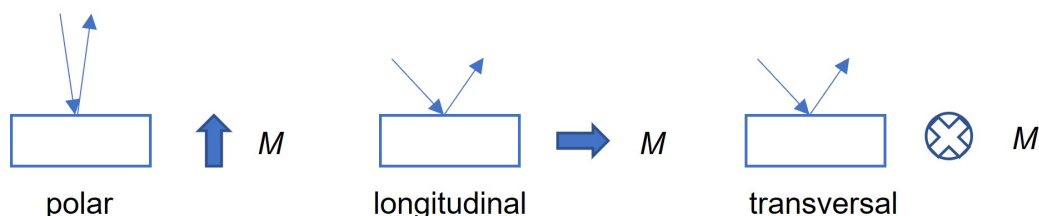

Figure 1.3: Three different geometries of MOKE measurements.

For antiferromagnetic materials, the lack of average magnetization does not hinder their investigation via MOKE. One reason is that the spins in a lot of antiferromag-

netic materials are canted, through either the antisymmetric Dzyaloshinskii–Moriya interaction or the coupling to other spin sublattices, forming a net magnetic moment anyway. The other reason is that if some external stimuli launch some coherent dynamics in the antiferromagnetic spins, a dynamical magnetization can also be induced (Němec et al., 2018), which is proportional to $\mathbf{L} \times d\mathbf{L}/dt$, where $\mathbf{L}$ is the order parameter of antiferromagnetism: the staggered magnetization, defined as the average magnetic moment in one sublattice within antiferromagnetism minus the average magnetic moment in the other sublattice within antiferromagnetism.

Both the Faraday effect and the MOKE effect scales linearly with the magnetic order parameters, namely, reversing the spins switches the sign of the effect. However, in some cases, the magnetic orders can, for example, induce some lattice changes through magneto-elastic coupling, which do not necessarily care about the orientation of the magnetization. In these cases some effects can depend quadratically on the order parameters. For example, in the Voigt effect (sometimes called the Cotton–Mouton effect), the polarization rotation angle is

$$\alpha_v = P^{\text{MLD}} \sin(2(\varphi - \beta)), \tag{1.9}$$

where φ is the light propagation angle, β is the magnetization angle, and the magnetic linear dichroism parameter P^{MLD} is quadratic in the magnetization projected onto the plane normal to the light propagation direction. This required relative orientation between the light propagation and the magnetization is quite opposite to what the Faraday effect requires.

For completeness I will conclude this part with a discussion of topological materials, with an emphasis on the effect of band structure geometries on the photogalvanic effect (PGE), where a dc current can be induced by light illumination through a rectification process. If a system preserves the time-reversal symmetry but breaks the spatial inversion symmetry, the Berry curvature $\mathbf{\Omega}$ should be an odd function of the momentum $\mathbf{k}$ (Orenstein et al., 2021). Consider that we apply an electric field along the x direction, the Fermi surface will be displaced along the x direction, and the net flux through the Fermi surface caused by the Berry curvature $\mathbf{\Omega}$ would be proportional to the electric field E. This net flux will cause an anomalous current which is a product of the instantaneous acceleration of the electron wave packets and the Berry curvature flux. This anomalous current requires a circularly polarized light, because i) the acceleration is proportional to the time derivative of the field, which is zero for a dc field, and ii) if the light is linearly polarized, the acceleration

and the Berry curvature flux will always be out of phase since the former is out of phase with the field and the latter is in phase with the field. Therefore, this effect is called the circular PGE (CPGE), and the magnitude scales quadratically with the light field E.

Optical engineering of quantum materials: A brief history

The previous section focuses on the probe part of a pump probe type experiment. This section will focus on the pump part, talking about different existing ways that light can modulate material properties. This section will establish a context where our research works took place.

When sunlight is strong, the earth is warm. People have known the heating effect of light for thousands of years. Similarly, if the various subsystems (lattice, electrons, and spins) thermalize quickly, the effect of light illumination can be summarized as an elevated temperature. This can be exploited to induce temperature-driven phase transitions. Heating up the lattice induces structural phase transitions, while heating up spins above their Curie or Néel temperature induces demagnetization (Beaurepaire et al., 1996), holding prospects for fast data storage.

Talking about optical engineering of magnetism, although in most cases the electric field component of light can impart energy into the spin subsystem more efficiently via spin-orbit coupling, the magnetic field component of light can also naturally couple to the spins inside the material through magnetic dipole Zeeman interaction, an energy term of $-\mu \cdot \mathbf{B}$, where μ is the magnetic moment. It has been shown that the low-frequency terahertz light can induce resonant magnons through this Zeeman mechanism (Kampfrath et al., 2011).

The magnetic field component of light always carries some finite frequency. If one wants to mimic a static magnetic field using light, they have to rely on the inverse Faraday effect, where a static magnetization can be induced by the electric field component of a circularly polarized light through (Kimel et al., 2005)

$$M(0) = \frac{\chi}{16\pi}[E(\omega) \times E^*(\omega)]. \tag{1.10}$$

This idea of using a finite-frequency electric field in light to mimic a static field in order to couple to some static orders inside materials has been extended beyond magnetism, such as inducing electronic gyrotropic (chiral) orders in 1T-TiSe$_2$ through shining circularly polarized light onto the sample (Xu et al., 2020). By using light to create a static scalar field that couples to the gyrotropic order, and cool the sample

down across the gyrotropic phase transition, the authors managed to train a large chiral domain.

In the previous cases of magnetism control, the spins themselves stay at the original locations and their orientations change because the light adds an additional term to the free energy of the spins. However, different nonthermal approaches exist. For one example, by exciting electrons across the charge gap using light, holons and doublons can emerge, where zero or two electrons occupy each lattice site which should be occupied by exactly one electron in equilibrium (Afanasiev et al., 2019). In this way, the spins themselves are disrupted spatially and it is no surprise the magnetic order will also be suppressed. As another example, light can modify the exchange interaction between spins (Ron, Chaudhary, et al., 2020), which is the already existing term in the spin free energy.

Low-frequency (mid-infrared) light can excite phonons, which are lattice vibrations. Since most condensed matter physics happens in the background of the lattice, excited phonons can couple to and modify various orders, including magnetism (Disa et al., 2020), ferroelectricity (Nova et al., 2019), and superconductivity (Mitrano et al., 2016). The authors used group theory-based symmetry analysis to determine which phonon couples to which order nonlinearly.

Established orders can also be reversed using light. If an order can choose from two possible states with equal energy, the free energy of the order parameter exhibits a double-well shape. When the light is intense enough, the electrons gain enough energy to escape their local minimum, as they roll into the other local minimum (Stanciu et al., 2007; Rubio-Marcos et al., 2018; Ning et al., 2020).

The recent developments of "Floquet engineering" (Y. H. Wang et al., 2013; Oka and Kitamura, 2019; Rudner and Lindner, 2020; McIver et al., 2020) have enabled an optical engineering mechanism where the effects come purely from the coherent interaction between electrons and the electric field in light. Floquet engineering can potentially shape the electronic, magnetic, and optical properties of quantum materials on demand. It will be the main focus of Chapter IV and Chapter 5.1. I will omit the detailed introductions here.

C h a p t e r   2

TIME-RESOLVED SECOND HARMONIC GENERATION (TR-SHG)

2.1 Principles of SHG

Introduction to nonlinear optics

Shine a red beam onto a glass and you get a red transmission. Double the red beam intensity and the red transmission intensity doubles. This is the essence of linear optics. Shine a red beam onto a β-BaB$_2$O$_4$ (BBO) crystal and you get an additional blue transmission. Double the red beam intensity and the blue transmission intensity quadruples. This is the essence of nonlinear optics.

Apart from being an interesting physical phenomenon, optical nonlinearity is useful in condensed matter research, as will be shown throughout later parts of the thesis. We performed the main works in this thesis using a second harmonic generation (SHG) probe, a process where light is generated at double the frequency of the incident light. Therefore, it is necessary that we provide an introduction of SHG and the optical nonlinearity in general.

Linear optics can be described by the equation $P(t) = \chi E(t)$, where the electric field induces a proportional electric polarization, linked by χ, the 3×3 susceptibility tensor[1]. If the field E oscillates with frequency ω, the induced polarization P will also oscillate with frequency ω, which will emit scattered light with frequency ω. In reality, there are more terms contributing to $P(t)$ (Boyd, 2020),

$$P(t) = \chi^{(1)}E(t) + \chi^{(2)}E(t)E(t) + \chi^{(3)}E(t)E(t)E(t) + ... \qquad (2.1)$$

In this case, if E carrying a frequency ω oscillates with a phase factor $\mathrm{e}^{-\mathrm{i}\omega t}$, then P will carry additional $\mathrm{e}^{-2\mathrm{i}\omega t}$, $\mathrm{e}^{-3\mathrm{i}\omega t}$, ..., factors in addition to the fundamental frequency $\mathrm{e}^{-\mathrm{i}\omega t}$, which means that harmonics of the fundamental frequency are generated.

---

[1]Note that this equation is true only for lossless media. If there is absorption of light, the electric polarization at a certain time instant does not only depend on the electric field at that time instant, but also on the electric field at earlier time instants. However, even for media with loss, this equation can still be written in the frequency domain and the main conclusions about optical nonlinearity will not be affected.

The magnitude of the higher-order susceptibility $\chi^{(n)}$ decreases approximately by a factor of $1/E_{\text{at}}$ when n increases by 1, where E_{at} is the characteristic atomic electric field strength on the order of 10^{11} V/m. Therefore, at weak light intensities, the higher-order frequency generation is much weaker than the lower-order frequency generation, let alone the fundamental light, because the n-th order harmonic generation intensity scales to the n-th power of the incident light intensity. As a result, intense light is required to observe harmonic generations of light, so femtosecond lasers are suitable for this kind of experiment, thanks to their high peak power. However, note that at high light intensities, higher-order harmonic generation intensity does not have to be weaker than lower-order harmonic generation intensity, especially for the comparisons between even- and odd-order harmonic generations (see the part below).

While the linear susceptibility $\chi^{(1)}$ is a 3×3 tensor, the second harmonic generation (SHG) susceptibility $\chi^{(2)}$ is a 3×3×3 tensor, and the third harmonic generation (THG) susceptibility $\chi^{(3)}$ is a 3×3×3×3 tensor. This ever-increasing number of elements in the tensors is extremely useful in determining the symmetries of condensed matter systems, be it structural, electronic, orbital or magnetic.

The essence of harmonic generation can be understood classically. Assume the electrons live inside a harmonic potential, and the electric field at frequency ω serves as the external force on the electrons. Then the problem is a simple forced harmonic vibration, and the well-known steady-state solution is just the electrons vibrating at ω. There is no second- or third-harmonic generation. However, if we add higher than quadratic terms into the electron potential, the Fourier transform to the oscillating solution of the electrons will contain higher-order frequency components. Depending on whether the electrons live in a noncentrosymmetric or centrosymmetric environment, the lowest-order correction to the harmonic x^2 potential is the x^3 or the x^4 term, enabling a lowest-order harmonic generation at the second harmonic or the third harmonic (meaning that SHG is forbidden in centrosymmetric media within this classical model).

SHG as a way to study system symmetries: Various origins

We can use a simpler argument to show that SHG is mostly forbidden in centrosymmetric media. The SHG process (actually, only the leading-order electric dipole term, as we will soon see) can be described by the equation

$$P_i(2\omega) = \chi_{ijk}^{(2),\text{ED}} E_j(\omega) E_k(\omega), \tag{2.2}$$

where the summation over j and k is implicated on the right-hand side. I will discuss the the exact meaning of ED later. Now let us apply a spatial inversion operation to the Equation 2.2. Here P becomes $-P$ and E becomes $-E$ since they are polar vectors. If the system possesses spatial inversion symmetry, $\chi^{(2),\text{ED}}$ is not changed at all. Therefore, Equation 2.2 becomes $-P_i(2\omega) = \chi_{ijk}^{(2),\text{ED}}E_j(\omega)E_k(\omega)$, telling us that $\chi^{(2),\text{ED}}$ must vanish. Historically, this property makes SHG a very sensitive probe for surfaces or interfaces, since they necessarily break the inversion symmetry. SHG is also a sensitive probe for phase transitions that breaks the inversion symmetry, such as ferroelectricity (which will be part of the focus of Chapter III).

With this inversion symmetry sensitivity said, it was well known to researchers in the early days of SHG that SHG can also occur in centrosymmetric materials (Bloembergen, Chang, et al., 1968), though often orders of magnitude weaker than the SHG from noncentrosymmetric materials. What is the origin of the SHG observed? Now we clarify some terms used to distinguish SHG origins. The process described by Equation 2.2 is called the electric-dipole (ED) process, which is the leading order of SHG. If the bulk of the material breaks the inversion symmetry, then the bulk ED is allowed, and everything is good.

If the bulk ED is forbidden by the inversion symmetry, we need to distinguish between several other SHG processes. The first one is the surface ED, which is the same ED term, but from the necessarily inversion symmetry-breaking surface of the materials. The surface ED is much smaller than the bulk ED term, because the surface effect is only evident in several top layers, while the bulk ED contribution can come from all the way down to the penetration depth of the fundamental or SHG light, whichever is smaller. Another often overlooked ED SHG source is the randomly oriented polar domains, which break the local inversion symmetry and thus allow a finite ED SHG (Dolino, 1972).

Or more often, we need to consider higher-order SHG process in the absence of bulk ED. The first one is the magnetic dipole (MD) contribution, and the second one is the electric quadrupole (EQ) contribution. Both contributions are $1/c$ weaker than the ED contribution, where c is the speed of light. Basically this is a game of how you can combine two quantities oscillating at ω to form another quantity oscillating at 2ω. Within the MD category, there are two ways. The first one is combining $E(\omega)$ and $H(\omega)$ within light to form $P(2\omega)$, where H is the magnetic field, and

$P(2\omega)$ oscillates to emit SHG. We call this the type-1 MD SHG,

$$P_i(2\omega) = \chi_{ijk}^{(2),\text{MD1}} E_j(\omega) H_k(\omega). \tag{2.3}$$

The second one is still combining two $E(\omega)$, but forming an oscillating magnetization $M(2\omega)$ to emit SHG. We call this the type-2 MD SHG,

$$M_i(2\omega) = \chi_{ijk}^{(2),\text{MD2}} E_j(\omega) E_k(\omega). \tag{2.4}$$

Both processes are allowed in centrosymmetric media because H and M are axial vectors.

The EQ contribution is a combination of two $E(\omega)$ to form an oscillating electric quadrupole $Q(2\omega)$ to emit SHG. A lot of literature converts this to an equivalent form, which is combining $E(\omega)$ and its gradient $\nabla E(\omega)$ to form $P(2\omega)$, described by the equation $P_i(2\omega) = \chi_{ijkl}^{(2),\text{EQ}'} E_j(\omega) \nabla_k E_l(\omega)$. However, we need to take precautions with this conversion because it is actually a sum of EQ and type-1 MD (Pershan, 1963). We show this by breaking up this equation to symmetric and antisymmetric parts regarding the last two indices,

$$\begin{aligned} P_i(2\omega) &= \frac{1}{2} [\chi_{ijkl}^{(2),\text{EQ}'} E_j(\omega) \nabla_k E_l(\omega) + \chi_{ijkl}^{(2),\text{EQ}'} E_j(\omega) \nabla_l E_k(\omega)] \\ &+ \frac{1}{2} [\chi_{ijkl}^{(2),\text{EQ}'} E_j(\omega) \nabla_k E_l(\omega) - \chi_{ijkl}^{(2),\text{EQ}'} E_j(\omega) \nabla_l E_k(\omega)]. \end{aligned} \tag{2.5}$$

For the antisymmetric part (the second line of equation 2.5), $\nabla_k E_l(\omega) - \nabla_l E_k(\omega)$ is actually just H. Therefore, the symmetric part (the first line of Equation 2.5) corresponds to the EQ SHG, described by

$$P_i(2\omega) = \chi_{ijkl}^{(2),\text{EQ}} E_j(\omega) \nabla_k E_l(\omega), \tag{2.6}$$

where the last two indices of the fourth-rank tensor $\chi^{(2),\text{EQ}}$ are interchangeable (for more details on the intrinsic symmetry of the $\chi^{(2)}$ tensors, see Chapter 2.2).

With surface ED, type-1 MD, type-2 MD and EQ all allowed in the absence of bulk ED SHG, how do we know what exactly the source is if we observe some SHG in a centrosymmetric material? The first way is tracking how the SHG intensity evolves with the angle of incidence of the fundamental light, while keeping other factors fixed. This can be done by using an s-polarized light, where the polarization is perpendicular to the scattering plane, so the electric field direction stays fixed when the angle of incidence is changed, and detecting the s-polarized component of SHG (I will discuss more details in Chapter 2.2). ED SHG contribution is not affected

by the angle of incidence, as evidence by the Equation 2.2, so the SHG should be constant for all angles of incidence. However, MD and EQ contributions depend strongly on the angle of incidence. For the type-1 MD, the direction of H depends on the angle of incidence. For type-2 MD, how the oscillating M generates the detected SHG depends on the angle of incidence. For EQ, the ∇ part actually renders the dependence on the angle of incidence (more details in Chapter 2.2). Another way to distinguish these different SHG sources is by performing SHG rotational anisotropy, where different processes have different functional forms. This will be the main topic of Chapter 2.2. In that chapter we will also talk about how the different processes above contribute to the final SHG intensity that we observe.

Apart from discerning the inversion symmetry, SHG can also resolve different point groups better than linear optics. The root of this advantage is the increased number of susceptibility tensor elements. I will provide an example to illustrate this point. Consider the point groups 3 and 4 for example[2]. For linear susceptibility tensor, the symmetry-allowed tensor forms of these two point groups is the same

$$
\begin{pmatrix}
\chi_{xx} & 0 & 0 \\
0 & \chi_{xx} & 0 \\
0 & 0 & \chi_{zz}
\end{pmatrix},
\tag{2.7}
$$

so linear optics cannot distinguish these two point groups. On the other hand, their SHG susceptibility tensor $\chi^{(2),\mathrm{ED}}$ is very different. The tensor for the point group 3 is

$$
\begin{pmatrix}
\begin{pmatrix} \chi_{xxx} \\ \chi_{xxy} \\ \chi_{xxz} \end{pmatrix} & \begin{pmatrix} \chi_{xxy} \\ -\chi_{xxx} \\ \chi_{xyz} \end{pmatrix} & \begin{pmatrix} \chi_{xxz} \\ \chi_{xyz} \\ 0 \end{pmatrix} \\
\begin{pmatrix} \chi_{xxy} \\ -\chi_{xxx} \\ -\chi_{xyz} \end{pmatrix} & \begin{pmatrix} -\chi_{xxx} \\ -\chi_{xxy} \\ \chi_{xxz} \end{pmatrix} & \begin{pmatrix} -\chi_{xyz} \\ \chi_{xxz} \\ 0 \end{pmatrix} \\
\begin{pmatrix} \chi_{zxx} \\ 0 \\ 0 \end{pmatrix} & \begin{pmatrix} 0 \\ \chi_{zxx} \\ 0 \end{pmatrix} & \begin{pmatrix} 0 \\ 0 \\ \chi_{zzz} \end{pmatrix}
\end{pmatrix},
\tag{2.8}
$$

---

[2]Throughout this thesis I will use the Hermann–Mauguin notation, sometimes called the international notation, for point groups. The correspondance between different notations can be found on the webpage https://en.wikipedia.org/wiki/Crystallographic_point_group.

which has six independent coefficients, while the tensor for the point group 4 is

$$\begin{pmatrix} \begin{pmatrix} 0 \\ 0 \\ \chi_{xxz} \end{pmatrix} & \begin{pmatrix} 0 \\ 0 \\ \chi_{xyz} \end{pmatrix} & \begin{pmatrix} \chi_{xxz} \\ \chi_{xyz} \\ 0 \end{pmatrix} \\ \begin{pmatrix} 0 \\ 0 \\ -\chi_{xyz} \end{pmatrix} & \begin{pmatrix} 0 \\ 0 \\ \chi_{xxz} \end{pmatrix} & \begin{pmatrix} -\chi_{xyz} \\ \chi_{xxz} \\ 0 \end{pmatrix} \\ \begin{pmatrix} \chi_{zxx} \\ 0 \\ 0 \end{pmatrix} & \begin{pmatrix} 0 \\ \chi_{zxx} \\ 0 \end{pmatrix} & \begin{pmatrix} 0 \\ 0 \\ \chi_{zzz} \end{pmatrix} \end{pmatrix}, \tag{2.9}$$

which is different from Equation 2.8 and has four independent coefficients. Therefore, SHG is able to distinguish between the point groups 3 and 4.

Above, we talked about how we use SHG to say something about the point group of the materials, especially the inversion symmetry of the system, and what other SHG processes exist in centrosymmetric media. Now at the end of this section I would like to talk about time-reversal symmetry a little bit—not really how SHG helps to determine the time-reversal symmetry of the systems, but how the time-reversal symmetry dictates the form of the SHG susceptibility tensors.

Under time-reversal, nonmagnetic systems often do not change[3], so the SHG tensors should not change. We call these time-reversal even tensors the i-type tensors. In magnetic systems, the time-reversal operation reverses all the spins inside the system, and how the SHG susceptibility tensors change depends on how the tensors couple to the magnetic order. If the tensors couple directly (linearly) to the magnetic order, then the tensors should also change sign. If the tensors couple indirectly to the magnetic order (for example, quadratically because the tensors couple to the lattice deformation induced by the magnetic order), then the tensors should stay the same. We call the time-reversal odd tensors the c-type tensors. The i or c types will impose additional restrictions to the tensor forms. An important thing to note here is that whether the tensor is i- or c-type does not depend on the SHG category (ED, MD, or EQ), namely, one has to determine how a specific SHG process seen in a specific material couples to the magnetic order, in order to determine the type of the SHG tensor, and cannot make a priori guesses on the types of the susceptibility tensor.

---

[3]This is not actually true if the SHG probe fundamental frequency or its second harmonic is resonant with some electronic transitions, since the excitation of electrons can have complicated ramifications on the treatment of the time-reversal operation.

Quantum mechanical descriptions of SHG

The classical model of harmonic generation mentioned above is intuitive, but does not help much if we want to perform calculations of $\chi^{(2)}$ in real materials, especially if the fundamental frequency ω or 2ω is close to some electronic transitions. We will resort to a quantum mechanical description of SHG here. SHG is a three-photon process, where the density of photons is so high that the material can simultaneously absorb two photons and emit one photon which combines the energy of the prior two photons, as illustrated in Figure 2.1. The system starts from an initial state, absorbs $\hbar\omega$ to an intermediate state, and then absorbs $\hbar\omega$ to the final state. The intermediate state and the final state can be virtual states. However, if there are states close to the energy $\hbar\omega$ or $2\hbar\omega$, the SHG will be enhanced.
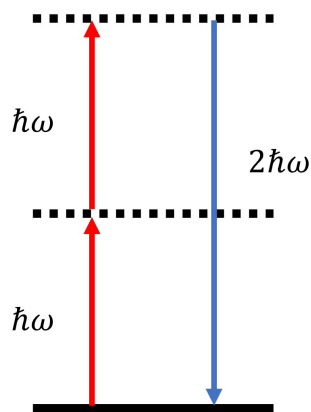
Figure 2.1: The three-photon process.

If we want to treat this problem quantum mechanically, we need to write down the Hamiltonian caused by the SHG probe light,

$$H = \frac{1}{2m}[p - qA(r, t)]^2 + q\varphi(r, t), \tag{2.10}$$

where A is the vector potential and φ is the electrostatic potential. Using the Coulomb gauge, $\nabla \times A(r, t) = 0$, we can drop the second term since $\varphi(r, t) = 0$. Therefore, the interaction Hamiltonian is

$$\begin{aligned} V &= -\frac{q}{m}A \cdot p \\ &= -\frac{q}{m}A(0) \cdot p e^{i(k \cdot r - \omega t)}. \end{aligned} \tag{2.11}$$

In the electric dipole approximation, we assume the light wavelength is much larger than the dimension of the electronic wavefunction, and set $e^{ik \cdot r} = 1$. If we retain

the Taylor expansion of this exponential to higher orders, we get MD, EQ SHG and so on. So with the Coulomb gauge and the electric dipole approximation $V = -(q/m)A(0) \cdot p e^{-i\omega t}$.

Often in condensed matter physics we use another gauge, called the length gauge. The length gauge and the Coulomb gauge are related by the Goeppert-Mayer transformation, $A'(x) = A(x) + \nabla \Lambda$, where $\Lambda(x) = -x \cdot A(0)$. In the length gauge, the interaction Hamiltonian can be written as

$$V = -eE(0,t) \cdot x. \tag{2.12}$$

Plugging this interaction Hamiltonian to a second-order time-dependent perturbation theory, we can calculate the SHG susceptibility in the ED channel

$$\chi_{ijk}^{\text{ED}} \propto \sum_{m,f} \frac{\langle g|r_i|f\rangle\langle f|r_j|m\rangle\langle m|r_k|g\rangle}{(E_f - E_g - 2\hbar\omega)(E_m - E_g - \hbar\omega)}$$
$$+ \frac{\langle g|r_j|f\rangle\langle f|r_k|m\rangle\langle m|r_i|g\rangle}{(E_m - E_g + 2\hbar\omega)(E_f - E_g + \hbar\omega)} \tag{2.13}$$
$$+ \frac{\langle g|r_k|f\rangle\langle f|r_i|m\rangle\langle m|r_j|g\rangle}{(E_f - E_g - \hbar\omega)(E_m - E_g + \hbar\omega)}$$
$$+ (j \leftrightarrow k).$$

Here g denotes the ground electronic state to start with, m and f are intermediate states and final states to be summed over. If one already knows the wavefunctions of the extended states derived from the band structure or localized states derived from a single-ion model inside a material, they can select the states which are closest to resonance with any of the three lines[4] in Equation 2.13 and calculate χ.

2.2 SHG rotational anisotropy

The high-speed measurement setup: from 10 K to 400 K

SHG is good for distinguishing between different point groups of the materials, thanks to the large number of independent tensor elements. However, a single SHG intensity cannot tell us which elements are zero and which are not. One needs to measure at least a functional form in order to fit according to some hypothetical point group, to determine whether the point group is correct or not. This is achieved through SHG rotational anisotropy (RA).

The principle of SHG RA measurements is as follows: a fundamental beam is focused onto the sample surface and the reflected SHG intensity in the specular

---

[4]These three lines correspond to three SHG pathways, and often only the first line remains if the system starts from the ground state.

direction is measured. The single crystal sample rotates along its sample surface normal, then the SHG is measured as a function of this sample rotation angle. We can control the incident light to be *s*- or *p*-polarized, and we can choose to collect the SHG reflection in the *s*- or *p*-polarization. Therefore, we get four combinations - SS, SP, PS, and PP, where the first (second) letter indicates the incident (reflected) light polarization. However, this approach has two problems (Torchinsky et al., 2014). The first is that for low-temperature measurements the samples are placed inside a cryostat, and due to the space limitations it is not easy to rotate a sample inside the cryostat. The second problem is that, if the beam is not focused exactly at the center of the sample rotational axis, when the sample is rotated the beam will walk on the sample surface, thus greatly limiting the measurement capacity. Therefore, we adopted an alternative but equivalent approach, where we do not rotate the sample but rotate the scattering plane consisting of the incident light and the SHG reflection. This is basically saying instead of rotating the sample in the lab, we rotate the lab around the sample.

When rotating the scattering plane, there are two strategies. One is measuring SHG angle by angle—staying at one angle, measuring SHG for a period of time, then rotating to the next angle until the whole 2π rotation is finished. For this approach, we can use a photomultiplier tube (PMT) combined with a lock-in amplifier to measure the SHG intensity at each scattering plane angle. However, this approach cannot filter out the low-frequency noises for the laser intensity, namely, if the SHG intensity differs between two scattering plane angles, it is hard to say whether it truly comes from the SHG anisotropy or it comes from the laser intensity fluctuation. Therefore, we adopted another approach for better signal-to-noise ratio. We rotate the scattering plane with a high frequency (~2 Hz) while almost simultaneously measuring the SHG reflection from all angles, and integrate for a period of time in order to average between rotations (Harter et al., 2015). Since SHG responses from different angles cannot be separated temporally with this approach, it requires separating them spatially. Since PMT has no spatial resolution, we used a charge-coupled device (CCD) camera as the SHG detector.

As illustrated in Figure 2.2, we used a grating-based oblique-incidence setup to measure the SHG rotational anisotropy, because by using oblique incidence with a combination of all the four polarization combinations (SS, SP, PS, and SP) we can obtain more complete information about the SHG susceptibility tensor $\chi^{(2)}$, and by using a grating we can make sure that the focused beam does not move

on the sample when we rotate the scattering plane. A diffraction grating diffracts the incoming beam to various orders m according to the equation $d \sin \theta_m = m\lambda$, where d is the distance between adjacent slits of the grating. In normal gratings the majority of the diffracted power goes to the 0-th order, which is not needed in our experiment. We only need the +1 order in order to perform the oblique incidence, though with normal incidence on the grating the -1 order will also be inevitably generated. Therefore, we chose to use a phase mask to diffract the incoming beam.
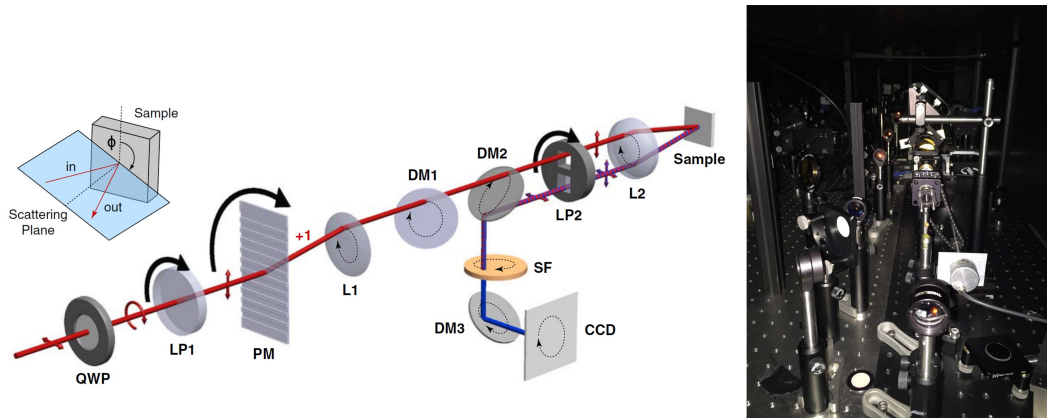

Figure 2.2: The SHG-RA setup. The left is a cartoon taken from Harter et al., 2015. The right is the actual setup.

A phase mask is just like a diffraction grating—periodic slits etched into fused silica, and the slit distance determines the diffraction angle. However, in phase masks the etching depth is accurately controlled, and by selecting the correct etching depth (see Figure 2.3), interference effects make the 0-th order diffraction vanish. Each wavelength corresponds to an optimal etching depth[5]. Therefore, the main diffraction power goes to the +1/-1 orders, while some remains in the higher orders. For 800 nm normal incidence, the optimal etching depth is 0.882 μm. For 1200 nm normal incidence, the optimal etching depth is 1.339 μm. For 1030 nm normal incidence, the optimal etching depth is 1.144 μm. We use $d \sin \theta_m = m\lambda$ to calculate the diffraction angle. For fundamental wavelength of 800 nm, we used a phase mask with $d = 14.4$ μm, resulting in a diffraction angle of 3.2°. For fundamental wavelength of 1200 nm, we used a phase mask with $d = 21.4$ μm, resulting in a similar diffraction angle. The material of our phase mask is AR-coated fused silica, and the lateral dimensions are shown in Figure 2.3. The total thickness of the phase

---

[5]For a calculator of the optimal etching depth, see https://www.holoor.co.il/optical-calculator/gratings-optical-calculator/.

mask is 0.5 mm, which can be varied. A possible vendor is Photomask PORTAL[6]. We face the etchings towards the sample. The duty cycle of the etching is 50%.
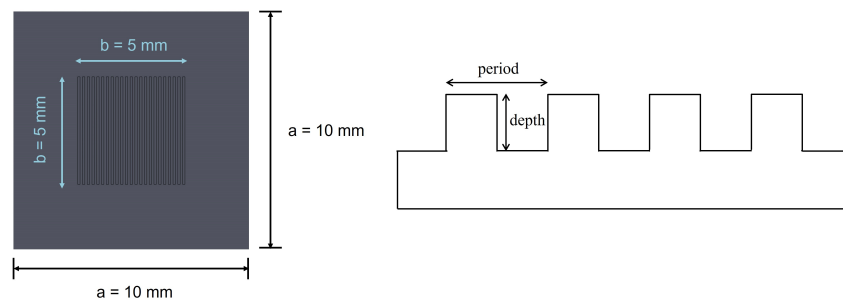

Figure 2.3: The phase mask. The left is a top view showing the lateral dimensions of the phase mask, with etched and un-etched sections. The right is a side view of the etched section of the phase mask, showing the period and the etching depth. Courtesy of Wencan Jin.

Now I would like to describe all the optics involved in the SHG-RA setup from upstream to the sample, then to the CCD detector. The whole setup is horizontal and on an optical table lower than people's eyes, in order prevent stray laser light from entering the eyes. Before light enters the setup, it goes through some power and polarization control optics. For the power control, we can either use two polarizers (Thorlabs LPVIS050), a half waveplate (Thorlabs WPH05M-808) and a polarizer, or a continuous variable neutral density filter (Thorlabs NDC-25C-2-B) and a polarizer. Because in the SHG-RA setup, the incident light onto the sample is linearly polarized, and the light power must be kept constant while the scattering plane is rotated, we must shine a circularly-polarized light into the setup and use a rotating polarizer to choose s or p polarization. Therefore, we put a quarter waveplate (Thorlabs AQWP05M-980, QWP in Figure 2.2) after the power control module, and make the fast axis of the quarter waveplate at 45° with the polarization axis of the polarizer in the power control module to create circularly-polarized light. The circular polarization can be checked by measuring the output power as one rotates another polarizer after the quarter waveplate; it should be constant, or in practice within 5% variance.

Then we use a telescope (Thorlabs LA1433-B with $f = 150$ mm, and AC508-075-B with $f = 75$ mm as L1 in Figure 2.2) to shrink the beam size going into the setup by a factor of half. After the first lens of the telescope we put a rotating polarizer (Thorlabs LPVIS050, LP1 in Figure 2.2) to control the incident polarization. We

---

[6]https://www.photomaskportal.com.

put the phase mask (PM in Figure 2.2) close to, but not exactly at the focal point of the first lens, in order to reduce damage to the phase mask. In practice, we put the phase mask after the focal point of the first lens. The +1 and -1 order diffraction beams diverge after the phase mask, and the second lens of the telescope (L1) also serves to collimate these two orders. In real experiments, the -1 order is blocked by a black tape and only the +1 order passes through.

Then we use an achromatic doublet lens (Thorlabs AC254-030-AB-ML, L2 in Figure 2.2) with a focal length of 30 mm as the objective, to get both a tight focus and a significant angle of incidence of $\sim 8°$. Note that both the fundamental and SHG wavelengths pass through this doublet lens. That is why we used an achromatic lens, and one needs to pay attention to which side of the lens faces the incoming beam.

The sample is placed at the focus of the objective, and its surface normal should be aligned to coincide with the optical axis of the whole setup in order to get a constant angle of incidence when the scattering plane is rotated. In practice, both of these two constraints can be met if the +1 order reflection beam coincides with the -1 order incoming beam, and the -1 order reflection beam coincides with the +1 order incoming beam.

The reflected beam passes through an output polarizer (Thorlabs GT5-A, LP2 in Figure 2.2) to select the SHG polarization between between *s* and *p*. In some literature this output polarizer is also called an analyzer. Because the reflected beam is not along the optical axis of the setup, we mounted the output polarizer on a cage plate (Thorlabs SP01). We machined a hole on one side of the plate to hold the output polarizer, and another hole on the other side of the plate to allow the incident beam through.

Finally we arrive at the signal collection and measurement module. Instead of normal mirrors, We use dichroic mirrors (transmitting longer wavelengths and reflecting shorter wavelengths) with a cut-off wavelength of 635 nm (Semrock Di03-R635-t1-25-D which is of custom size) to steer the SHG beam into the CCD detector, in order to pre-filter out the fundamental wavelengths. We use a periscope geometry. We use one dichroic mirror to reflect the beam up to the vertical direction, and a second dichroic mirror to pick up the beam and reflect it into the CCD (DM2 and DM3 in Figure 2.2). Note that the fundamental beam also transmits through DM2 before reaching the sample. When the scattering plane rotates, the incident fundamental beam polarization oscillates between *s* and *p* for DM2, causing an oscillation in the intensity transmission, we put a third dichroic mirror (DM1 in Figure 2.2) to

compensate for this unwanted effect (Harter et al., 2015).

Before the CCD we put several spectral filters to further filter out the strong fundamental reflection. For our 800-nm SHG experiments, we used two 650-nm shortpass filters (Edmund optics 84-712) and two 400-nm bandpass filters (Thorlabs FB400-40 and FBH400-40).

Since the SHG intensity is very weak, we used an electron multiplying CCD camera (Andor iXon Ultra 987) to enhance the detection efficiency. The 512×512 pixels enable the SHG signal at different scattering plane angles to be projected onto different spots on the CCD image. Cooling the CCD camera down to -85 °C helps reducing the thermal noises, but cosmic rays can still enter the CCD as super bright spots on the acquired CCD image. Therefore, we always acquire more than one CCD image with the same experimental conditions and use despeckle algorithms to obtain the correct SHG rotational anisotropy. We show some typical CCD images in Figure 3.3. Since the beam has a finite size, we choose an inner ring and an outer ring which encompass the measured signal, and integrate everything between these two rings to get the SHG intensity at a certain scattering plane angle. A box made of black acrylic sheets encompasses the whole setup with holes to let beams through, in order to reduce the noise.

To rotate the scattering plane, the input polarizer LP1, the phase mask PM, and the output polarizer LP2 need to rotate with exactly the same speed. This infrastructure is done by coupling all spinning parts to the same rod (McMaster-Carr 8934K26) through tubes, needle-roller bearings (McMaster-Carr 5905K135), sprockets (McMaster-Carr 2737T2 and 2737T13), and roller chains (McMaster-Carr 6261K171). The rod is then connected to a stepper motor (Lin Engineering 5618S-01S-RO) through shaft couplings (McMaster-Carr 6412K11), which is then controlled by a motor controller [Galil DMC-30016-BOX(SER)]. We use customized programs to control the rotation of the scattering plane, and set the rotation frequency to be 2 Hz.

We mount our samples onto customized copper sample mounts using Torr Seal epoxy for better thermal conductivity. If one performs SHG-RA experiments at room temperature and ambient pressure, we can simply tape the sample mount onto a standard mirror mount for easier alignment. If one wants to perform these experiments at lower/higher temperatures, we use optical cryostats (Janis ST-500) in combination with IR fused silica windows for different temperatures and optical access, where the window transmission is nearly constant ($\sim 90\%$) in the near

infrared range.

For measurements at different temperatures we screw our sample holder onto the cryostat cold plate with indium foil between them for better thermal conduction. The whole chamber is pumped down to 10^{-7} torr by a vacuum pumping station (Pfeiffer HiCube 80 Eco) combining a backing pump and a turbopump. We have achieved temperatures from 80 K to 400 K using liquid nitrogen as the cryogenic liquid and down to 10 K using liquid helium. For low-temperature experiments we glue a cover slip onto the extruded sample mount edge with vacuum grease, lying on top of the sample surface with a gap. This trick prevents low-temperature condensation forming on the sample surface during measurements. Since our SHG-RA setup is horizontal, we use the cryostat vertically, and use transfer lines to transfer cryogenic liquids into the cryostat. Normally the pressure inside the liquid dewar is more than 3 psi higher than the atmosphere pressure for stable liquid flow. We connect a tube from the exhaust arm of the cryostat to prevent ice from forming at the output port of the cryogenic exhaust. We put the cryostat on an XYZ translation stage (Thorlabs PT3) for easier movements.

Determining the susceptibility tensor

In this section I will talk about how to determine the SHG susceptibility tensor $\chi^{(2)}$ from the measured SHG rotational anisotropy with SS, SP, PS, and PP polarization channels.

As shown in Chapter 2.1, either P or M is generated at frequency 2ω. The conversion from P or M to our measured SHG reflection is a complex problem requiring solving the Maxwell's equations under boundary conditions (Bloembergen and Pershan, 1962), but a simple conclusion is that, both the magnitude and the direction of the electric field in the SHG reflection $E(2\omega)$ is proportional to $P(2\omega)$, and likewise for the relationship between H and M. E and H are related by $E \propto k \times H$.

The procedure starts from determining the SHG process (ED, EQ, or MD; i- or c-type) and the material's point group. With this information the form of the $\chi^{(2)}$ tensor can be determined. We used the Bilbao crystallographic server to help us with this task[7]. This involves several steps:

i) Determining the rank of the tensor. ED and MD tensors are of third-rank, and EQ tensors are of fourth-rank.

---

[7]https://www.cryst.ehu.es/.

ii) Determining the intrinsic symmetries of the tensor. For ED, all the three indices correspond to polar vectors, and the last two indices should be interchangeable because they are equivalent, meaning that $\chi_{ijk}^{(2),\text{ED}} = \chi_{ikj}^{(2),\text{ED}}$. Therefore, the intrinsic symmetry of the tensor is V[V2] (using the Jahn symbols[8]). For type-1 MD, the first two indices correspond to polar vectors and the last one corresponds to an axial vector. The intrinsic symmetry is V2eV. For type-2 MD, the first index corresponds to an axial vector. The last two indices correspond to polar vectors and are interchangeable. The intrinsic symmetry is eV[V2]. For EQ, all the four indices correspond to polar vectors. Normally in the equation $P_i(2\omega) = \chi_{ijkl}^{(2),\text{EQ}} E_j(\omega) \nabla_k E_l(\omega)$ we substitute ∇ with ik because the electric field carries a phase factor $e^{ik\cdot r}$. However, this needs to be done with caution since the ∇ gradient takes place inside the nonlinear optical material and k is not continuous across the material surface (Yang et al., 2009). Therefore, in the rare instances where the incident beam contains both s and p polarization *and* the gradient is taken along the sample surface normal *and* the material is anisotropic, we cannot replace ∇ with ik. Fortunately, in the common cases we are allowed to replace ∇ with ik and therefore the second and fourth indices of the tensor $\chi^{(2),\text{EQ}}$ are interchangeable. In Chapter 2.1 we already said that for the EQ contribution the last two indices should be interchangeable, so the last three indices should all be interchangeable. The intrinsic symmetry is V[V3]. For magnetic point groups, if the tensor is c-type, a time reversal constant a should be added in front of the Jahn symbols for relevant SHG processes (see Appendix A for an example).

iii) Using the selected (magnetic) point group and the Jahn symbols corresponding to the intrinsic symmetries, we can use the Bilbao crystallographic server to get the corresponding SHG susceptibility tensors. One should be careful about the convention of the definition of x, y, and z directions used in the server, especially for trigonal and hexagonal point groups.

Having obtained the tensors, we need to rotate them from the structural coordinates to the lab coordinates, where the sample sample surface is the xy plane and the surface normal is z. Say the sample surface normal is the direction [hkl] so the normal unit vector is $\mathbf{u} = \mathbf{r}/|\mathbf{r}|$, where $\mathbf{r} = h\mathbf{a} + k\mathbf{b} + l\mathbf{c}$. To rotate the tensor, we first need to find the rotation matrix that rotates vector $z = (0, 0, 1)$ to u, which is

$$R = I + [v]_\times + [v]_\times^2 \frac{1-c}{s^2}, \tag{2.14}$$

---

[8]https://www.cryst.ehu.es/html/cryst/mtensor_help.html.

where $v = z \times u$, $s = |v|$, $c = z \cdot u$, and $[v]_\times$ is the skew-symmetric cross product matrix of v defined as

$$\begin{pmatrix} 0 & -v_3 & v_2 \\ v_3 & 0 & -v_1 \\ -v_2 & v_1 & 0 \end{pmatrix}. \tag{2.15}$$

Using a third-rank tensor as example, then we can calculate the tensor in the lab coordinates as

$$\chi_{ijk}^{\text{lab}} = R_{ii'} R_{jj'} R_{kk'} \chi_{i'j'k'}^{\text{crys}}. \tag{2.16}$$

Then we calculate the tensor when the scattering plane (or equivalently, the sample) rotates by an angle φ. The rotation matrix R^φ can be expressed as

$$\begin{pmatrix} \cos\varphi & -\sin\varphi & 0 \\ -\sin\varphi & \cos\varphi & 0 \\ 0 & 0 & 1 \end{pmatrix}, \tag{2.17}$$

so the tensor can be transformed as

$$\chi_{ijk}^{\varphi} = R_{ii'}^\varphi R_{jj'}^\varphi R_{kk'}^\varphi \chi_{i'j'k'}^{\text{lab}}. \tag{2.18}$$

We will use this tensor to calculate the SHG intensity at a scattering plane angle φ.

We set the scattering plane to be the xz plane, and use an angle of incidence θ. The wave vector $k \propto (\sin\theta, 0, \cos\theta)$. For s polarization incidence, the electric field $E \propto (0, 1, 0)$. For p polarization incidence, the electric field $E \propto (-\cos\theta, 0, \sin\theta)$. The magnetic field $H \propto k \times E$.

Then we can calculate $P(2\omega)$, using the tensor and the fields. For s polarization reflection, the measured SHG intensity $I(2\omega) \propto (P_y)^2$. For p polarization reflection, the measured SHG intensity $I(2\omega) \propto (P_x \cos\theta + P_z \sin\theta)^2$, because we need to project the SHG field amplitudes to the direction perpendicular to the reflection wave vector.

We have obtained the functional form of $I(2\omega)$ in all the four SS, SP, PS, and PP geometries. If we have also measured the SHG rotational anisotropy data, we can then fit these four channels simultaneously. In the actual data we need to know which angle corresponds to $\varphi = 0$ in the functional form. This can be done either through some symmetry analysis or by marking some specific crystallographic axis on the sample holder, so we can compare this direction with the obtained SHG anisotropy in the setup geometries. For the simultaneous fit, we are sometimes allowed to add an (close to one) overall factor to each polarization channel to

account for the difference in reflectivity between $s-$ and $p-$ polarized light. If the fitting is reasonably good, we can extract the relative strength between different tensor elements and/or their temperature evolution. To get their absolute values, we need to compare the measured intensity to that of some standard sample, such as GaAs. If the fitting fails, one needs to either consider other SHG sources, or conclude that the point group which is used for the fit has higher symmetry than the actual point group of the sample.

2.3 Time-resolved measurement techniques

Generating pump pulses: Regenerative amplifier, OPA, DFG, and BBO

We have thoroughly introduced the SHG probe technique. Now I will turn to the pump side–the laser pulses that actually modulate the material properties. In the Hsieh lab we use a Ti:sapphire femtosecond ultrafast laser (Coherent Astrella), which has a fundamental output of 800 nm pulses. The rep rate is 1 kHz, the pulse width is 35 fs, and the maximal power is 5 W. We use a beam splitter to split 3.5 W into an optical parametric amplifier (Light Conversion TOPAS), which can generate a spectrum from 1160 nm to 2600 nm. The maximal efficiency occurs at 1400 nm, where the power of the signal plus idler can reach 1 W. The OPA beams can either go through a differential frequency generation (DFG) module to generate wavelengths as long as 15 μm with a power $\sim$ 10 mW, or bypass DFG to directly reach the setups.

I would like to use this section to briefly discuss the components of a femtosecond laser, as well as OPAs and DFGs. I will use the systems in the Hsieh lab as examples.

The main part of Astrella is a regenerative amplifier, where weak pulses can be amplified inside the gain medium Ti:sapphire, and the amplified pulses are the main output of the laser. Two important beams need to enter the regenerative amplifier, including the seed laser which contains the weak pulses to be amplified, and a pump laser to supply energy to the amplifier (inducing the population inversion). I will talk about the general principles of a regenerative amplifier later, and now I want to first focus on the seed laser and the pump laser.

The seed laser in the Astrella system is called Vitara. Vitara itself is an 800-nm Ti:sapphire laser (one that is not amplified is often called an oscillator) made by the mode-locking mechanism described in Chapter 1.2, with a bandwidth of 70 nm. Vitara also needs its own pump laser to gain energy. That pump module is called Coherent Verdi G-Series, which is a continuous-wave optically-pumped semiconductor laser emitting green (532 nm) light. Verdi G itself is pumped by

an 808-nm laser diode. The emission wavelength of Verdi G is engineered by the composition and the thickness of the gain medium, and the emitted radiation is converted to green by frequency doubling with nonlinear crystals. The rep rate of the oscillator Vitara is 80 MHz.

The pump laser for the amplifier in the Astrella system is called Revolution. Revolution is a diode-pumped, intra-cavity doubled, Q-switched Nd:YLF laser of 527 nm. Q-switch is another way to make ultrafast lasers other than mode locking. While mode locking is used for generating femtosecond pulses, Q-switch is mainly used for nanosecond pulses, where the Q (which stands for quality) factor of the lasing cavity which controls the loss of light circulating the cavity can be switched. Though some lasers use electro-optical Q-switch, most Q-switched lasers (including Revolution) use acousto-optical Q switch, where a radio-frequency (RF) signal is converted to ultrasonic vibrations in the acousto-optical modulator, which then changes the loss of the circulating light. When the loss is high, lasing is suppressed. When the loss is low, a burst of laser power is emitted. The 527-nm beam comes from frequency doubling through an LBO crystal.

With the seed laser and the pump laser ready, we are now ready to talk about the principles of the regenerative amplifier. We should note that the peak power of the pulses is very high, and thus prone to unwanted nonlinear effects in the gain medium. Therefore, the lasers use a method called chirped pulse amplification (CPA), which earned a Nobel Prize in Physics in 2018. In this method, the pulses are stretched in time, so their peak power can be greatly reduced. Then the stretch pulses get amplified. Finally they are compressed again in time to form short but stronger pulses.

There are two ways to stretch a pulse in time. As Equation 1.2 shows, the shortest pulse width is inversely proportional to the bandwidth of the pulse. A pulse whose time duration is equal to this shortest value is called bandwidth limited, meaning that its time duration cannot be further compressed unless it gains a broader bandwidth through nonlinear processes. Therefore, one way to stretch the pulses is cutting some bandwidth of the pulses, so the remaining bandwidth still forms a bandwidth-limited pulse, though with longer time duration. However, in this way the pulses cannot be compressed back after the amplification process because part of the bandwidth is already lost, so it is not an ideal way to stretch pulses in this application.

So we turn to chirping the pulses. A chirped pulse is not bandwidth limited. A very common way to produce chirped pulses is to pass a bandwidth-limited pulse through
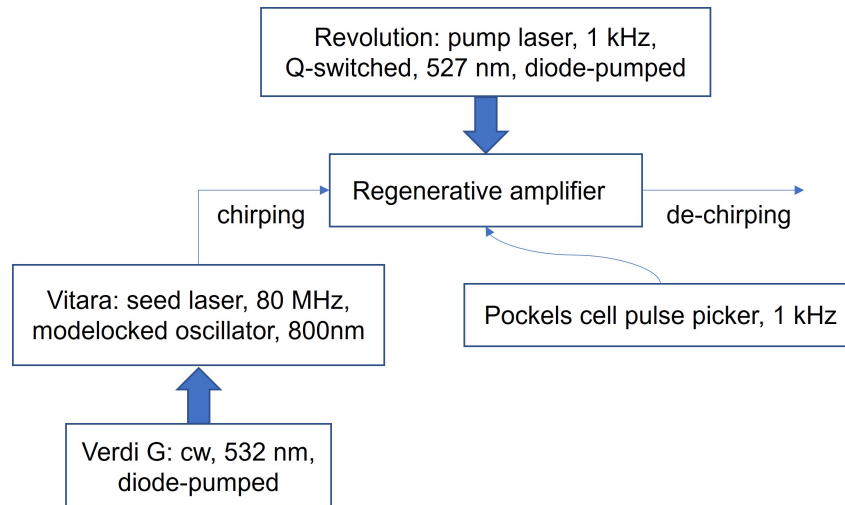
Figure 2.4: The layout of Astrella. The thick blue arrows mean pumping energy.

any dispersive media. Red light travels faster than blue light inside the media, so red light leads the pulse and blue light trails behind. As a result, the pulses get stretched in time. A more efficient and controlled way to induce chirping is by using prism pairs or diffraction grating pairs. A prism or grating can separate different wavelengths spatially, so different wavelengths travel different distances (in air or vacuum) at the same speed c, resulting in chirping effects similar to the ones seen in dispersive media. Normally the beam needs to go through four prisms or gratings to merge spatially again.

After the pulses are stretched, they are sent into the regenerative amplifier. For the regenerative amplifier, the gain medium first accumulates energy by optical pumping. Then, an electro-optical or acousto-optical switch opens so a pulse can enter the cavity and undergo several round trips inside the cavity to be amplified, and then the pulse gets emitted out of the cavity. An electrically controlled Pockels cell, which manipulates the beam polarization, and a polarizer are used as a pulse picker, to down convert the rep rate from the 80 MHz oscillator to 1 kHz. A sketch of the whole Astrella system is shown in Figure 2.4.

The 800-nm pulses from the Astrella amplifier then enter the OPA to generate longer wavelengths. One can view this process as breaking the 800-nm photon (1.55 eV) into two parts, whose photon energy sums up 1.55 eV (the fundamental pump photon energy). The part that has a higher energy (wavelength shorter than twice the pump wavelength) is called the signal beam and the part that has a lower energy (wavelength longer than twice the pump wavelength) is called the idler beam.

However, the real optical path is more complicated.

The 800-nm pump beam is split into three ways: 80% as beam 1, 16% as beam 2, and 4% as beam 3. Beam 3 is focused onto a nonlinear crystal (NC1) to generate a white light continuum (WLC), which contains the signal wavelengths. The WLC is then dispersed in time. Both the WLC and beam 2 are focused onto another nonlinear crystal (NC2). Beam 2 serves as the pump beam to amplify some wavelengths of the WLC. The time delay between beam 2 and the WLC is controlled, and which wavelengths of the WLC coincide with beam 2 in time on the NC2 determines which wavelength of the WLC gets amplified. This wavelength will be the signal wavelength of the OPA output. The amplification happening in the NC2 is the pre-amplification process. After the pre-amplification, only the pre-amplified signal continues to propagate, and all other beams (including the beam 2 as a pump and the idler wavelengths generated, as well the sum frequency generation between these wavelengths) are blocked. The pre-amplified signal typical outputs 1-3 μJ of energy. The following main amplification process can boost this to tens ~ hundreds of microjoules.

The path length of main pump beam (beam 1) is controlled so that beam 1 and the pre-amplified signal arrive at a third nonlinear crystal (NC3) at the same time. On the NC3, both beam 1 and the pre-amplified signal are collimated and follow exactly the same beam path. In this way, the signal can be amplified again. Proper pump intensity is required for saturated amplification. If the pump intensity is too low, the conversion efficiency of OPA is low. If the pump intensity is too high, both the spatial and spectral profile of the OPA output will be bad. In this way, the idler is also generated in collimation with the signal, and the signal polarization is perpendicular to the idler polarization.

After the signal and idler beams are generated through the OPA, they can enter the non-collinear differential frequency generation (NDFG, here non-collinear means that the signal and idler beams are not collinear on the DFG crystal) to generate longer wavelengths. If one pumps the OPA with photon energy E_{pu} and requires a DFG photon energy E_{DFG}, the required signal and idler photon energies can be calculated as

$$E_{\text{sig}} + E_{\text{idl}} = E_{\text{pu}}, \qquad (2.19)$$

$$E_{\text{sig}} - E_{\text{idl}} = E_{\text{DFG}}. \qquad (2.20)$$

In the actual beam path, the collimated signal and idler beams coming out of the OPA get separated by a dichroic mirror, and they shine onto a DFG nonlinear crystal

at the ssame time. When changing the DFG wavelength, both the angle difference between signal and idler beams and the angle of the DFG crystal need to be changed.

With the signal or idler wavelengths, we can double their frequencies using BBO crystals to get the visible spectrum. For the use of BBO crystals, phase matching conditions need to be considered.

The essence of phase matching can be viewed in a BBO crystal with a thickness d in the z direction. The fundamental frequency beam propagates along the z direction, seeing a refractive index $n(\omega)$, and SHG is generated at each z position inside the BBO crystal. After the SHG is generated at a specific z position, the SHG continues to propagate along the z direction with a refractive index $n(2\omega)$. The SHG generated at different z locations all propagates to the back side of the BBO crystal, and one needs them to constructively interfere to efficiently generate an overall SHG output, namely, their phases need to match at the back side of the BBO crystal. The phase of each SHG component carries both the phase of the fundamental beam at the location where SHG is generated, and the phase accumulated through the SHG propagation. Therefore, to achieve phase matching $n(\omega)$ must be equal to $n(2\omega)$. In reality, the phase-matching conditions are met using different cuts of the BBO crystals for different nonlinear processes. A 29.2° cut is for SHG of 800 nm and a 44.3° cut is for THG of 800 nm. Given a specific cut of BBO and a specific fundamental wavelength, one can also change the angle of incidence and the azimuthal angle to optimize the SHG efficiency from the BBO crystal.

Transient reflectivity and time resolved (tr) MOKE setups

We have introduced the generation of the pump pulses. Now I will introduce the pump probe setups. For the pump side, we can use different wavlengths, different angles of incidence, different polarizations, and different intensities. For the probe side, we can choose from different probe methods. We can use reflectivity as a probe of the charge dynamics. We can use MOKE to probe the dynamics of magnetism, as detailed in Chapter 1.2. We can use SHG to probe the dynamics of symmetry-breaking orders, such as antiferromagnetism.

For the pump beam path, we can use a half wave plate (Thorlabs AQWP05M-1600 for OPA signal wavelengths) and a polarizer (Thorlabs LPNIR050) to control its intensity. We place the half wave plate in a motorized precision rotation stage bundled with a DC servo motor (Thorlabs KPRM1E) for automated fluence control. We use another half wave plate after the polarizer to change the linear polarization

of the pump beam, or a quarter wave plate (Thorlabs AQWP05M-1600) after the polarizer to create a circularly or elliptically polarized pump beam.
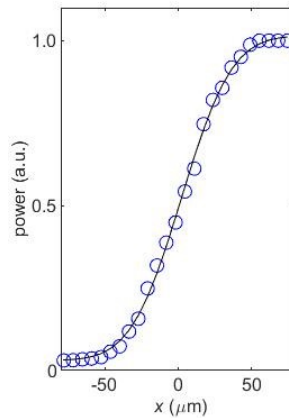

Figure 2.5: Typical measurement from the knife-edge method.

We can measure the beam size of the focused pump beam on the sample using a knife edge method. We mount a knife edge on a two translation stages (Thorlabs PT1), one for moving the knife edge to the sample location along the z axis (the optical axis of the objective before the sample), and another one for moving the knife edge laterally in order to cut part of the beam. We put a power meter after the knife edge and measure the transmitted power as a function of the lateral position of the knife edge. A typical measurement is shown is Figure 2.5. Assume a Gaussian beam profile of the intensity $I = I_0 \exp\left(-2r^2/w^2\right)$, we can fit the measured data to an error function,

$$P = P_0 + \frac{P_{\max}}{2}\left(1 - \mathrm{erf}\left(\frac{\sqrt{2}(x - x_0)}{w}\right)\right). \tag{2.21}$$

From this fitting we can get the full-width-at-half-maximum (FWHM) diameter of the focused beam to be $w\sqrt{2\ln 2}$.

We can measure the both the temporal and the frequency profile of the pump beam using frequency-resolved optical gating (FROG). In FROG the beam is split into two arms, similar to a Michelson interferometer. One arm has a fixed optical path and the other arm has a retroreflector on a translation stage. The two reflections are then focused onto a BBO crystal, and their sum-frequency generation (SFG, which in this case has the same wavelength as the SHG of the beam since the two reflections have identical wavelengths) is measured by a spectrometer as a function of the optical path length of the adjustable arm. Using a phase-retrieval algorithm, we can obtain the temporal and the frequency profile of the beam.

In a pump probe experiment, both the beam size and the penetration depth of the pump beam should be much larger than those of the probe beam in principle. However, our experiments require a large pump fluence so the pump beam size cannot be too big. Our typical pump beam size is 150 μm and a typical probe beam size is 100 μm. The fluence of the pump beam should also be much larger than that of the probe beam in principle. This can easily be satisfied in transient reflectivity or tr-MOKE experiments because they are linear optical probes, and even with a weak probe we can still get a good signal-to-noise ratio. However, if we use an SHG probe, we normally use a probe fluence on the same order of magnitude as the pump fluence, since SHG is a nonlinear process and a fundamental probe that is too weak will result in an almost undetectable SHG intensity.

For transient reflectivity ($\Delta R/R$) measurement, the reflection of the probe beam is routed into a biased Si detector (Thorlabs DET10A2) using a D-shaped mirror (Thorlabs PFD10-03-P01 mounted on DMM1). The detector is then connected to a lock-in amplifier (Stanford Research Systems SR830) using BNC cables.

For pump probe experiments, the pump goes through a delay stage (ILS100LM-S) with a broadband hollow retroreflector (Newport UBBR2.5-1I), controlled by a motion controller (Newport ESP301) to control the delay between the pump and probe pulses. An optical chopper system (Thorlabs MC2000B) chops the pump pulses at half the laser rep rate (500 Hz) triggered by the laser output. Therefore, half of the probe pulses going into the photodetector are modulated by the pump pulse and the other half are not modulated by the pump pulse. By taking the difference between these two, we can get the pump-induced changes to the reflectivity ΔR. When measuring the R itself, we set the frequency of the lock-in amplifier to be equal to the laser rep rate, instead of half the laser rep rate as when measuring ΔR.

Lock-in amplifiers are used to measure small signals in a noise environment which is up to a million times larger than the signal itself. The power lies in the Fourier transform of periodic functions. For example, when measuring ΔR, the signal that we want to measure is $R_{\text{pumped}} - R_{\text{unpumped}}$. Because we use a chopper at 500 Hz, the signal that we want to measure is a signal modulated at 500 Hz. What the lock-in amplifier does is that it first mixes (multiplies) the signal and a sinusoidal reference waveform at 500 Hz, then applies a low-pass filter. This effectively singles out the 500-Hz Fourier transform of the measured signal. Lock-in amplifiers has two channels, labeled X and Y. The signal obtained from the description above is called X. In Y, everything is the same but the phase of the reference waveform is shifted

by 90°. Therefore, we can obtain both the amplitude and the phase of the measured signal relative to the reference waveform. A time constant determines the transfer function of the low-pass filter by

$$H(\omega) = \frac{1}{1 + i\omega\tau}, \tag{2.22}$$

where $\tau = RC$ in an RC low-pass filter. Using a larger τ yields a less-noisy measurement.

We can also define a phase-insensitive amplitude $R = \sqrt{X^2 + Y^2}$. However, in real experiments, we do not use the R channel (not to be confused with the reflectivity R). Rather, we auto-phase to concentrate all signals to the X channel, and measure the X channel only. The reason is that changes in reflectivity can be both negative and positive, but using the R channel hinders the determination of the sign. Still, we do not know whether a positive reading in the X channel means a positive or a negative ΔR (changes in reflectivity). To determine this, we can leak a little bit of the pump beam into the photodetector and keep the phase of the lock-in amplifier fixed. Then we can use the sign of the lock-in reading caused by the pump leakage to help us determine the sign of ΔR. At high light intensities the response function of the photodetector can become nonlinear. Therefore, we use ND filters in front of the photodetector to reduce the light intensity entering the photodiode. We have also placed a polarizer in front of the photodetector to continuously tune the light intensity entering the photodiode, therefore achieving a maximal ΔR.

In tr-MOKE setups, we need to measure a light polarization change on the order of mrad to μrad. A normal photodetector cannot reach a high enough signal-to-noise ratio. We need to use a balanced detector (Thorlabs PDB210A) to complete this task. Here we focus on the simplest cases where the magnetism induces a linear polarization rotation or an elliptical polarization.

To detect a small polarization change, we first use a Wollaston prism (Thorlabs WPQ10) to separate the beam into two orthogonally polarized outputs with a separation angle. Then the two outputs enter the two detectors of a balanced detector, which subtracts the two inputs from each other. Without the pump we first need to *balance* the balanced detector. For the magnetism-induced polarization rotation case, we put a half-wave plate in front of the Wollaston prism, so that the two outputs from the Wollanston prism have equal intensities. At this point the reading from the balanced detector is zero and it is said to be balanced. With this condition the detection sensitivity for the polarization rotation is the highest. Then we add the

pump beam and chop the pump at half the laser rep rate. If the pump modifies the magnetism, changes in the light polarization will make the balanced detector no longer balanced.

If the magnetism induces an elliptical polarization, the balancing method above will not work for detecting a change in the ellipticity, because a change in the ellipticity will not change the directions of the major and minor axes within an elliptically polarized light which have a 90° phase difference. Therefore, to balance the balanced detector, we first need to use a quarter-wave plate to transform the elliptically polarized light into a linear polarization. Then we use a half-wave plate as normal to balance the balanced detector. In this way changes in the light ellipticity will make the balanced detector no longer balanced.

The tr-SHG setup

Because the CCD detector that we used for SHG measurements cannot be connected to a lock-in amplifier, we have to bear with the readout noise of the CCD camera and the extrinsic noises when we perform tr-SHG experiments. We used several tricks to reduce the noise.

First of all, since for the most of the time we only measure tr-SHG at a fixed scattering plane angle (e.g., the largest lobe in the SHG-RA patterns), namely, the scattering plane is not rotating, so we do not care about the spatial resolution of the CCD camera. The SHG spot can occupy ~ 100 pixels on the CCD camera, and instead of averaging the readings from all the pixels occupied by the SHG spot, we perform binning on the pixels (normally 16×16) to make a large pixel then read out just the large pixel. In this way we can greatly reduce the readout noise from the CCD camera. We also repeat the same time-delay scan for multiple (~ 10) times in order to filter out the laser power fluctuation.

If we do need to take the tr-SHG RA patterns, we have to make sure that the mirror that steers the pump beam into the objective and thus the sample does not block the incident or reflected probe beams at any scattering plane angles. For oblique pump incidence this is easy since we can just place a D-shaped mirror (Thorlabs PFD10-03-P01 mounted on DMM1) out of the circle formed by the spinning incident probe beam for introducing the pump beam onto the sample. If we want to do normally incident pump beam, however, things get a little bit tricky because the separation between the +1 and -1 order probe beams before the objective is only ~ 1 cm and we need to fit a mirror into that space. We glued a small mirror (d = 5 mm) onto an

optical post using a thin pin as the steering mirror for the pump beam. In this way, the SHG-RA pattern is only blocked at the two vertical angles.

Although we put a lot of filters in front of the CCD camera to only allow the SHG wavelengths through, the pump scattering and the mixing between the pump and probe can pose a serious obstacle in our measurements. Some high-order generation of the pump beam can fall into the acceptance range of the filters, and in some cases they can overwhelm the CCD camera and make the SHG detection impossible. This problem is especially acute when an odd-order harmonic generation of the pump is close to the probe SHG wavelength, and the structure of the sample does not break inversion symmetry. For example, if we want to pump a material at 2000 nm and probe SHG at 800 nm to see changes in the MD SHG, the fifth-harmonic of the 2000 nm will be much stronger than the SHG of 800 nm. The pump scattering is an effect caused by the pump only so it persists at all time delays.

On the other hand, some high-order mixing between the pump and probe can also fall into the acceptance range of the filters, but this effect is only present close to $t = 0$. Both the pump scattering and the pump-probe mixing do not necessarily fall onto the same pixels as the SHG spot on the CCD camera, so some of the times we can filter them spatially. But if they do fall onto the same spot, there are two ways we can fix this. The first solution is that we use a very obliquely incident pump beam which does not even go through the same objective lens as the probe beam. We can minimize (but not necessarily remove) the pump scattering this way. Another solution is that we use a spectral band pass filter that has a narrower bandwidth, which might allow the SHG frequency through but reject other unwanted beams. However, note that a narrower bandwidth filter will also make the SHG beam intensity itself weaker.

Data analysis methods

There are two typical shapes of the time-resolved responses. The first shows a coherent Gaussian behavior and the second shows an asymmetric decaying behavior, as shown by the red and black curves in Figure 2.6. The coherent Gaussian shape normally represents the convolution between the pump and probe pulses, and often indicates that no excitations are generated by the pump, especially if the excitations need to take longer time to decay than the pulse width. For example, a coherent $\Delta R/R$ can often be seen when the system is pumped sub-gap because no real electronic transitions are made. On the contrary, resonant pumping normally
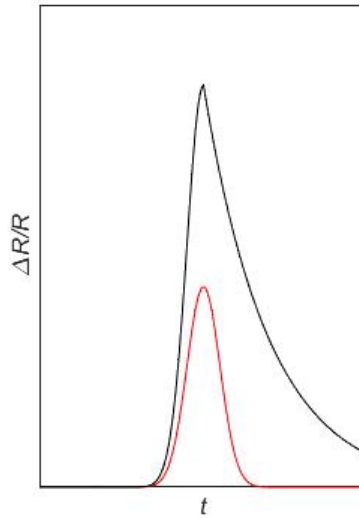
Figure 2.6: Two typical shapes of the time-resolved responses.

produces electronic excitations and an exponentially decaying $\Delta R/R$ curve, where the decaying time corresponds to the thermalization of the system. For a coherent Gaussian shape, the largest $\Delta R/R$ occurs at time zero, the time instant when the pump and probe pulses fully overlap. On the contrary, for a decaying behavior, the largest $\Delta R/R$ occurs after time zero. This is expected since the most electrons are excited after the whole pump pulse arrives at the sample, and time zero corresponds to the time when half of the pump pulse arrives at the sample. The full curve (the black curve in Figure 2.6) can be modeled by the convolution between a Gaussian-shaped probe pulse, a Gaussian-shaped pump pulse, and the response from the sample assuming a δ-function pump and probe. The response from the sample can be modelled as

$$f(t) = H(t)[a \exp(-t/\tau) + c],$$ (2.23)

where $H(t)$ is the Heaviside step function. The constant c accounts for the heating caused by the pump, which might take nanoseconds to dissipate away from the excited region, and we are going to discuss heating in more details in Chapter 4.1. Therefore, even in time-resolved curves with a decaying shape, we can use the rise dynamics around time zero to infer the time durations of the pump and probe pulses.

In Equation 2.23 we only have one exponential. Sometimes we fit our data to the sum of two exponentials, with separate time scales. This can be fully understood through a three-temperature model (Kirilyuk, Kimel, and Rasing, 2010).

If we concentrate our focus on the resonant pump, the pump pulse first excites electrons to higher energies. We assume that the electrons themselves reach a thermal equilibrium in no time, so all the absorbed energy from the pump goes to heat up the electrons. We further assume that the lattice (phonons) and the spins (magnons) are the other two thermal reservoirs which reach their respective thermal equilibrium in no time. Therefore, we can define temperatures for the three subsystems and the whole dynamics is determined by the transfer of energy from the electron subsystem to the lattice subsystem and the spin subsystem. If we assume that the pump pulse has ended and the energy transfer is local (namely, we do not consider the diffusion of heat), and use the T_e, T_s, and T_l to represent the temperatures of the electron, spin and lattice subsystems, we can write their dynamics as

$$c_e \frac{dT_e}{dT} = -g_{el}(T_e - T_l) - g_{es}(T_e - T_s), \tag{2.24}$$

$$c_l \frac{dT_l}{dT} = -g_{el}(T_l - T_e) - g_{ls}(T_l - T_s), \tag{2.25}$$

$$c_s \frac{dT_s}{dT} = -g_{es}(T_s - T_e) - g_{ls}(T_s - T_l), \tag{2.26}$$

where c represents the heat capacity of the subsystems and g represents the coupling between different subsystems. The solution of the equations has a double-exponential form. For example, the solution of T_s is

$$T_s(t) = T_{s0} + a_1(1 - e^{-\lambda_1 t}) + a_2(1 - e^{-\lambda_2 t}). \tag{2.27}$$

We note that this three-temperature model has many variations. For example, the three thermal reservoirs do not have to be electron, lattice, and spin, and can be others like electron, one set of phonons, and another set of phonons (Laurita et al., 2019). If there are only two thermal reservoirs exchanging energy, this model can be simplified to a two-temperature model, and the dynamics will be a single exponential.

In some transient responses we see an oscillating behavior on top of the decaying signal (Hoegen et al., 2018). This normally means that some coherent excitations (phonons, magnons, CDW modes) are launched by the pump pulse, and the frequency of the oscillation represents the frequency of the coherent excitations. This can be understood in two ways, either in the time domain or in the frequency domain. Let me illustrate it using coherent phonons. In the time domain, the phonons (lattice vibrations) modulate the material properties in a time periodic pattern with their own periods, and it comes as no suprise that the responses from the same

material exhibit the same periodic pattern. In the frequency domain, on the other hand, the probe light experiences Raman scattering (for $\Delta R/R$ measurements) or hyper-Raman scattering (for tr-SHG measurements). Assume the probe light has frequency ω and the phonon has frequency Ω. The Raman scattered light at $\omega - \Omega$ reaches the photodetector, and interferes with the fundamental probe light at ω, so a beat at frequency Ω is generated.

Chapter 3

SHG AS A MEANS TO STUDY SHORT-RANGE STRUCTURAL CORRELATIONS

3.1 SHG studies of nonpolar-polar transition in metallic LiOsO$_3$

Introduction to polar metals

In this section, I will use an example of LiOsO$_3$ to show that SHG is not only capable of detecting the inversion symmetry breaking through the ED channel, but also able to detect short-range correlations, which then couple to some symmetry-preserving lattice distortions through temperature dependence in the EQ SHG (Shan, de la Torre, et al., 2020). This is an often overlooked power of SHG.

Among all noncentrosymmetric materials, the ones that yield the largest SHG intensities are those where the lattice structures themselves break the inversion symmetry, instead of the electronic states or the spin configurations breaking the symmetry. People have used SHG to study noncentrosymmetric structures for decades. Among all 32 point groups, 11 of them are centrosymmetric (m$\bar{3}$, m$\bar{3}$m, 4/m, 4/mmm, mmm, 2/m, $\bar{1}$, $\bar{3}$, $\bar{3}$m, 6/m, 6/mmm). Among the other 21 noncentrosymmetric point groups, 10 of them are polar (4, 4mm, mm2, 2, m, 1, 3, 3m, 6, 6mm). A polar point group is defined as a point group in which there is more than one point that every symmetry operation leaves unmoved. A polar structure cannot have more than one polar axis.

Polar structures are closely related to ferroelectrics, where a macroscopic electric polarization forms in the absence of an electric field, much as a macroscopic magnetization formation in the absence of a magnetic field for ferromagnets. However, there are three main differences between ferroelectrics and ferromagnets:

i) In ferromagnets, the electron spins align in the same direction, but in ferroelectrics it is the structural polarization (formed by negatively- and positively-charged ions) that aligns, not the electrons.

ii) The spin order in ferromagnets is stabilized by short-range exchange interaction. Though there is also long-range magnetic dipole-dipole interaction between spins, it is much weaker than the exchange interaction and is more responsible for the formation of magnetic domains. However, in ferroelectrics (at least in people's

traditional understanding) the driving force of the nonpolar to polar phase transition is purely the long-range electric dipole-dipole interaction. As a result, it is counter-intuitive when people discovered polar metals, as in metals this long-range interaction should be screened by free electrons. To resolve this dilemma, people resorted to short-range interaction between electric dipoles which cannot be effectively screened. Until 2013 all discovered polar metals are already polar at room temperature, namely, they do not exhibit nonpolar-polar phase transitions at accessible temperatures. Therefore, the observation of a nonpolar-polar structural phase transition in $LiOsO_3$ (Shi et al., 2013) in 2013 only made this more puzzling. Note that here I use the term polar metals instead of ferroelectric metals, because in addition to the spontaneous polarization formation, ferroelectrics need to satisfy another criterion: the direction of the polarization should be able to be reversed with an external electric field. This cannot be done in metals since electric fields cannot penetrate into the bulk of metals, unless the metal that we are talking about is atomically thin (Fei et al., 2018).

iii) In ferromagnets there is only one temperature scale: the Curie temperature, where the thermal fluctuation is smaller than the energy scale set by the exchange interaction, so the spins can order. The existence of spins (local magnetic moments) is guaranteed by the electronic orbital occupation of ions. However, in ferroelectrics even the existence of local electric dipole (within one unit cell) cannot be taken for granted. At very high temperatures the center of positive charges in a single unit cell coincides with the center of negative charges—there is no local electric dipole. Only below a certain temperature T_I local electric dipoles start to form. There is another temperature scale T_{II} which corresponds to the dipole-dipole interaction strength. If $T_I > T_{II}$, there is a temperature window where local dipoles have formed but not ordered, and the ferroelectric phase transition is called order-disorder type. If $T_I < T_{II}$, the dipoles order as soon as they form, and the ferroelectric phase transition is called displacive type (Aubry, 1975).

It is in this context that we started to investigate the material $LiOsO_3$ using SHG. Some of the questions that we tried to answers are, whether its structural phase transition at 140 K is displacive or order-disorder type, and what the driving force of this phase transition is.

As we mentioned, ferroelectric phase transitions typically occur in insulating materials where long-range electrostatic forces between local electric dipoles are unscreened (Slater, 1950). The observation of a ferroelectric-like structural phase

transition in metallic $LiOsO_3$ in 2013 (Shi et al., 2013) was therefore counterin-
tuitive and challenged the conventional understanding of how polar distortions are
stabilized (Anderson and Blount, 1965; Puggioni and Rondinelli, 2014). Over the
last few years, there is growing evidence that the phase transition in $LiOsO_3$ is
primarily of a continuous order-disorder type (Shi et al., 2013; Sim and B. G. Kim,
2014; H. M. Liu et al., 2015; Jin, A. Zhang, et al., 2016; Padmanabhan et al., 2018;
Jin, L. Wang, et al., 2019), where local dipole moments generated by the off-center
displacement of Li ions form well above the Curie temperature ($T_c \sim 140$ K). Based
on first-principles calculations (Xiang, 2014; Benedek and Birol, 2016; Zhao et al.,
2018), these local moments interact through short-range forces arising from local
bonding preferences, which are un-screened by the itinerant carriers, to achieve
long-range order at T_c.

To understand the form of the short-range interacting Hamiltonian that describes
$LiOsO_3$, it is necessary to address its critical behavior upon cooling through T_c.
In insulating proper ferroelectrics such as the isostructural compound $LiNbO_3$, the
presence of long-range forces should suppress dipolar fluctuations and lead to a very
narrow or no critical region (Tokunaga, 1974; Tokunaga and Mitsui, 1976). In polar
metals, on the other hand, where inversion symmetry is lifted through geometric
routes, the screening of long-range forces can in principle lead to wide critical
regions that are more amenable to study. However, critical dipolar fluctuations
in $LiOsO_3$ cannot be probed using standard dielectric measurements owing to its
metallicity. They are also challenging to measure using X-ray or neutron scattering
due to the weak interaction with Li and the small size of available single crystals
respectively. The temperature dependence of the local dielectric susceptibility of
$LiOsO_3$ was recently inferred from the linewidth of a Raman active Li vibrational
mode (Jin, L. Wang, et al., 2019), but it was argued to closely follow a Curie-Weiss
law above T_c, with no evidence of a critical region.

Here we detect short-range dipolar correlations arising from Li cation displace-
ments above T_c in $LiOsO_3$ through electromechanical coupling, which is normally
seen in insulators. In polar metals, this effect can also be large due to microscopic
dipole-strain interactions. More specifically, the short-range interaction energy be-
tween local c-axis oriented moments D_i in $LiOsO_3$ (Figure 3.1a) can be described
by the thermal expectation value of an Ising-type Hamiltonian $\mathcal{H}_{int} = \sum_{\langle ij \rangle} J_{ij} D_i D_j$
(Barreto, 2000; H. M. Liu et al., 2015; Jin, L. Wang, et al., 2019), where the cou-
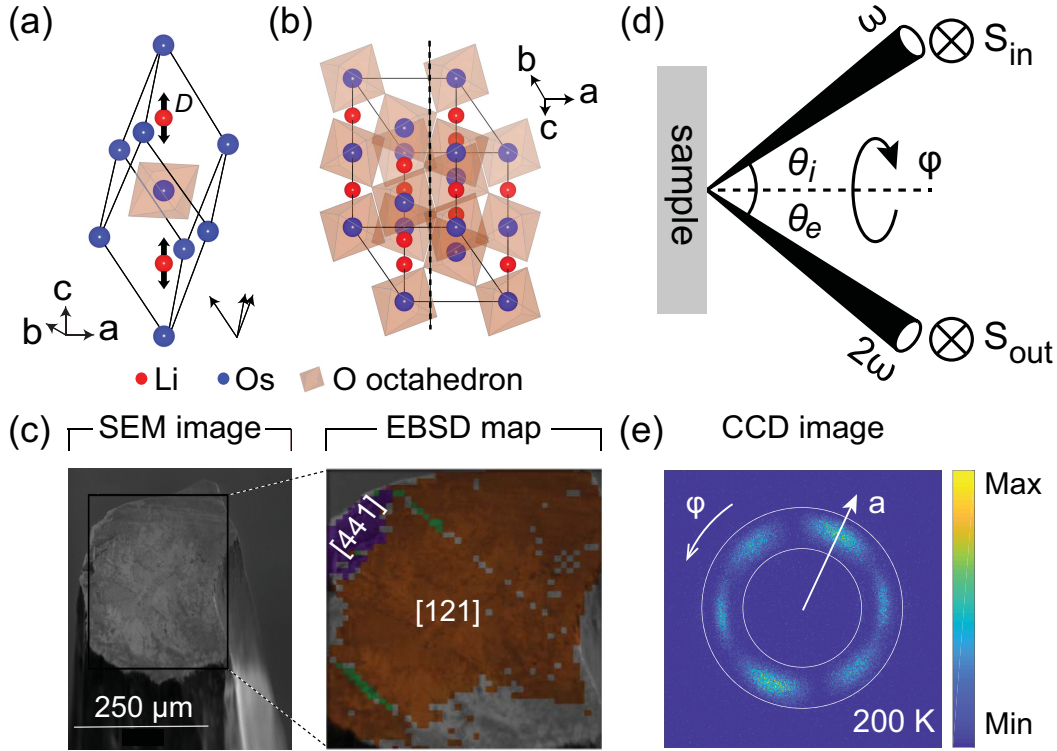pling constants J_{ij} depend sensitively on the position of atoms in the vicinity of

Figure 3.1: **a,** Crystal structure of LiOsO$_3$ in the nonpolar $R\bar{3}c$ phase. Black arrows indicate the two possible polar displacements of the Li atoms that produce the dipole moments D in the polar $R3c$ phase. Crystallographic axes on the bottom left (right) are in the hexagonal (rhombohedral) setting. **b,** Projection of the crystal structure onto the studied [121] surface. The black dashed line is the projection of the polar c axis onto this surface. **c,** Scanning electron microscopy (SEM) image and enlarged electron backscatter diffraction (EBSD) map of a typical polished [121] surface. Different colors on the EBSD map represent different crystal orientations. **d,** Schematic of the SHG-RA experiment: laser light with photon energy $\hbar\omega = 1.5$ eV is focused onto the sample at some chosen angle of incidence θ_i. The emitted SHG light at 3 eV is collected as a function of the scattering plane angle φ and the angle of emission θ_e using a CCD camera. All data shown in the main text were acquired in the S$_{\text{in}}$-S$_{\text{out}}$ polarization geometry, but data in other geometries provide consistent results. **e,** A typical raw SHG-RA data set from LiOsO$_3$ measured above T_c for a fixed θ_i. The φ and θ_e dependence are projected respectively along the azimuthal and radial directions in the CCD image. The white arrow is the crystallographic a axis.

sites i and j. The atomic positions minimize the total elastic energy of the system $E_T = \langle \mathcal{H}_{\text{int}} \rangle + \langle \mathcal{H}' \rangle$, where $\mathcal{H}'$ includes all other interactions. As the dipole correlators $\langle D_i D_j \rangle$ increase upon cooling, atomic positions will shift to readjust the balance between $\langle \mathcal{H}_{\text{int}} \rangle$ and $\langle \mathcal{H}' \rangle$ in order to minimize E_T. Therefore, $\langle D_i D_j \rangle$

can be tracked via subtle symmetry-preserving changes in atomic coordinates. By detecting such electrostrictive effects in $LiOsO_3$ using high-multipole optical second harmonic generation rotational anisotropy (SHG-RA), we reveal a wide critical region extending from T_c up to $T' \sim 230$ K, the characteristic temperature where short-range correlations start to grow. The observation of strong fluctuations suggests the presence of competing short-range interactions in the system, which is not captured by existing density functional theory or effective model calculations (H. M. Liu et al., 2015), and is consistent with specific heat data reporting a low entropy loss across T_c (Shi et al., 2013).

$LiOsO_3$ sample preparation and characterization

Single crystals of $LiOsO_3$ were prepared by solid-state reaction under high pressure and mechanically polished (roughness < 0.5 μm) along their [121] surfaces. We chose this relatively low symmetry surface to enhance sensitivity to distortions both along and perpendicular to the polar c axis (Figure 3.1b). High surface qualities were verified by scanning electron microscopy and grain boundaries were carefully identified using electron backscatter diffraction (Figure 3.1c). Light from a regeneratively amplified Ti:sapphire laser, which produces 80 fs pulses with central wavelength $\lambda = 800$ nm at a repetition rate of 100 kHz, was focused at a variable angle of incidence (θ_i) onto a 30-μm spot (FWHM) within a single [121] domain away from grain boundaries, with a fluence of 0.4 mJ/cm^2. Based on the reported optical constants of $LiOsO_3$ (Padmanabhan et al., 2018), the optical penetration depth at $\lambda = 800$ nm is around 32 nm at normal incidence, and the propagation angle of the incident light inside the sample is around 0.8 θ_i. The SHG-RA response was acquired by mechanically rotating the scattering plane about the sample surface normal and projecting the SHG light emitted at each scattering plane angle (φ) and emission angle (θ_e) onto different positions on a two-dimensional CCD detector (Figure 3.1d). A typical raw SHG-RA data set from $LiOsO_3$ is shown in Figure 3.1e, which manifests the symmetries of the [121] surface.

We tried to polish our samples to obtain other surfaces using fine sand paper. However, our samples were too small for proper polishing. We performed the electron backscatter diffraction on the scanning electron microscopy (SEM) at the Caltech department of geology. The determination result of the sample surface is similar to the X-ray diffraction result.
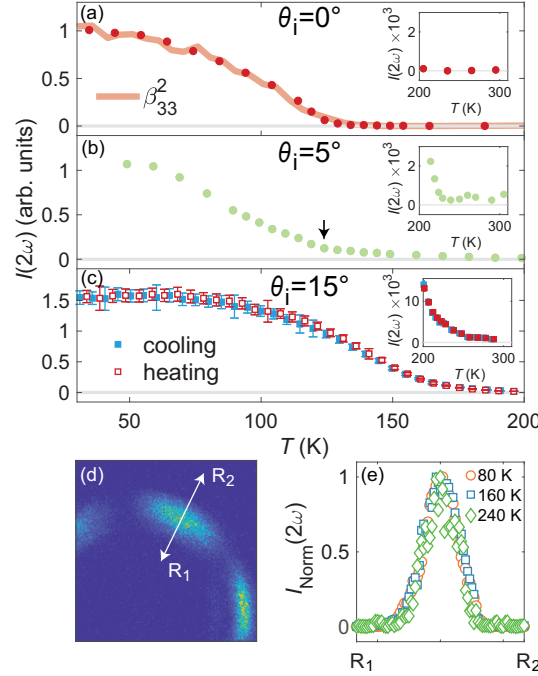
Figure 3.2: **a–c,** Temperature-dependent SHG intensity from $LiOsO_3$ at fixed φ and $\theta_i = 0°, 5°$, and $15°$, all scaled to the intensity of the $\theta_i = 0°$ curve at base temperature. The intensities are integrated over the θ_e range bounded by the concentric white circles shown in Figure 3.1e. Insets show a close-up on the temperature range between 200 K and 300 K. The square of the Li displacement parameter β_{33} reported in a neutron diffraction study (Shi et al., 2013) is overlaid on the normal incidence data (panel a). We shifted the reported β_{33} curve downwards by 8 K to account for laser heating of the sample in our experiments. The black arrow (b) indicates the kink mentioned in the main text. No difference between cooling and heating curves was observed. **d,** The θ_e dependence of the SHG intensity is extracted from a cut along the radial direction of the CCD image. **e,** The normalized intensity profile along a radial cut from R_1 to R_2 taken at different temperatures.

Angle-of-incidence dependent SHG measurement

Below T_c the electric-dipole (ED) contribution to SHG, governed by a third-rank susceptibility tensor χ_{ijk}^{ED} that relates the induced polarization at twice the frequency of the incident electric field via $P_i(2\omega) = \chi_{ijk}^{ED} E_j(\omega) E_k(\omega)$, becomes allowed due to the loss of inversion symmetry (Boyd, 2020). Previous work has shown that χ_{ijk}^{ED} is linearly proportional to the polar order parameter and dominates the low-temperature SHG response from $LiOsO_3$ (Padmanabhan et al., 2018). However, in the centrosymmetric state above T_c, a finite SHG response can still arise from higher-multipole radiation, such as via an electric quadrupole (EQ) process $P_i(2\omega) = \chi_{ijkl}^{EQ} E_j(\omega) \nabla_k E_l(\omega)$, which is highly sensitive to symmetry-preserving

lattice distortions (Ron, Zoghlin, et al., 2019), or a magnetic dipole process, which can be ruled out in our case. To detect and isolate the EQ from the ED contribution in LiOsO$_3$, we performed angle-of-incidence dependent SHG measurements in the S$_{in}$-S$_{out}$ geometry. In this geometry, the electric field polarizations of both the incident and detected SHG light are perpendicular to the scattering plane and maintain a fixed orientation relative to the sample as θ_i is varied. Therefore, the ED contribution will be independent of θ_i whereas the EQ contribution will change with θ_i by virtue of its dependence on the light wave vector. Because our measurements are particularly sensitive to the Os-O sublattice symmetry at the chosen photon energies, the EQ contribution to the SHG intensity in the high-temperature centrosymmetric state should scale approximately as $\sin^2 \theta_i$. Therefore, we expect the EQ contribution to be significantly enhanced away from normal incidence (Y. Zhang et al., 2019; Bloembergen, Chang, et al., 1968).

Figure 3.2a shows that at $\theta_i = 0°$, we detect no SHG signal above T_c and a large intensity upturn just below T_c. The intensity scales with the square of the average Li atom displacement β_{33} extracted from neutron diffraction data (Shi et al., 2013), which is reproduced in Figure 3.2a. This is consistent with an ED dominated signal where all χ_{ijk}^{ED} elements scale linearly with the polar order parameter β_{33}, in accordance with a previous normal incidence SHG study (Padmanabhan et al., 2018). With a small increase of θ_i to 5°, we detect a finite SHG intensity even at 300 K, which starts to grow below a characteristic temperature $T' \sim 230$ K. The onset of the ED contribution at T_c is slightly smeared out but remains identifiable via a kink in the SHG intensity (Figure 3.2b). As θ_i increases further to 15°, the SHG signal at 300 K becomes even stronger and again exhibits an upturn below T'. Now the kink at T_c is completely obscured (Figure 3.2c). No thermal hysteresis was observed in any measurement, consistent with a continuous phase transition.

The pronounced angle-of-incidence dependence of the high-temperature SHG intensity is incompatible with an ED process. This rules out the possibility of localized polar nano-regions, which generate SHG above T_c in insulating ferroelectrics (Pugachev et al., 2012). Moreover, in the case of randomly oriented polar domains, one expects significant incoherent (hyper-Rayleigh) scattering (Dolino, 1972; Melnikov, Nikulin, and Aktsipetrov, 2003), manifested as the emission of second harmonic radiation over a broad range of angles around the specular direction $\theta_e = \theta_i$ (Figure 3.1d). Figure 3.2d and 3.2e show the θ_e dependence of the SHG intensity at a constant φ, which shows a sharp peak in the specular direction with no measurable

broadening over a wide temperature range across T_c. We also found the ratio between the high-temperature SHG intensities at $\theta_i = 5°$ and $\theta_i = 15°$ (Figure 3.2b and 3.2c) to be consistent with a $\sin^2 \theta_i$ scaling (ignoring the weak θ_i-dependence of the Fresnel coefficients over this range (Padmanabhan et al., 2018)). Taken altogether, our data show that changes in the SHG signal above T_c can be attributed to changes in the coherent EQ SHG response arising from lattice distortions.
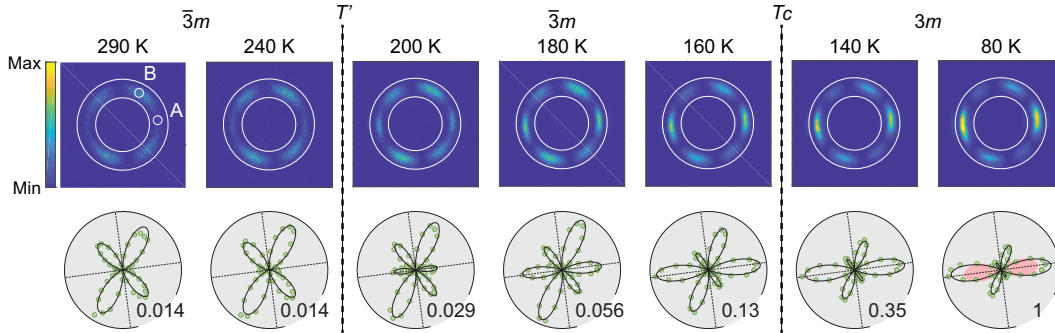

Figure 3.3: The top row shows raw SHG-RA data sets from LiOsO$_3$ at select temperatures taken with a fixed $\theta_i = 15°$. The bottom row shows polar plots of the data (green circles) obtained by radially integrating the raw data between the concentric white circles shown in the top row. Fits to the simplified hyperpolarizable bond model are superposed (black lines). For the 80 K fit we include an ED SHG contribution, with a functional form based on the experimental normal incidence RA pattern (pink shaded region). The intensity scale in the bottom row is normalized to the 80 K value. The dashed black lines in the bottom row indicate the angles parallel and perpendicular to the fastest growing lobe. Lattice point groups are labeled above.

To understand the nature of the distortions above T_c, we measured the temperature dependence of the full SHG-RA patterns at $\theta_i = 15°$ where the EQ SHG contribution is pronounced. At $T = 290$ K the SHG-RA pattern consists of four lobes with alternating amplitude. This fits the functional form predicted from a symmetry-based calculation of bulk EQ SHG from [121] oriented LiOsO$_3$. No changes in either the magnitude or the shape of the SHG-RA pattern are observed down to T' (Figure 3.3), consistent with a weak uniform thermal contraction of the lattice over this temperature range (Shi et al., 2013). On the other hand, in the region bounded by T' and T_c, we observe drastic changes to the shape of the patterns and the emergence of two additional intensity lobes. These changes do not lower the symmetry of the patterns and can be accounted for simply by adjusting the relative magnitudes of the χ_{ijkl}^{EQ} elements allowed in the nonpolar $\bar{3}m$ point group. We cannot reliably extract χ_{ijkl}^{EQ} values because the fits are under-determined, especially considering the
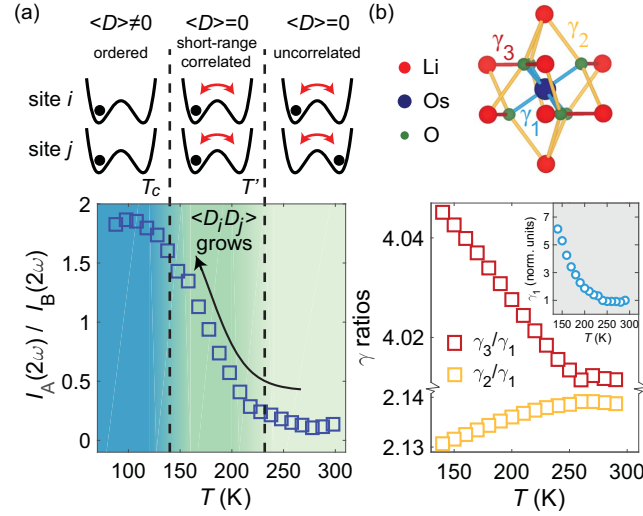
Figure 3.4: **a,** The ratio of the SHG intensities at scattering plane angles A and B (see Figure 3.3) as a function of temperature. The evolution of dipolar correlations deduced from our data is illustrated above. Two neighboring sites are shown for each temperature range, and the black curves show the free energy potentials as a function of the Li polar displacement. For $T > T'$, local moments are already formed, but there is negligible correlation between sites. The local moment orientation, denoted by the location of the black dot in the double-well potential, fluctuates randomly. For $T_c < T < T'$, moments continue to fluctuate but short-range correlations develop. For $T < T_c$, moments become static long-range ordered. **b,** The hyperpolarizabilities included in our SHBM are shown above. The extracted values of γ_2/γ_1, γ_3/γ_1, and γ_1 (inset) at each temperature obtained through fitting the SHG-RA patterns.

χ_{ijkl}^{EQ}'s can be complex for absorbing materials, but the important observation is their atypical nonuniform temperature dependence. This indicates that a nonuniform but symmetry-preserving lattice distortion, i.e., a polymorphous representation of the $R\bar{3}c$ structure, takes place between T' and T_c, revealing an extended critical region over which $\langle D_i D_j \rangle$ grows from dissimilar Li displacements that are correlated over the probe volume. Upon further cooling below T_c, the SHG intensity continues to rise, but the shape of the SHG-RA patterns does not evolve appreciably. This is to be expected once ED SHG starts to dominate the signal because all elements of χ_{ijk}^{ED} are linearly proportional to the polar order parameter. This means that the relative magnitudes of all χ_{ijk}^{ED} elements are constant, which fixes the pattern shape. The full temperature evolution of the pattern shape can be quantified by plotting the intensity ratio of lobes A and B defined in Figure 3.3. As shown in Figure 3.4a, this intensity ratio grows steeply between T' and T_c but is temperature independent outside this window, in stark contrast to the behaviors of the intensities alone (Figure 3.2).
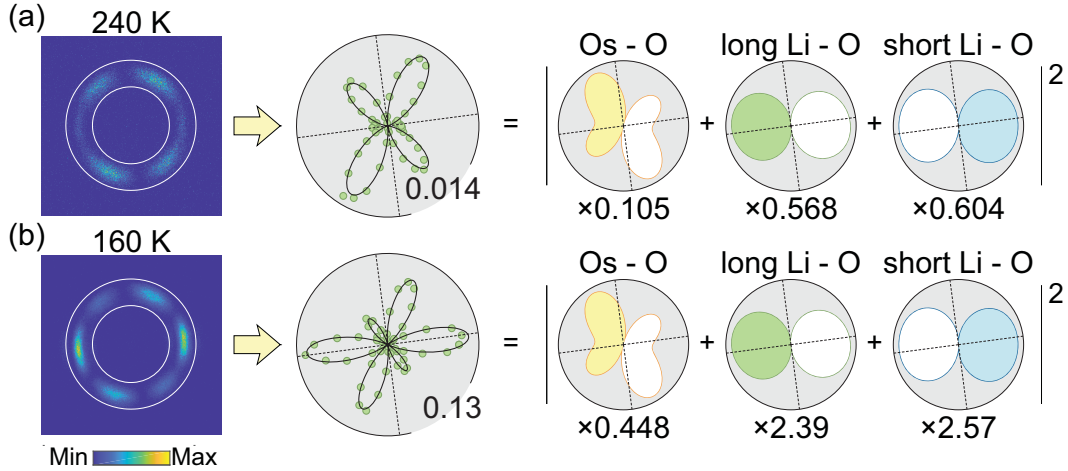
Figure 3.5: Example fits of the SHG-RA data at **a,** 240 K and **b,** 160 K to the SHBM. The first column shows the raw data. The second column shows the angular dependence of the SHG intensity obtained by radially integrating the raw data between the region bounded by the concentric white circles. Black curves are the SHBM fits. The third column shows the contributions from the Os-O bonds, the long Li-O bonds, and the short Li-O bonds obtained from fitting, with their fitted magnitudes written below. Shaded (unshaded) areas indicate positive (negative) amplitudes.

The simplified hyperpolarizable bond model

We explored the microscopic origin of the SHG-RA pattern evolution by considering a simplified hyper-polarizable bond model (SHBM) (Powell, J.-F. Wang, and Aspnes, 2002; Bauer and Hingerl, 2017). This model treats the crystal as an array of charged anharmonic oscillators centered at the chemical bonds, with motion constrained along the bond directions. The nonlinear susceptibilities of individual oscillators are calculated by solving classical equations of motion, and then summed together to form a bulk nonlinear susceptibility. An expression for $\chi_{ijkl}^{\mathrm{EQ}}$ derived from a SHBM has been shown to take the form $\chi_{ijkl}^{\mathrm{EQ}} \propto \sum_n \gamma_n^\omega \gamma_n^{2\omega} (\hat{b}_n \otimes \hat{b}_n \otimes \hat{b}_n \otimes \hat{b}_n)_{ijkl}$, where γ_n^ω and $\gamma_n^{2\omega}$ are the linear and second-order (hyper-) polarizabilities of the nth bond, $\hat{b}_n$ is a unit vector pointing along the nth bond, and all bond charges are assumed equal. For LiOsO$_3$, we included all three types of bonds in the unit cell: the Os-O bonds, the long Li-O bonds between adjacent c planes, and the short Li-O bonds in the same c planes (Benedek and Birol, 2016), with hyper-polarizabilities γ_1, γ_2, and γ_3, respectively (Figure 3.4b). No measurable change in the linear optical response at 1.5 eV or 3 eV has been detected over the temperature range studied here (Lo Vecchio et al., 2016; Laurita et al., 2019), so we assume that the

values of γ_n^ω are temperature independent. We also keep $\hat{\mathbf{b}}_n$ values constant, leaving only the $\gamma_n^{2\omega}$ as fit parameters (Figure 3.4). The $\hat{\mathbf{b}}_n$'s of the bonds are obtained from reported neutron diffraction data at 300 K (Shi et al., 2013) to be as follows. Note the primitive vectors are (units in Å): $\mathbf{a} = (5.06, 0, 0)$, $\mathbf{b} = (-2.53, 4.39, 0)$, and $\mathbf{c} = (0, 0, 13.2)$.

<div align="center">Os-O bonds:</div>

$$\hat{\mathbf{b}}_1 = (-0.482, -0.668, 0.566),$$
$$\hat{\mathbf{b}}_2 = (0.820, -0.0832, 0.566),$$
$$\hat{\mathbf{b}}_3 = (-0.338, 0.752, 0.566),$$
$$\hat{\mathbf{b}}_4 = (0.482, 0.668, -0.566),$$
$$\hat{\mathbf{b}}_5 = (-0.820, 0.0832, -0.566),$$
$$\hat{\mathbf{b}}_6 = (0.338, -0.752, -0.566).$$

<div align="center">Long Li-O bonds:</div>

$$\hat{\mathbf{b}}_7 = (0.344, 0.477, 0.808),$$
$$\hat{\mathbf{b}}_8 = (-0.685, 0.0593, 0.808),$$
$$\hat{\mathbf{b}}_9 = (0.241, -0.537, 0.808),$$
$$\hat{\mathbf{b}}_{10} = (-0.344, -0.477, -0.808),$$
$$\hat{\mathbf{b}}_{11} = (0.685, -0.0593, -0.808),$$
$$\hat{\mathbf{b}}_{12} = (-0.241, 0.537, -0.808).$$

<div align="center">Short Li-O bonds:</div>

$$\hat{\mathbf{b}}_{13} = (-1, 0, 0),$$
$$\hat{\mathbf{b}}_{14} = (0.5, 0.866, 0),$$
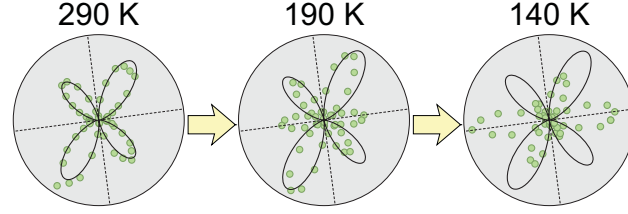$$\hat{\mathbf{b}}_{15} = (0.5, -0.866, 0).$$

Figure 3.6: Measured SHG-RA patterns (green circles) at 290 K, 190 K, and 140 K. Black curves show patterns calculated using the SHBM, where the $\gamma_n^{2\omega}$ values are fixed to the best fit values for the 290 K data, and the $\hat{\mathbf{b}}_n$'s are varied at each temperature based on neutron diffraction data.

The change in bond directions $\hat{b}_n$ alone based on neutron diffraction data (Shi et al., 2013) is also too small to account for the observed changes in $\chi_{ijkl}^{\mathrm{EQ}}$ within the SHBM. Therefore, the γ_n^ω and $\hat{b}_n$ are held fixed in our analysis, and the hyper-polarizabilities are the only free parameters. To validate our approximation that the $\hat{\mathbf{b}}_n$ values are constant, we also calculated SHG-RA patterns by fixing $\gamma_n^{2\omega}$ at all temperatures and only changing the $\hat{\mathbf{b}}_n$'s according to lattice parameters reported by neutron diffraction. As shown in Figure 3.6, the calculated SHG-RA patterns hardly change over the interval $T' > T > T_c$ and cannot account for our observations.

Best fits of this SHBM to our SHG-RA data are shown in the bottom panels of Figure 3.3, from which we obtain the temperature dependence of γ_1, γ_2, and γ_3. We find that while all hyper-polarizability values grow upon cooling, a small decrease (increase) in γ_2/γ_1 (γ_3/γ_1) occurring over the critical region is responsible for the large shape changes observed in the SHG-RA data (Figure 3.4b). Knowing that uniform thermal contraction above T' does not affect the shape of the SHG-RA patterns, we can assume that the scaling between the change in bond hyper-polarizability and the change in bond length is the same for different bonds. Therefore, the critical region must be characterized by nonuniform changes in the short and long Li-O bond lengths.

Discussion and conclusions

A microscopic picture of the temperature evolution of dipole correlations in $LiOsO_3$ deduced from our electrostriction measurements is presented in the top panels of Figure 3.4a. Our finding of an extended critical region across $T_c < T < T'$ in $LiOsO_3$ corroborates the predominantly order-disorder character of the polar transition and points to the presence of significant dipolar correlations developing below T'. This may explain the low entropy loss across T_c found in specific heat (Shi et al., 2013),

the unusual increase in linewidth of the ^3E_g Li in-plane vibrational mode below $\sim T'$ observed by Raman scattering (Jin, L. Wang, et al., 2019), as well as the weakly nonuniform changes occurring in the a and c lattice parameters below $\sim T'$ measured by neutron diffraction (Shi et al., 2013). The fact that previous Curie-Weiss analyses of dielectric susceptibility data were performed inside the critical region may also be responsible for the unusually low value of the extracted Curie-Weiss temperature (Jin, L. Wang, et al., 2019). An extended critical region is not accounted for in existing 3D Ising-type models with purely ferroic interactions, which were proposed based on density functional theory calculations (H. M. Liu et al., 2015). There is also no evidence for spatially anisotropic interactions in the Hamiltonian that would lead to effectively lower dimensionality and hence enhanced fluctuations (H. M. Liu et al., 2015). Instead, it is possible that enhanced fluctuations arise from the geometric origin of Li off-centering—competing interactions from different signs of J_{ij} arising owing to different neighbor distances. The nonuniform change in the short and long Li-O bonds serves to partially relieve the multiple nearly degenerate displacements. Our findings should guide further theoretical work in search of a detailed microscopic mechanism, which can in turn lead to more refined and quantitative models of the SHG response that go beyond our phenomenological treatment. More generally, our technique can be applied broadly to understand critical phenomena in geometric ferroelectrics, for which many polar metals are an effective subclass, as well as other metals with broken inversion symmetry, such as topological semimetals. It would also be interesting to explore signatures of critical fluctuations in other related nonlinear optical responses such as the photogalvanic effect, which has recently been shown to be a symmetry-sensitive probe of noncentrosymmetric topological semimetals (Ma et al., 2017; Rees et al., 2020). Since electric field cannot penetrate into metals, we cannot apply an electric field to reverse the direction of the polar order. However, we can potentially try to flow electric current through $LiOsO_3$ or other polar metals to reverse their polar order.

Chapter 4

NONTHERMAL OPTICAL ENGINEERING OF ELECTRONIC AND OPTICAL PROPERTIES

4.1 The coherent Floquet formalism

Introduction

In Chapter 1.2 we introduced several ways where we can use a strong laser beam to modify the material properties. A lot of these methods involve some sort of excitations–be it electrons, magnons, or phonons, so the light is absorbed. This absorption of light poses two problems. The first one is that the light absorption will finally lead to heating and even damage to the material. Figure 4.1 shows the microscopic image of a sample surface with burning holes caused by strong optical heating from a focused beam. The second problem is that the excitations need time (typically from hundred femtoseconds to hundred picoseconds) to decay, so after the material properties get modulated, we have to wait some time for the material to return to its original state. This is not ideal in high-speed applications.
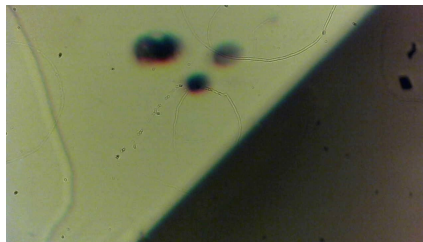

Figure 4.1: The burning holes from optical heating.

Therefore, we need a way for light to modulate material properties without being absorbed. An ideal situation is that the periodic driving with light can change the effective Hamiltonian of the system so that the ground state of the effective Hamiltonian has different properties from the original ground state. In this way, we do not need excitations to transform the material properties, and the modulation speed can be very fast, limited only by how fast we can shape our pump pulse to be.

A question we need to pay attention to is that, when the systen Hamiltonian is time dependent as introduced by the periodic driving with light, is there still a notion of ground state, or any energy spectrum consisting of the eigenenergies and eigenstates,

since the energy is not conserved in the system? The answer is yes, if we take a time average. Based on the differential equation theories developed by the French mathematician Gaston Floquet (1847–1920), we can convert the time-dependent Hamiltonian to a time-independent one (Shirley, 1965) and solve for the eigenstates of this time-independent Floquet Hamiltonian.

Normally, when we solve the time-dependent Schrödinger equation and specify an initial condition, we can get the time evolution of the given state. If the Hamiltonian is time-independent, the only phase factor is $\exp(iEt/\hbar)$, where E is the energy of a given eigenstate. If the Hamiltonian is time-dependent, though, things get more complicated. In the Floquet formalism, however, we can convert the original time-dependent Hamiltonian into a time-independent Floquet Hamiltonian. This does not come for free. We have to at the same time expand our Hilbert space to be a tensor product between the original Hilbert space and an infinite dimensional Floquet space. Each Floquet sector in the Floquet space has a different phase factor $\exp[i(E + n\hbar\Omega)t/\hbar]$, where Ω is the driving frequency and n labels the order of the Floquet state in the infinite dimensional Floquet space. The solution obtained from this Floquet formalism is exact. It is at the same time convenient since we can solve the dynamical Hamiltonian using the same methods as the ones used in solving a static Hamiltonian, and we can extract "quasi-energies" which are useful for predicting properties of strongly-driven materials.

Theories

We start from the Floquet's theorem, which is very similar to the Bloch's theorem for solving the electronic wavefunctions in a spatially periodic potential. Consider a time-periodic Hamiltonian $H(t) = H(t + T)$. Floquet's theorem states that the system's evolution can be expanded by a complete basis consisting of the Floquet states $|\psi_n(t)\rangle$, where

$$|\psi_n(t)\rangle = e^{-i\varepsilon_n t/\hbar}|\Phi_n(t)\rangle, \tag{4.1}$$

and $|\Phi_n(t)\rangle$ is a periodic function in time with a period T. The quantity ε_n is called the quasi-energy. Therefore, we can Fourier transform $|\Phi_n(t)\rangle$ to be

$$|\Phi_n(t)\rangle = \sum_m e^{-im\Omega t}|\phi_n^{(m)}\rangle. \tag{4.2}$$

Our goal is to solve for $|\phi_n^{(m)}\rangle$. With this formalism, we can define the Floquet Hamiltonian H_F to be (Rudner and Lindner, 2020)

$$
\begin{bmatrix}
\ddots & H^{(-1)} & & H^{(-2)} & \\
H^{(1)} & H^{(0)} - m\hbar\Omega & & H^{(-1)} & & H^{(-2)} \\
H^{(2)} & H^{(1)} & & H^{(0)} - (m+1)\hbar\Omega & H^{(-1)} \\
& H^{(2)} & & H^{(1)} & & \ddots
\end{bmatrix},
\tag{4.3}
$$

or $(H_f)_{mn} = \frac{1}{T} \int_0^{2\pi/\Omega} e^{i\Omega t(m-n)} H(t) - n\hbar\Omega\delta_{mn}$, where $H^{(i)}$ is the i-th element Fourier series of the original Hamiltonian H. Each block in equation 4.3 is an $n \times n$ dimensional matrix where n is the dimension of the original Hamiltonian. Then we can solve for the eigenstates of the Floquet Hamiltonian H_f as $H_f\varphi_n = \varepsilon_n\varphi_n$, where we can get the $|\phi_n^{(m)}\rangle$ through φ_n, which we decompose into

$$
\begin{bmatrix}
\vdots \\
|\phi_n^{(m)}\rangle \\
|\phi_n^{(m+1)}\rangle \\
\vdots
\end{bmatrix}.
\tag{4.4}
$$

Throughout this derivation note that n labels the states in the original Hilbert space, and m labels the Floquet sectors. After having solved for $|\phi_n^{(m)}\rangle$ we can use Equation 4.1 and 4.2 to get the solutions to the time-dependent Hamiltonian.

Heating management

Despite intense theoretical interests on using Floquet engineering to drastically alter electronic and magnetic properties by optically inducing non-trivial band topologies (Oka and Aoki, 2009; Kitagawa et al., 2011; Rudner and Lindner, 2020; Hübener et al., 2017) and emergent spin interactions (Mentink, Balzer, and Eckstein, 2015; Claassen et al., 2017; J. Liu, Hejazi, and Balents, 2018; Chaudhary, Hsieh, and Refael, 2019), there have been very few experimental realizations (Y. H. Wang et al., 2013; McIver et al., 2020). The main obstacle is heating due to absorption of light. In this part we focus on two types of heating: steady-state heating and transient heating.

In the steady-state heating, the absorption of the laser power by the excited area is totally compensated by the heat conduction out of the excited area. The steady-state (average) heating induced temperature rise can be calculated as (Jiang and Ban, 2020)

$$
\Delta T = \sqrt{\frac{\ln 2}{\pi}} \frac{P}{\kappa d},
\tag{4.5}
$$

where P is the average laser power, κ is the thermal conductivity, and d is the FWHM beam diameter.

For transient heating, with sufficient time after the pump pulse is gone, the excited area has reached a thermal equilibrium but the heat diffusion has not taken place. The pump pulse energy Q has been absorbed by the excited area of the material and the temperature rise depends on the heat capacity c, which is often temperature dependent. The transient temperature rise ΔT from the base temperature T_0 can be calculated as

$$Q = \int_{T_0}^{T_0 + \Delta T} c(T)\mathrm{d}T. \tag{4.6}$$

The transient temperature rise is often much larger than the steady-state temperature rise.

4.2 Floquet engineering of band gap and SHG in MnPS$_3$
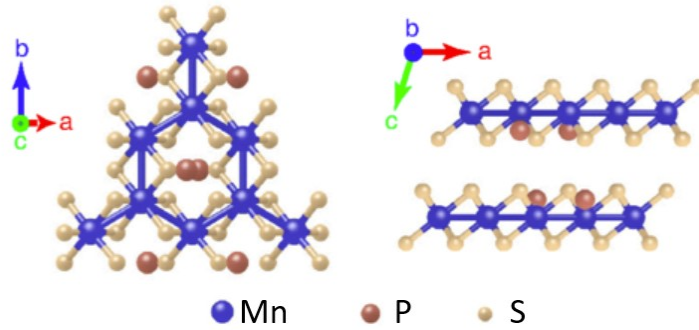
Introduction

Figure 4.2: The crystal structure of MnPS$_3$, viewed along the c (left) and b (right) axis. Taken from Chu et al., 2020.

As we have shown in Chapter 4.1, a strong periodic driving with light can change the effective energy spectrum of materials, therefore modulating their properties. In this section we will demonstrate coherent control and giant modulation of optical nonlinearity in a van der Waals layered magnetic insulator MnPS$_3$ (Shan, Ye, et al., 2021). By driving far off-resonance from the lowest on-site Mn d-d transition, we observe a coherent on-off switching of its optical second harmonic generation efficiency on the timescale of 100 femtoseconds with no measurable dissipation. At driving electric fields of order 10^9 V/m, the on-to-off ratio exceeds 10, limited only by the sample damage threshold. Floquet theory calculations (Shirley, 1965) based on a single-ion model of MnPS$_3$ are able to quantitatively reproduce the measured
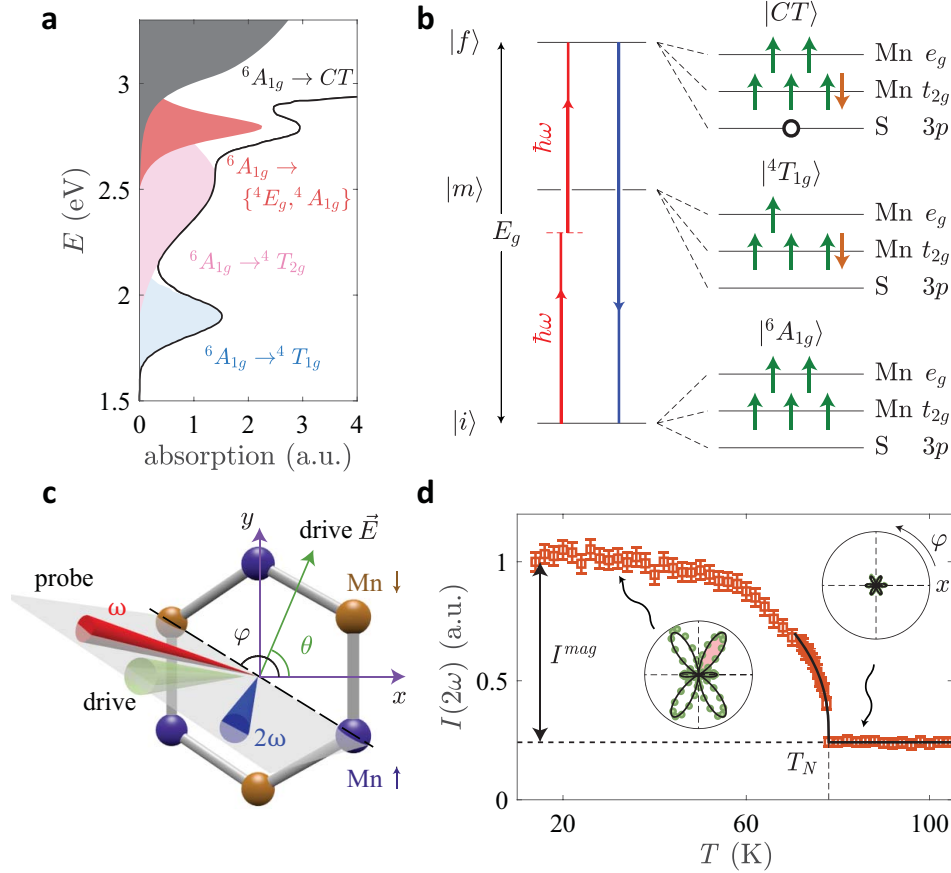
Figure 4.3: Static SHG from MnPS$_3$. **a,** Absorption spectrum of MnPS$_3$ (black curve) and underlying optical transitions (shaded areas) adapted from Grasso et al., 1991. **b,** Left: Black horizontal lines denote the initial, intermediate, and final multi-electron states involved in the resonant ED-SHG process (red and blue arrows). Right: Orbital and spin configurations of the states. **c,** Depiction of the experimental geometry and the antiferromagnetic spin arrangement on the Mn sublattice. The probe beam (red) is focused obliquely onto the sample, and the reflected SHG beam (blue) is measured as a function of the scattering plane angle φ. Both incident and reflected beams are linearly polarized in the scattering plane. The driving beam (green) is focused normally onto the sample with linear polarization along θ. The x and y axes correspond to the crystallographic a and b axes. **d,** Temperature-dependent SHG intensity acquired at $\varphi = 60°$ (pink lobe in inset) normalized by its value at 10 K. The error bars represent the standard errors of the mean from four independent measurements. A power law fitting with $\beta = 0.32(2)$ is overlaid (black curve). Insets show RA-SHG patterns above and below T_N (green circles) and fits to the single-ion model (black curves).

driving field amplitude and polarization dependence of the effect. Our approach can be applied to a broad range of insulating materials, raising the possibility of dynamically designed nonlinear optical elements.

The ability to widely tune the optical nonlinearity of a material with ultrafast speed is crucial for advancing photonics technologies spanning optical signal processing, on-chip nonlinear optical sources and optical computing. However, the nonlinear optical properties of materials, dictated by their electronic and crystallographic structures, are largely set at the synthesis and fabrication stages. Further in situ tuning may be achieved by changing temperature, pressure (Bayarjargal and Winkler, 2013), electric field (Terhune, Maker, and Savage, 1962), current density (An et al., 2013; Ruzicka et al., 2012) or carrier concentration (Seyler et al., 2015; Soavi et al., 2018), but these approaches are static and often materials specific. Dynamical tuning based on light-induced phase transitions (Satoh et al., 2007; M. Y. Zhang et al., 2019) or photo-carrier density modulation (Sartorello et al., 2016) have previously been demonstrated. However, these approaches impart significant heating and are limited in speed due to electronic and structural relaxation bottlenecks.

Floquet engineering potentially offers a non-thermal and broadly applicable strategy to modulate nonlinearity on ultrashort timescales limited only by the drive pulse duration. However, appreciable tuning requires strong driving (pump) electric fields E^{pu}. To determine the required field strength, we note that the typical length scale in the systems is the atomic spacing a, which is on the order of several angstroms, and the typical energy scales of Floquet problems are on the order of $\sim$ eV. Therefore, in Floquet problems a field on the order of $10^9 \sim 10^{10}$ V/m is required. We can demonstrate this general order of magnitude in two more concrete examples. In Floquet engineering of the spin exchange interaction, significant effects require a Floquet parameter $\mathcal{E} \equiv \frac{eaE^{\text{pu}}}{\hbar\Omega}$ of order unity, where e is the electron charge and $\hbar\Omega$ is the driving photon energy, which is $\sim$ eV if we use visible or near-infrared frequencies (Mentink, Balzer, and Eckstein, 2015). In Floquet engineering of the energy spacing between states, more commonly known as the optical Stark effect (Sie, McIver, et al., 2015), the energy shift $\Delta E_{OS} \propto \frac{(E^{\text{pu}})^2}{E_0 - \hbar\Omega}$, where E_0 is the unperturbed energy spacing (such as the bandgap). Common E_0 and $\hbar\Omega$ are on the order of $\sim$ eV. This strong requisite field makes runaway heating a major obstacle to experimentally realizing Floquet engineering. To mitigate this effect, we focus on driving electrical insulators below their bandgap.

The layered honeycomb lattice magnetic insulator $MnPS_3$ (Figure 4.2) is an ideal demonstration platform for the following reasons: (i) It exhibits a large direct bandgap E_g= 3.1 eV in the visible region (Piryatinskaya et al., 2012). (ii) The Mn^{2+} moments adopt a Néel antiferromagnetic (AFM) arrangement that breaks the

inversion symmetry of its underlying lattice, allowing a finite second-order optical nonlinearity in the electric-dipole (ED) channel. This has recently been detected by optical second harmonic generation (SHG) measurements with an SHG photon energy resonant with E_g (Chu et al., 2020). (iii) The relatively low AFM ordering temperature (T_N = 78 K) allows thermal versus non-thermal induced effects to be readily distinguished. (iv) The timescale for spin dynamics, set by the magnetic exchange interaction, is around 5 ps (Kurosawa, Saito, and Yamaguchi, 1983). Therefore, all dynamics can be confined to the charge sector by driving with femtosecond pulses. (v) Because the Mn $3d$ electrons are highly localized, the optical response and transport properties of $\mathrm{MnPS_3}$ are well captured within a single ion picture (Grasso et al., 1991), which enables an analytical derivation of Floquet engineering effects from a microscopic model.

Microscopic single-ion model

We first developed a single ion model to understand the AFM order induced static SHG from $\mathrm{MnPS_3}$. This response is dominated by an ED process of the form $P_i(2\omega) = \chi_{ijk}^{\mathrm{ED(c)}} E_j^{\mathrm{pr}}(\omega) E_k^{\mathrm{pr}}(\omega)$, where the c-type (Fiebig, Pavlov, and Pisarev, 2005) (time-reversal odd) second-order susceptibility tensor $\chi_{ijk}^{\mathrm{ED(c)}}$ governs the relationship between the incident (probe) electric field $E_i^{\mathrm{pr}}(\omega)$ and the polarization induced at twice the incident probing frequency $P_i(2\omega)$, and the indices run over the x, y, and z coordinates. For a near resonant process where $2\hbar\omega \approx E_\mathrm{g}$, the quantum mechanical expression for $\chi_{ijk}^{\mathrm{ED(c)}}$ is given by (Boyd, 2020)

$$\chi_{ijk}^{\mathrm{ED(c)}} \propto \sum \frac{\langle i|r_i|f\rangle \langle f|r_j|m\rangle \langle m|r_k|i\rangle}{(E_f - E_i - 2\hbar\omega - i\gamma_f)(E_m - E_i - \hbar\omega)}, \qquad (4.7)$$
$$+ (j \leftrightarrow k)$$

where the sum is performed over $\mathrm{Mn^{2+}}$ ions in a unit cell, $|i\rangle$, $|m\rangle$, and $|f\rangle$ are the ground, intermediate, and final states of the SHG process, E_i, E_m and E_f denote their respective energies and γ_f is a phenomenological decay rate of the final state. In the presence of an octahedral crystal field imposed by the sulfur ions, the five-fold degenerate Mn $3d$ orbitals split into a low-energy t_{2g} triplet and a high-energy e_g doublet. The ground state is a high-spin ($S = 5/2$) state characterized by a $t_{2g}^3 e_g^2$ orbital configuration with even-parity $^6A_{1g}$ symmetry. According to prior optical absorption measurements (Figure 4.3a) (Grasso et al., 1991), the intermediate state has predominantly $^4T_{1g}(t_{2g}^4 e_g^1)$ character (even-parity, $S = 3/2$) and the final state has predominantly S $3p \rightarrow$ Mn $3d$ charge transfer (CT) character (odd-parity, $S = 5/2$). By introducing spin-orbit coupling λ and a trigonal distortion of the crystal field η as

perturbations to the states described above (Muthukumar, Valentí, and Gros, 1995), optical transitions $|i\rangle \rightarrow |m\rangle$ and $|m\rangle \rightarrow |f\rangle$ become ED allowed (Figure 4.3b). Upon coherently summing the single-ion contributions from two Mn^{2+} sites in the unit cell, one obtains $\chi_{ijk}^{ED(c)} \propto \beta_{ijk}\lambda^2\eta(\langle S_{z,1}\rangle - \langle S_{z,2}\rangle)$, where $(\langle S_{z,1}\rangle - \langle S_{z,2}\rangle)$ is the staggered moment perpendicular to the honeycomb plane. The coefficient β_{ijk} encodes the CT transition matrix elements that, by construction, are unequal along x and y due to coupling between the *ABC* stacked honeycomb layers.

The Néel order in MnPS$_3$

To verify this static SHG model, we performed rotational anisotropy (RA) measurements using near resonant probe light ($\hbar\omega = 1.55$ eV). The beam was focused obliquely onto a bulk MnPS$_3$ single crystal and specular reflected SHG light was collected as a function of the scattering plane angle φ (Figure 4.3c). Above T_N we observe a weak temperature-independent SHG signal arising from i-type (time-reversal even) higher multipole bulk crystallographic SHG processes (Figure 4.3d), consistent with a previous report (Chu et al., 2020). Below T_N the intensity, collected at $\varphi = 60°$, undergoes a steep upturn that can be fitted to a power law $\chi_{ijk}^{ED(c)} \propto (T_N - T)^\beta$ with $\beta = 0.34$. This is in excellent agreement with the critical exponent of the AFM order parameter ($\beta = 0.32$) obtained from neutron diffraction (Wildes et al., 2006), confirming its linear coupling to $\chi_{ijk}^{ED(c)}$ as predicted in our model. The enhanced anisotropy of the RA pattern below T_N arises from interlayer coupling and is fully captured in our model through the β_{ijk} coefficient (Figure 4.3d inset).

Floquet dynamical model

Next, we study how an electric field oscillating at sub-gap frequency affects the electronic spectrum of MnPS$_3$ within our single ion model. Since this drive mainly hybridizes $|i\rangle$ and $|f\rangle$ due to their opposite parity and equal spin, the three-level problem can be simplified to a two-level one, described by the following time-dependent Hamiltonian

$$H(t) = H_0 + e\vec{r} \cdot \vec{E}^{pu} \cos \Omega t, \tag{4.8}$$

where H_0 is the un-perturbed 2×2 Hamiltonian. By diagonalizing the time-independent Floquet Hamiltonian (Rudner and Lindner, 2020)

$$(H_f)_{mn} = \frac{1}{2\pi/\Omega} \int_0^{2\pi/\Omega} e^{i\Omega t(m-n)} H(t) - n\hbar\Omega\delta_{mn} \tag{4.9}$$
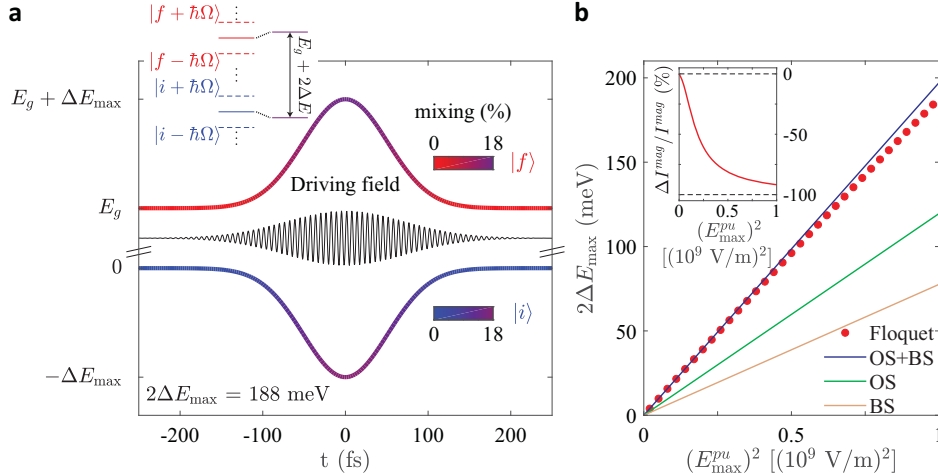
Figure 4.4: Coherent drive-induced state modification. **a,** Calculated temporal profile of the energy shift and mixing amplitude of the initial (blue) and final (red) states of the ED-SHG process due to a pulsed periodic drive (black curve). We assumed a Gaussian envelope of width 120 fs, a peak driving field $E_{max}^{pu} = 10^9$ V/m, and polarization $\theta = 90°$. Inset shows the higher Floquet sectors (dashed lines) that hybridize with the states in the zeroth Floquet sector (solid lines). **b,** Predicted maximum energy shift versus peak driving field calculated using our full Floquet formalism (Floquet), optical Stark shift (OS), Bloch-Siegert shift (BS), and the sum of OS and BS. Inset shows a calculation of the corresponding change in the magnetic contribution to the SHG intensity (defined in Figure 4.3d).

truncated at the $\pm 3^{rd}$ Floquet sector (Figure 4.4a inset), we obtain the pump field dressed initial and final states $|i'\rangle$ and $|f'\rangle$

$$
\begin{aligned}
|i'\rangle &= e^{-i(E_i - \Delta E)t/\hbar}(\cos\alpha\,|i\rangle + \sin\alpha\,e^{i\phi(t)}|f\rangle) \\
|f'\rangle &= e^{-i(E_f + \Delta E)t/\hbar}(-\sin\alpha\,e^{-i\phi(t)}|i\rangle + \cos\alpha\,|f\rangle),
\end{aligned}
\tag{4.10}
$$

where ΔE is the energy shift and the hybridization is parameterized by a mixing amplitude $\sin\alpha$ and phase $\phi(t)$, which all depend on $\vec{E}^{pu}$. For a Gaussian-pulsed drive, our calculations show that in the adiabatic limit where the pulse width far exceeds Ω^{-1}, both the bandgap and hybridization undergo a temporal increase that follows the pulse envelope (Figure 4.4a), attaining maximum values at the peak pump field E_{max}^{pu}. The maximal mixing amplitude scales linearly with E_{max}^{pu} as expected from a perturbative treatment, whereas the maximal bandgap increase $(2\Delta E)$ scales like the square of E_{max}^{pu}. While this quadratic dependence is reminiscent of the optical Stark effect (Autler and Townes, 1955; Sie, McIver, et al., 2015), our Floquet treatment goes beyond the rotating wave approximation by including both optical Stark and Bloch-Siegert shifts (Bloch and Siegert, 1940) (Figure 4.4b) as

well as the influence of higher Floquet sectors, predicting $2\Delta E_{max}$ as large as 188 meV for $E_{max}^{pu} = 10^9$ V/m.
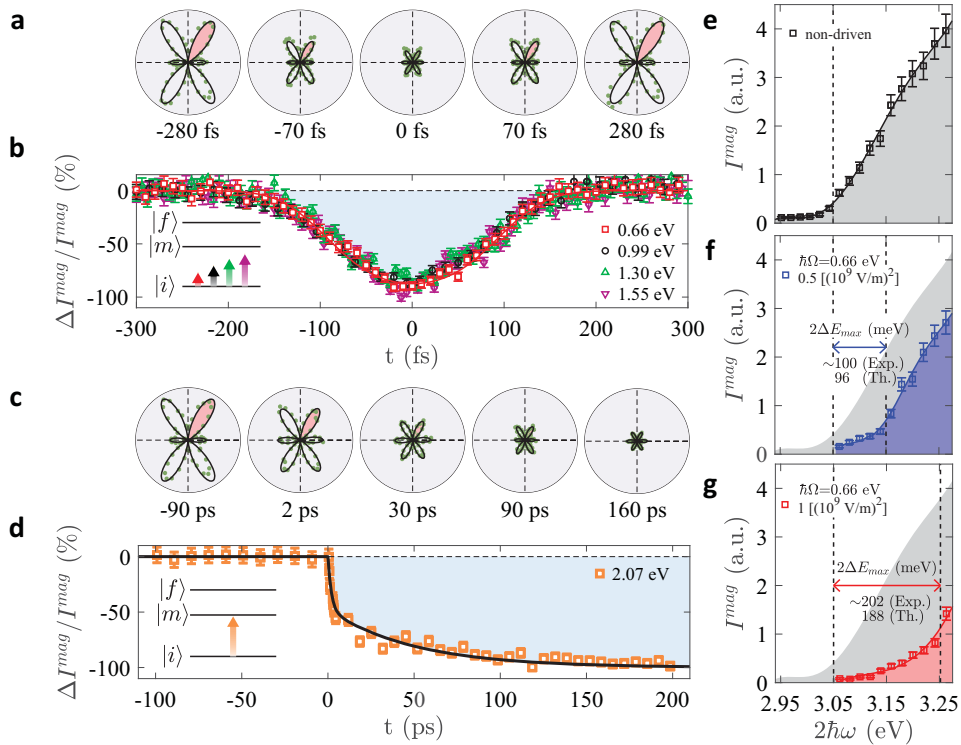

Figure 4.5: Driving photon energy dependence of RA-SHG transients. **a,** Time-resolved RA-SHG patterns from $MnPS_3$ measured at 10 K following a pulsed sub-gap drive with $\hbar\Omega = 0.66$ eV and $E_{max}^{pu} = 10^9$ V/m (green circles). Black curves are fits to our Floquet model. **b,** $\Delta I^{mag}/I^{mag}$ transients measured at $\varphi = 60°$ (pink lobes in panel **a**) for different sub-gap pump photon energies (inset) and E_{max}^{pu} fixed at 10^9 V/m. The red curve shows the theoretically predicted SHG response for 0.66 eV drive convolved with the probe pulse profile. Pump-induced changes in the linear optical response or competing second-order nonlinear processes can be excluded as the cause of SHG suppression. **c,** Time-resolved RA-SHG patterns measured under resonant pumping ($\hbar\Omega = 2.07$ eV) conditions (inset) with E_{max}^{pu} set to 7.5×10^8 V/m (green circles). Fits to the static RA patterns (Fig. 1d) at temperatures 10 K, 64 K, 76 K, 77 K and 80 K (left to right) are overlaid for comparison. **d,** Corresponding $\Delta I^{mag}/I^{mag}$ transient for resonant pumping conditions. Black curve is a guide to the eye. **e,** Non-driven SHG spectrum at 10 K. **f** and **g,** Transient $t = 0$ SHG spectra at two different E_{max}^{pu} values. Solid curves in panels **e**–**g** are guides to the eye. Vertical dashed lines mark the intensity upturns. Values of the observed and theoretically calculated energy shifts are indicated. All error bars represent the standard errors of the mean from four independent measurements.

Both mixing and bandgap widening, imparted by a coherent modulation of the two-level Hamiltonian comprised of $|i\rangle$ and $|f\rangle$, should suppress the magnitude of $\chi_{ijk}^{ED(c)}$

because the former reduces the amplitude of states in the zeroth Floquet sector—the dominant contribution to $\chi_{ijk}^{\mathrm{ED(c)}}$—by a factor of $\cos\alpha$, while the latter shifts the resonance condition away from $\hbar\omega = 1.55$ eV. The fast oscillating pump field induces a quasi-static change in the time-averaged value of $\chi_{ijk}^{\mathrm{ED(c)}}$ that follows the slower pump pulse envelope, consistent with a Floquet description. To quantify these effects, we computed the expected change in $\chi_{ijk}^{\mathrm{ED(c)}}$ and the resulting modulation of the magnetic contribution to the SHG intensity I^{mag} (Fig. 4.3d) within our single ion model using the dressed initial and final states, assuming $\hbar\Omega$ well below the $^6A_{1g} \rightarrow$ $^4T_{1g}$ transition and $\vec{E}^{\mathrm{pu}}$ parallel to the nearest neighbor Mn-Mn bond ($\theta = 90°$). As shown in the inset of Figure 4.4b, we predict an inverse power law-like dependence of I^{mag} on the driving field amplitude, indicating that the suppression is predominantly caused by energy shifts that affect the denominator in Equation 4.7. Remarkably, we predict that Floquet engineering can impart a giant suppression exceeding 90% at readily attainable field strengths of order 10^9 V/m.

Giant SHG modulation

To experimentally test our prediction, we performed time-resolved pump-probe RA-SHG measurements in the AFM phase of MnPS$_3$. To minimize dissipation and decoherence, the pump photon energy was tuned below the $^6A_{1g} \rightarrow {}^4T_{1g}$ transition edge near 2 eV to avoid absorption, but above 0.5 eV to suppress the effects of quantum tunneling between valence and conduction bands, phonon resonances, and photo-assisted inter-site hopping that are more pronounced at lower frequencies. Gaussian pump and probe pulse envelopes of 120 fs and 80 fs duration were used respectively, satisfying the adiabatic condition. Figure 4.5a shows instantaneous RA patterns at select time delays measured using $\theta = 90°$ and $E_{\mathrm{max}}^{\mathrm{pu}} = 10^9$ V/m. The magnitude of the RA patterns is drastically reduced during pumping and can be fit by simply decreasing all $\chi_{ijk}^{\mathrm{ED(c)}}$ elements uniformly. The temporal evolution of the RA patterns is completely symmetric about time $t = 0$ – the instant when pump and probe pulses are exactly overlapped—and the transient SHG intensity change $\Delta I^{\mathrm{mag}}/I^{\mathrm{mag}}$ exhibits a temporal profile that matches the theoretically predicted SHG profile convolved with the probe pulse (Figure 4.5b). These data indicate a coherent and uniform modulation of the $2'/m$ magnetic point group allowed $\chi_{ijk}^{\mathrm{ED(c)}}$ elements with no measurable dissipation, in accordance with a Floquet engineering process. The maximal suppression of I^{mag} reaches around 90% and is unchanged upon sweeping $\hbar\Omega$ from 0.66 eV to 1.55 eV, in full agreement with our theoretical model.
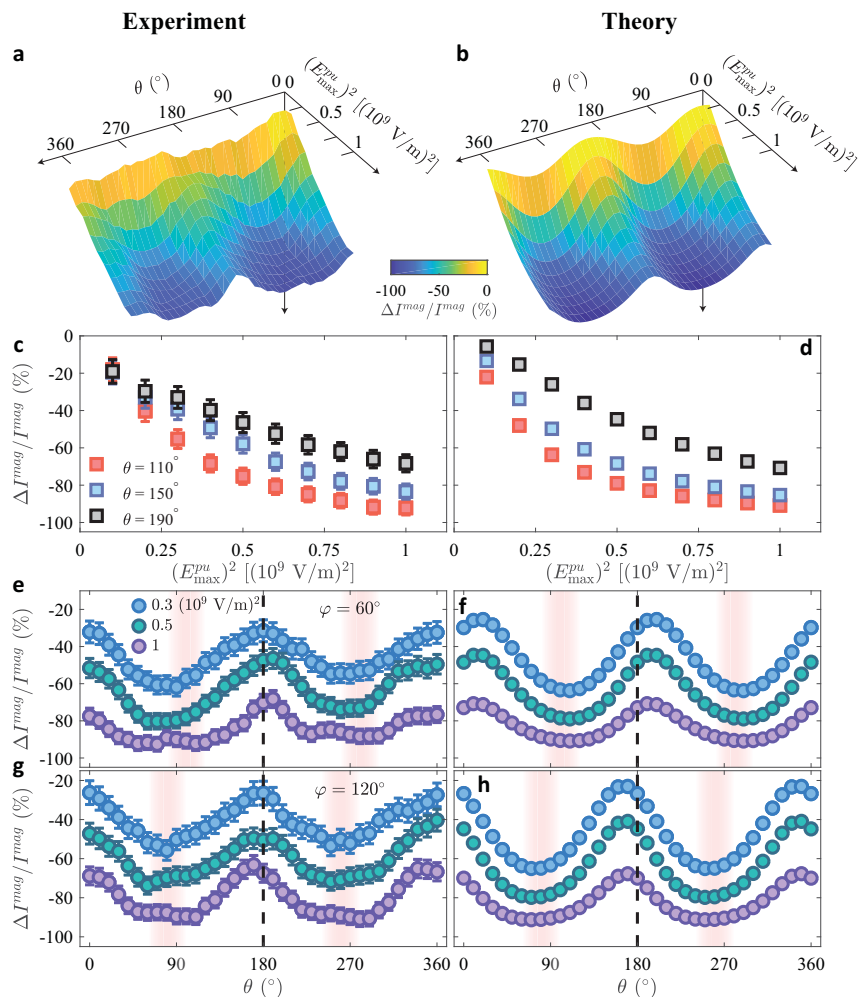
Figure 4.6: Driving field amplitude and polarization dependence of SHG modulation. Experimentally measured (left column) and theoretically predicted (right column) value of $\Delta I^{\mathrm{mag}}/I^{\mathrm{mag}}$ at time zero as a function of the peak driving field and polarization. **a,b** show the full two-dimensional maps. **c,d** show one-dimensional cuts along the field axis at selected θ values. **e,f** show one-dimensional cuts along the θ axis at selected field strengths for $\varphi = 60°$ and **g,h** $\varphi = 120°$. The positions marked by the faint vertical red bars indicate where the largest $\Delta I^{\mathrm{mag}}/I^{\mathrm{mag}}$ is predicted. The slight horizontal offset between the $\varphi = 60°$ and $\varphi = 120°$ curves arises due to a degeneracy of the final state, not Rabi frequency anisotropy. All error bars represent the standard errors of the mean from four independent measurements.

Heating as a contrast

In contrast, measurements performed with $\hbar\Omega$ tuned near the ${}^6A_{1g} \to {}^4T_{1g}$ absorption peak reveal dynamics that are strongly asymmetric about $t = 0$. Following an initial fast coherent reduction of I^{mag}, there is a slow exponential decay to 100% suppression, where it remains for more than 500 ps (Figure 4.5d). The decay and

plateau are consistent with an incoherent quasi-thermal melting of the AFM order via heat transfer from the optically excited electronic subsystem to the spin subsystem, followed by a very slow cooling of the pumped region through diffusion. This interpretation is further corroborated by instantaneous RA data acquired within the exponential decay time window, which directly map onto our temperature-dependent RA data (Figure 4.5c).

Transient SHG spectrum measurements

To directly confirm the predicted bandgap widening effect (Figure 4.4), we performed transient SHG spectroscopy measurements with $\hbar\Omega = 0.66$ eV. The equilibrium SHG spectrum exhibits a steep intensity upturn near the band edge of $MnPS_3$ at $2\hbar\omega = 3.05$ eV (Figure 4.5e), in accordance with the optical absorption spectrum (Piryatinskaya et al., 2012) as expected. Upon driving, the band edge feature instantaneously shifts to higher energy, which is opposite to the typical response of electronic gaps to photo-excitation. The size of the positive shift at $t = 0$ increases monotonically with E_{max}^{pu} and agrees reasonably well with our theoretically predicted values (Figure 4.5f & g), further supporting the Floquet engineering interpretation.

Driving field and polarization dependence

Since both the bandgap widening and level mixing are dependent on the Rabi frequency $\langle f | e\vec{r} \cdot \vec{E}^{pu} / \hbar | i \rangle$, we expect the magnitude of SHG modulation to be tunable by both the electric field amplitude and polarization of the pump pulse. To study this relationship, we performed a comprehensive experimental mapping of $\Delta I^{mag} / I^{mag}(t = 0)$ as a function of both E_{max}^{pu} and θ using $\hbar\Omega = 0.66$ eV (Figure 4.6a). A comparison to our model calculation performed over the same parameter space (Figure 4.6b), using the same weighting of dipole matrix elements along x and y as in our static model to account for inter-layer coupling, shows excellent agreement in overall trend. More detailed comparisons can be drawn by taking different one-dimensional cuts through our data set. For a fixed θ, $\Delta I^{mag} / I^{mag}$ exhibits an expected inverse power law-like dependence on pump field in both experiment and theory (Figure 4.6c and 4.6d), with good agreement on the level of suppression. For a fixed pump field, we observe a sinusoidal dependence of $\Delta I^{mag} / I^{mag}$ on θ that is reproduced in our calculations (Figure 4.6e and 4.6f). Although the three-fold rotational symmetry of an isolated honeycomb layer forbids an anisotropic Rabi frequency, this is broken in bulk $MnPS_3$ due to the layer stacking (inset Figure 4.3d), resulting in a maximum (minimum) Rabi frequency at $\theta = 90°$ ($0°$). The

fact that the θ dependence remains largely unchanged upon rotating ϕ (Figure 4.6g and 4.6h) confirms that the anisotropy is intrinsic to the crystal and is unrelated to the relative polarization of the pump and probe light. The close agreement between our measurements and theoretical calculations, which contain no free parameters, confirms the validity of our single-ion treatment and highlights its dominant role over photo-assisted inter-site hopping effects in our experiments.

Outlooks

The Floquet engineering strategy demonstrated here can be broadly applied to coherently control a variety of nonlinear optical processes including optical rectification and higher harmonic generation. Moreover, both coherent enhancement and suppression of the nonlinear response can in principle be realized by tuning the probe photon energy to either side of an absorption resonance. Introducing few-layer exfoliable materials like $MnPS_3$ into cavity architectures (Sentef et al., 2020) raises the exciting prospect of coherently switchable optical, optoelectronic, and magnetic devices with reduced external field thresholds. During my PhD I also used time-resolved SHG to study a closely related compound, $NiPS_3$.

Chapter 5

NONTHERMAL OPTICAL ENGINEERING OF MAGNETIC PROPERTIES

5.1 Floquet revisited: Dynamical localization and exchange renormalization Theories

We have introduced the Floquet formalism in Chapter 4.1. In Chapter 4.2, we demonstrated that how the Floquet mechanism can be used to modulate the electrical and optical properties of materials. Here we summarize some theoretical progress on Floquet engineering magnetism in quantum materials.

We start from the Hubbard model for strongly correlated materials,

$$H = -t_0 \sum_{\langle ij \rangle \sigma} c_{i\sigma}^\dagger c_{j\sigma} + U \sum_j n_{j\uparrow} n_{j\downarrow}, \tag{5.1}$$

where t_0 is the hopping parameter and U is the onsite Coulomb repulsion energy. If $U \gg t_0$, the system is a Mott insulator and each lattice site is occupied by exactly one electron (in the half-filling case). We then focus on the interaction between the spins of these electrons. Starting from the U term and treating the t_0 term as a perturbation, we can reach a low-energy effective Heisenberg Hamiltonian

$$H_{\rm H} = J \sum_{\langle ij \rangle} \mathbf{S}_i \cdot \mathbf{S}_j, \tag{5.2}$$

where $J = 4t_0^2/U$. This Hamiltonian determines the magnetic structure of a material, as in real materials J can be either positive or negative. Consider a square lattice with no frustration. When $J < 0$, parallel spins yield the smallest energy so the ground state is ferromagnetic. When $J > 0$, anti-parallel spins yield smaller energy so the ground state is approximately antiferromagnetic (not exactly anti-parallel spins due to the zero point energy).

In cases of honeycomb lattices, the exact spin configuration is determined by the ratio between nearest neighbor, next-nearest neighbor, and next-next-nearest neighbor spin exchange couplings. By tuning their relative strengths, the spins can show either a ferromagnetic configuration, or a Néel-, zigzag-, or stripy-type antiferromagnetic configuration (Sivadas et al., 2015).

Now consider just one band (the lower Hubbard band). Under an oscillating electric field, in the high-frequency limit it has been shown that the hopping integral t_0 can be renormalized (Dunlap and Kenkre, 1986) by a factor of $J_0(\mathcal{E})$, where J_0 is the zeroth-order Bessel function and $\mathcal{E} \equiv \frac{eaE}{\hbar\Omega}$ is the Floquet parameter, where e is the electron charge, a is the atomic spacing, E is the electric field, and Ω is the driving frequency. When the combination of E and ω reaches a certain value such that $\mathcal{E}$ is a root of J_0, the effective t_0 reaches 0 and the dynamical localization is realized.

This has ramifications on the exchange J since J is proportional to t_0^2. Therefore, J will be renormalized by $J_0(\mathcal{E})^2$. This is a simplified view if $\Omega \gg U$ and we call this contribution the photo-assisted tunneling. In realistic cases, we also need to consider the virtual excitations between different Floquet sectors of the lower and upper Hubbard bands, and the full expression of the renormalized J is (Mentink, Balzer, and Eckstein, 2015)

$$\frac{J_{\text{eff}}}{J} = \sum_{n=-\infty}^{\infty} \frac{J_{|n|}(\mathcal{E})^2}{1 + n\Omega/U}. \tag{5.3}$$

This renormalization factor can be positive, negative, or zero. Although this Floquet renormalization of J has not been realized in condensed matter systems so far, cold atoms have provided an ideal platform to realize this principle, as a large inter-atomic spacing a reduces the need for a large driving amplitude. Both the enhancement and sign reversal of J has been realized in cold atom systems (Görg et al., 2018), where a piezoelectric actuator sinusoidally drives the system.

Applications to MnPS$_3$

The exchange interaction in realistic materials, like MnPS$_3$, is not through direct hopping but through exchange interactions mediated by ligand ions. This can make the Flouqet renormalization calculations more complicated (Chaudhary, Ron, et al., 2020). Though the exact values might differ, the physics is similar to the direct hopping case—keeping the driving frequency fixed, increasing field strengths first enhance J, then suppressing it and inducing a sign reversal of J.

For our Floquet experiments described in Chapter 4.2, the Floquet parameter $\mathcal{E}$ with our largest fluence used is on the order of 0.7. This is not quite enough for generating a significant renormalization of J (Chaudhary, Ron, et al., 2020). We anticipate that even if we manage to manage to renormalize J by a marked amount, we still cannot drive MnPS$_3$ to a different magnetic phase with our $\sim$ 100 fs pulses, since the J in this material corresponds to a time scale of $\sim$ 5 ps (Kurosawa, Saito,

and Yamaguchi, 1983), and this is the time scale required for a quasi-static magnetic phase to emerge.
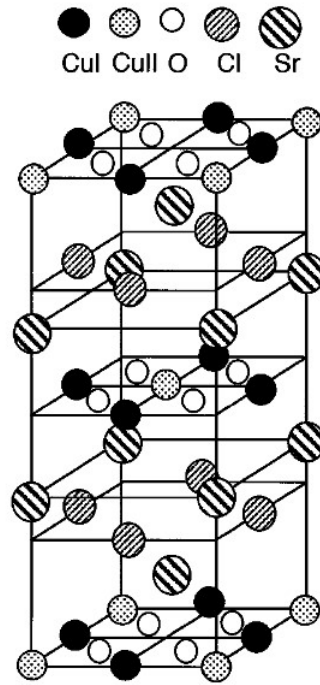

Figure 5.1: The crystal structure of $Sr_2Cu_3O_4Cl_2$. Taken from Chou et al., 1997.

5.2   Magnon bath engineering of $Sr_2Cu_3O_4Cl_2$

Introduction

Controlling the magnetic order of quantum materials holds the prospects of both elucidating the nature of strongly correlated electrons and making better memory devices. Light can induce transient demagnetization at ultrafast speeds (Beaurepaire et al., 1996; Kirilyuk, Kimel, and Rasing, 2010). Though in the electric dipole approximation photons cannot directly induce spin flips, recently strategies have emerged to resonantly induce magnons with infrared or terahertz optical pulses (Kampfrath et al., 2011; Mashkovich et al., 2021). However, no demagnetization has been realized via resonant magnon driving. Here we demonstrate complete melting of the antiferromagnetic order in the parent compound cuprate $Sr_2Cu_3O_4Cl_2$ without inducing charge excitations. By driving far off-resonance from the charge transfer transition and resonant with the sum of two zone-boundary magnon frequencies, we observe an ultrafast full suppression of the magnetism-induced second harmonic generation. We further demonstrated a peaked demagnetization efficiency when we brought the driving frequency to twice the van Hove singularity of the magnon spec-
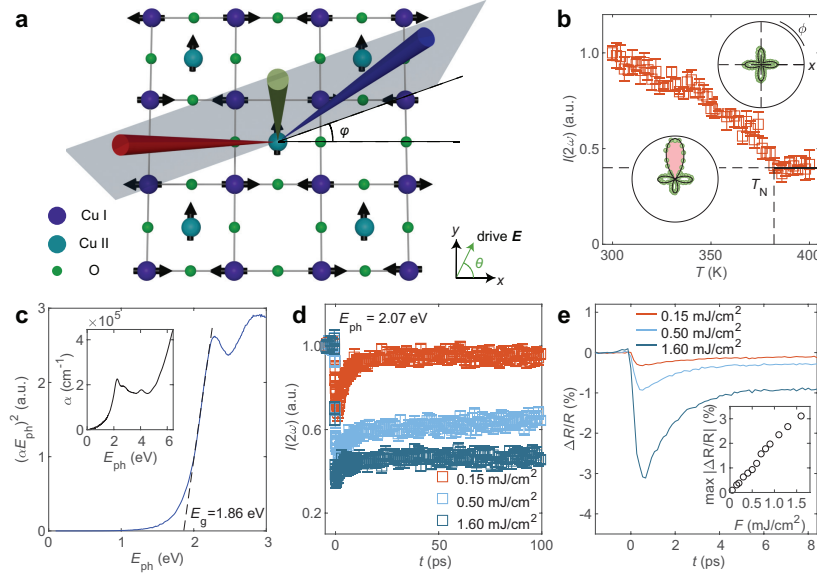
Figure 5.2: Photo-doping of $Sr_2Cu_3O_4Cl_2$. **a,** Depiction of the experimental geometry and the spin arrangement on the two copper sublattices in the Cu_3O_4 plane at room temperature. The probe beam (red) is focused obliquely onto the sample, and the reflected SHG beam (blue) is measured as a function of the scattering plane angle φ. Both incident and reflected beams are linearly polarized in the scattering plane. The driving beam (green) is focused normally onto the sample with linear polarization along θ. **b,** Temperature-dependent SHG intensity acquired at $\varphi = 90°$ (pink lobe in inset) normalized by its value at 300 K. Insets show RA-SHG patterns above and below T_N (green circles) and fits to the superposition between an EQ term and an MD term. **c,** The inset shows the absorption spectrum of $Sr_2Cu_3O_4Cl_2$ (blue curve) in a broad range. To facilitate the linear fitting of E_g we plot the $(\alpha E_{ph})^2$ versus E_{ph}. **d,** Time-resolved SHG intensity at $\varphi = 90°$ at selected fluences (smaller than the critical fluence inducing a complete demagnetization, the critical fluence, and the fluence where the recovery dynamics becomes infinitely slow). **e,** The transient reflectivity $\Delta R/R$ at corresponding fluences. The inset shows the linear relationship between the maximum $\Delta R/R$ and the fluence. All error bars represent the standard error of the mean from four independent measurements.

trum. The mechanism for the initial demagnetization is nonthermal, as evidenced by the two separate internal magnon relaxation processes for in-plane and out-of-plane momenta.

Antiferromagnets can make stabler memory devices due to their lack of magnetic moments, but the ultrafast control of the antiferromagnetic orders have always involved charge excitations, either thermal (Beaurepaire et al., 1996) or nonthermal (Kimel et al., 2005), which can pose serious heating problems. To avoid heating, we need sub-gap direct resonant coupling between photons and magnons, but it is

forbidden by the selection rules within the electric dipole channel. Previous works have got around this by leveraging the magnetic dipole interactions (Kampfrath et al., 2011; Mashkovich et al., 2021) or involving the spin-orbit coupling (Seifert and Balents, 2019). Due to their low efficiencies, earlier works have only demonstrated perturbations to the antiferromagnetic background. It is unsettled whether one can fully melt the antiferromagetic order with light frequencies resonant with magnons.
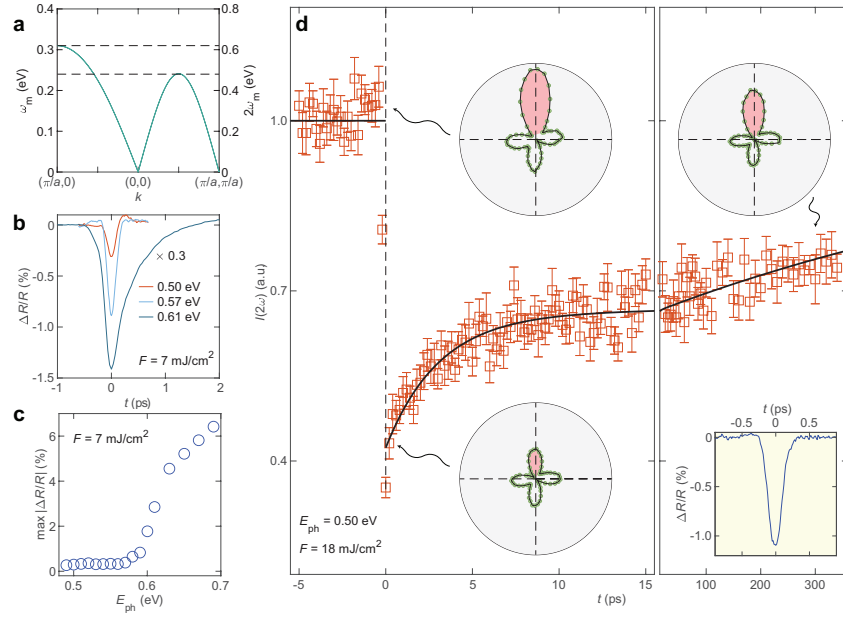

Figure 5.3: Complete demagnetization induced by directly-pumped magnons. **a,** The magnon dispersion of the copper I spins, adapted from Guarise et al., 2010. Horizontal dashed lines represent singularities in the magnon density of states. The k_x and k_y axes are defined to coincide with the x and y directions in Figure 5.2a and a is the atomic spacing between nearest-neighbor copper I atoms. Here we omit the $k_z = 0$ component for simplicity. **b,** The transient reflectivity $\Delta R/R$ traces for selected pump photon energies at a fixed pump fluence of 7 mJ/cm^2. **c,** The maximum amplitude of the $\Delta R/R$ traces as a function of pump photon energies. **d,** The time-resolved SHG intensity (red squares) and a double-exponential fit (black curve) at short and long time delays. Three insets show the full RA patterns at selected time delays (before $t = 0$, right after $t = 0$, and at $t = 300$ ps). The inset also shows the $\Delta R/R$ trace taken simultaneously with the time-resolved SHG data in the main panel. All error bars represent the standard error of the mean from 15 independent measurements.

The key issue lies in the magnon density of states at the energy of the pump photons. There are regions in the magnon spectrum where it is dispersionless, and the magnon density of states diverges theoretically, which is the van Hove singularity (Bassani and Pastori Parravicini, 1975). Since photons carry near-zero momentum, energy

and momentum conservation laws dictate that two zone-boundary magnons with identical energy but opposite momentum have to be generated simultaneously. As a result, if we optically pump the antiferromagnet at twice the van Hove singularity frequency, we expect to observe an enhanced efficiency of demagnetization due to the large number of magnons generated.

In this regard, the parent compound cuprate $Sr_2Cu_3O_4Cl_2$ (Figure 5.1) is an ideal demonstration platform for the following reasons. First, $Sr_2Cu_3O_4Cl_2$ has two sets of copper atoms in the Cu_3O_4 plane (Figure 5.2a). Below the Néel temperature of the copper I spins, an effective field is generated at the copper II sites through pseudo-dipolar interactions, inducing a paramagnetic alignment of the copper II spins (Chou et al., 1997). This spin configuration enables an enhanced second harmonic generation intensity which linearly couples to the antiferromagnetic order parameter of copper I, serving as an easy optical indicator of the centrosymmetric spin order which is generally not easy to detect. Second, the high Néel temperature $T_{N,I}$ of 380 K allows experiments at both room temperature and cryogenic temperatures, facilitating its potential applications. Lastly, the van Hove singularity of its magnon spectrum is at around 0.3 eV (Guarise et al., 2010), allowing an easy near-infrared pumping scheme at around 0.6 eV. The large separation between twice the van Hove singularity energy and the charge transfer gap energy ($\sim$ 1.8 eV) also prevents runaway heating.

SHG as a means to detect centrosymmetric antiferromagnetic order

In addition to the i-type second harmonic generation from the lattice, the AFM-induced alignment of the copper II spins yields a c-type (time-reversal odd) second harmonic generation (Fiebig, Pavlov, and Pisarev, 2005) in the magnetic dipole channel, describe by the equation, $P_i(2\omega) = \chi^{MD}_{ijk}E_j(\omega)H_k(\omega)$, where the induced polarization P at twice the incident frequency ω is linked to the incident electric field E and magnetic field H via the susceptibility tensor χ^{MD}, and the indices run over the x, y, and z coordinates (Boyd, 2020). We measured the temperature-dependent SHG rotational anisotropy, where we measure the SHG reflection from an obliquely incident light as a function of the scattering plane angle φ (Figure 5.2a) (Harter et al., 2015). Under $T_{N,I}$ the symmetry of the RA pattern changes from C_4 to C_1, and the intensity at $\varphi = 90°$ undergoes a steep upturn (Figure 5.2b).

To determine the bandgap E_g and the transparency window of $Sr_2Cu_3O_4Cl_2$, we measured its absorption spectrum at room temperature (Figure 5.2c inset). We

fit our data near 2 eV to a general model for the interband absorption coefficient α due to direct allowed transitions in three-dimensional semiconductors $\alpha(E) = (A/E)\sqrt{E - E_g}\Theta(E - E_g)$, where A is a constant, E is photon energy and Θ is the Heaviside function (Figure 5.2c) (Ukhanov, 1977; Shan, Ye, et al., 2021). A best fit yields E_g =1.86 eV, which is similar to the band gap of its sister compound $Sr_2CuO_2Cl_2$, which does not contain the copper II atoms (Choi et al., 1999).

Suppression of AFM order by photodoping

We first confirm that we can use the time-resolved SHG to track the antiferomagnetism order dynamics within a more common photo-doping case. We used a 2-eV near-normal incidence pump light, which is above the charge transfer gap, and monitored both the charge dynamics using the transient linear reflectivity $\Delta R/R$ and the spin dynamics using the time-resolved SHG $I(2\omega)$ at $\varphi = 90°$. The non-saturating $\Delta R/R$ with an increasing fluence shows an exponential decay after $t = 0$ - the instant when the pump and probe pulses overlap, corresponding to the relaxation of excited doublons (Figure 5.2e). The SHG, on the other hand, gets fully suppressed to the paramagnetic value at a fluence of 0.5 mJ/cm^2, indicating a full suppression of the antiferromagnetic order (Figure 5.2d). If we increase the fluence further, the maximum magnitude of the SHG suppression does not grow, but the relaxing process becomes slower, hinting at a non-thermal demagnetization where the internal thermalization of the magnons dominates the recovery process (de la Torre et al., 2022).

The charge dynamics

We then search for the frequency window of the pump light which is resonant with twice the van Hove singularity but far from the charge transfer gap. The dispersion of the magnons in $Sr_2Cu_3O_4Cl_2$ is much larger in the xy plane than along z, since the out-of-plane superexchange energy is four orders of magnitude smaller than the in-plane superexchange energy (Y. J. Kim et al., 2001). We also approximate the magnon dispersion of $Sr_2Cu_3O_4Cl_2$ with the magnon dispersion of $Sr_2CuO_2Cl_2$ measured through inelastic X-ray scattering in a previous report (Figure 5.3a) as the coupling between the copper I and copper II spins is weak (Guarise et al., 2010), which yields similar dispersion to another Cu_3O_4 compound, $Ba_2Cu_3O_4Cl_2$ (Babkevich et al., 2017). We expect large magnon density of states around 0.2 ~ 0.3 eV due to the flat dispersion of the spectrum at these energies.

To confirm that we do not excite charges if we pump at twice these energies, we

track the $\Delta R/R$ dynamics with sub-gap pump photon energies (Figure 5.3b). While below 0.6 eV pumping the curves show fully coherent Gaussian behavior, indicating the absence of charge excitations, at higher pump photon energies (e.g., 0.61 eV) the curve goes back to an exponential decaying shape as in the case of 2 eV pump (Figure 5.2e). We also measured the maximum magnitude of $\Delta R/R$ as a function of the pump photon energy (Figure 5.3c), where we clearly observed an onset at $E_g/3$, indicating multi-photon absorption as the main mechanism of the charge excitation for pump photon energies above 0.6 eV.

Full suppression of AFM via sub-gap driving

As a demonstration of the principle, we measured the time resolved SHG RA patterns with 0.50 eV pump, where multi-photon absorption is negligible (Figure 5.3d). When $t < 0$ the pattern is the same as the static one. Immediately after the pump pulse ends ($t = 400$ fs) the pattern restores the C_4 rotational symmetry, indicating a complete suppression of the antiferromgnetic order. The $\Delta R/R$ has returned to zero at $t = 400$ fs, so the demagnetization is solely due to the excitation of zone-boundary magnons. The double exponential relaxation of the SHG intensity (black fitting curve of Figure 5.3d) corresponds to the thermal equilibration process of the magnons between in-plane and out-of-plane momenta, which we will discuss in detail below, so the full demagnetization immediately after $t = 0$ is caused by a non-thermal distribution of magnons.

In order to study the origin of this enhanced magnon generation efficiency compared to previous studies, we performed time-resolved SHG measurements at a wide range of pump photon energies to track the demagnetization efficiency (Figure 5.4a). We chose a smaller fluence of 7 mJ/cm^2 where only partial demagnetization occurs so we can use the SHG intensity at $t = 400$ fs to indicate the demagnetization efficiency. We observed a peaked efficiency at $E_{ph} = 0.55$ eV and decreasing efficiencies on both sides, which is intrinsic to this material. This trend further excludes charge excitation as the origin of the demagnetization as in the $E_{ph} = 2.07$ eV case, as there are no absorption peaks in the sub-eV range, and any multi-photon absorption should not exhibit this peaking behavior. As the lattice excitation is of lower energies (Zibold et al., 1996), we conclude that the enhanced demagnetization efficiency is a result of larger density of states of the magnons resonant with half of the pump frequency, due to the van Hove singularities in the magnon spectrum.

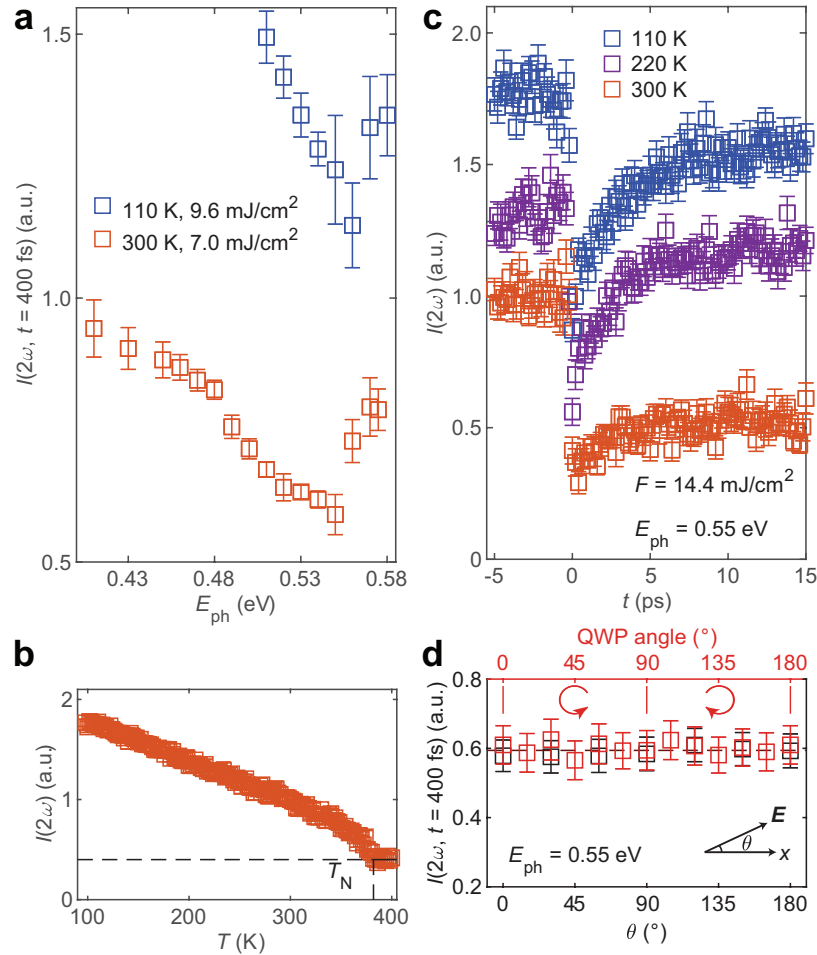We can further corroborate this scenario by measuring time-resolved SHG measure-

Figure 5.4: Mechanism of the demagnetization. **a,** Time-resolved SHG intensity for $\varphi = 90°$ from $Sr_2Cu_3O_4Cl_2$ measured at 110 K and 300 K immediately after the sub-gap pump pulse ($t = 400$ fs), as a function of the pump photon energy. **b,** The temperature-dependent SHG intensity from 100 K to 400 K. **c,** Time-resolved SHG intensity for $\varphi = 90°$ measured at different temperatures, with a pump photon energy of 0.55 eV. **d,** The linear and circular pump polarization dependence of the SHG measured immediately after the sub-gap pump pulse.

ments with different pump frequencies at a lower temperature, 110 K, where the magnons are expected to harden. At lower temperatures the time-resolved SHG at $t = 400$ fs drops to higher intensities, indicating that it is more difficult to suppress the magnetic order since the order parameter is more robust in equilibrium (Figure 5.4b and c). At 110 K the maximum demagnetization efficiency occurs at 0.56 eV, which is slightly higher than the value at room temperature, consistent with the hardening of magnon frequencies at lower temperatures due to the stronger anti-ferromagnetic order parameter. Pump polarization-dependent studies (Figure 5.4d)

show no observable modifications of the demagnetization efficiency when varying the linear polarization or using a circular polarization.
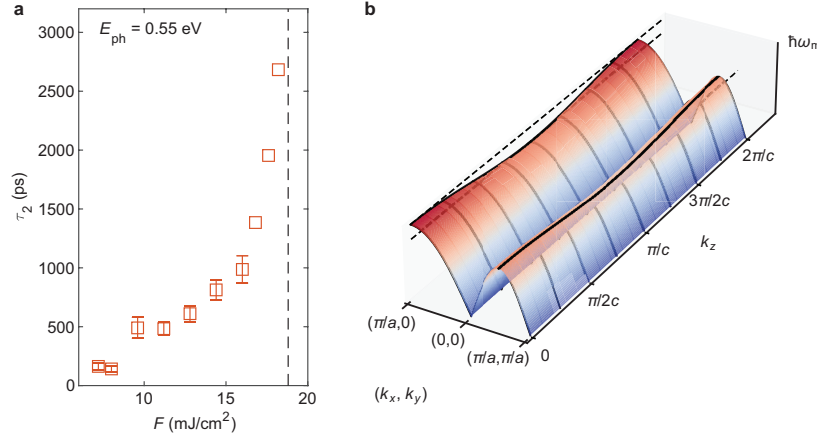

Figure 5.5: The thermalization of directly-pumped magnons. **a,** The recovery time constant τ_2 of the time-resolved SHG intensity at a pump photon energy of 0.55 eV, as a function of the pump fluence. The vertical dashed line indicates the fluence where tau_2 diverges. **b,** A schematic of the in-plane and out-of-plane magnon dispersion. The variation along k_z is exaggerated for clarity.

We note that the magnon density of states at half of the pump photon energy comes into play as a result of the Fermi's golden rule, where the transition rate Γ is given by

$$\Gamma = \frac{2\pi}{\hbar}|\langle f|H'|i\rangle|^2\rho(E_{\mathrm{ph}}),\qquad(5.4)$$

where i and f represent the ground state and the magnon state, $E_f - E_i = E_{\mathrm{ph}}$, H' is the light-spin coupling Hamiltonian, and ρ represents the two-magnon density of states. This term should exhibit a peak close to twice the van Hove singularity energy where the magnon density of states peaks.

In order to elucidate whether the demagnetization is caused by a thermalized magnon bath with a higher temperature, or a non-thermal magnon distribution, we set out to study the relaxation dynamics of the AFM order. The time-resolved SHG intensity after $t = 0$ can be fitted to a sum of two exponential decays, $I(2\omega, t) = 1 - a_1 \exp(-t/\tau_1) - a_2 \exp(-t/\tau_2)$ (see Figure 5.3d). In Figure 5.5a we plot the pump fluence dependence of τ_2 at $E_{\mathrm{ph}} = 0.57$ eV. Similar to the 2-eV pump case, we observed a divergence of τ_2 at around $F = 19$ mJ/cm^2. We conclude that the recovery dynamics is dominated by the internal thermalization between magnons

and the initial demagnetization is not due to higher-temperature thermal magnons (de la Torre et al., 2022). The two time scales, τ_1 and τ_2, correspond to the internal magnon thermalization between in-plane (k_x and k_y) and out-of-plane (k_z) momenta. Since the out-of-plane exchange energy is much smaller than the in-plane exchange energy, the magnon dispersion along k_z is negligible (Figure 5.5b). As a result, the phase space for the magnon thermalization along k_z is extremely limited, explaining why τ_2 is much larger than τ_1.

Chapter 6

CLOSING REMARKS

As we show in previous chapters, the interaction between light and matter is multifaceted. The magnetic field component of light can directly induce dynamics in the spin subsystem. The electric field component of light can induce collective lattice movements, charge excitations, and magnons, through either resonant or non-resonant pathways. Even if the frequency of light is not resonant with any energy scales in the quantum materials, their electronic, magnetic and optical properties can still be modified through Floquet engineering. The electric and magnetic field components can also interact nonlinearly inside the quantum materials.

The bounties offered by this versatility can become problematic if we want to make clear and clean claims about the exact mechanisms of observed optical engineering effects of quantum materials, as the quantum material properties are built on a delicate balance between the lattice, charge, orbit and spin degrees of freedom. Therefore, in our and future experiments, we have to choose wisely the parameters of the light and materials used, in order to single out the desired effects while suppressing the unwanted ones.

In our works, we chose insulators with large bandgaps to work with, in order to pump them subgap to avoid charge excitations and the subsequent thermal or non-thermal ramifications. In $MnPS_3$, we found a transparent window (below 1.5 eV, but above phonon or magnon energies) where light is not absorbed and thus a strong drive on the order of 10^9 V/m does not induce heating, In this transparent window, we demonstrated a giant modulation of the SHG efficiency and a significant widening of the bandgap. In $Sr_2Cu_3O_4Cl_2$, we pumped the material far below the charge transfer bandgap to avoid linear absorption and multi-photon absorption. As a result, we do not have to worry about the charge-induced demagnetization, which allowed us to showcase a complete demagnetization through direct photon-magnon coupling in the parent compound cuprate.

Prior to our works, it was generally believed that runaway heating is inevitable under strong driving conditions, dimming prospects for experimentally realizing Floquet engineering. Our novel strategy to achieve giant Floquet engineering effects without any measurable heating can be applied broadly to gapped materials and is

anticipated to accelerate progress in Floquet engineering research, particularly on the experimental front.

Also, our work shows that under strong driving conditions, electronic structure changes induced by single-ion effects can be very large and can dominate over inter-site effects. These effects can be accurately predicted in a materials specific way using Floquet theory calculations on single-ion models. Therefore, we anticipate our work to open new lines of investigation into the use of single-ion Floquet engineering to control the electronic and magnetic properties of targeted materials.

Light is powerful. It has so many degrees of freedom to play with. Its intensity and polarization can be easily controlled. Light carrying orbital angular momentum can be generated (Allen et al., 1992). Its temporal profile can be shaped to accommodate processes with different speeds. Its spatial profile can also be modulated to induce inhomogeneity. The marriage between materials and light has lasted decades, but we might have just explored a tiny fraction of the whole multi-dimensional phase space. With lots of existing theoretical predictions awaiting vindication, we will continue to be surprised by how much light can make new material properties, and how much light can help us understand the existing material properties.

Nowadays, when an engineer asks for a material to realize some function, they are asking a piece of *matter*. When the scientific research of optical engineering matures and enters practical applications, the definition of the term "material" might become very different, and it can mean a composite of *matter* and *light*. If in the future our alien friends from other planets ask us whether we have room-temperature superconductors, we might tell them, "Yes, but unfortunately these superconducting power transmission lines only work during daytime, because their functioning requires the photons from the sunlight!"

BIBLIOGRAPHY

Afanasiev, D. et al. (2019). "Ultrafast Spin Dynamics in Photodoped Spin-Orbit Mott Insulator Sr_2IrO_4". In: *Physical Review X* 9, p. 021020. DOI: 10.1103/PhysRevX.9.021020.

Allen, L. et al. (1992). "Orbital angular momentum of light and the transformation of Laguerre-Gaussian laser modes". In: *Physical Review A* 45, pp. 8185–8189. DOI: 10.1103/PhysRevA.45.8185.

An, Yong Q. et al. (2013). "Enhanced Optical Second-Harmonic Generation from the Current-Biased Graphene/SiO_2/Si(001) Structure". In: *Nano Letters* 13, pp. 2104–2109. DOI: 10.1021/nl4004514.

Anderson, P. W. and E. I. Blount (1965). "Symmetry Considerations on Martensitic Transformations: "Ferroelectric" Metals?" In: *Physical Review Letters* 14, pp. 217–219. DOI: 10.1103/PhysRevLett.14.217.

Armitage, N. P. (2018). "Electrodynamics of correlated electron systems". In: *arXiv:0908.1126 [cond-mat]*.

Aubry, S. (1975). "A unified approach to the interpretation of displacive and order–disorder systems. I. Thermodynamical aspect". In: *The Journal of Chemical Physics* 62, pp. 3217–3229. DOI: 10.1063/1.430872.

Autler, S. H. and C. H. Townes (1955). "Stark Effect in Rapidly Varying Fields". In: *Physical Review* 100, pp. 703–722. DOI: 10.1103/PhysRev.100.703.

Babkevich, P. et al. (2017). "Magnetic excitations from the two-dimensional interpenetrating Cu framework in $Ba_2Cu_3O_4Cl_2$". In: *Physical Review B* 96, p. 014410. DOI: 10.1103/PhysRevB.96.014410.

Barreto, F. C. Sá (2000). "Ferrroelectric phase transitions and the Ising model". In: *Brazilian Journal of Physics* 30, pp. 778–782. DOI: 10.1590/S0103-97332000000400027.

Basov, D. N., R. D. Averitt, and D. Hsieh (2017). "Towards properties on demand in quantum materials". In: *Nature Materials* 16, pp. 1077–1088. DOI: 10.1038/nmat5017.

Bassani, F. and G. Pastori Parravicini (1975). *Electronic states and optical transitions in solids*. Oxford: Pergamon Press. ISBN: 978-0-08-016846-3.

Bauer, Klaus-Dieter and Kurt Hingerl (2017). "Bulk quadrupole contribution to second harmonic generation from classical oscillator model in silicon". In: *Optics Express* 25, p. 26567. DOI: 10.1364/OE.25.026567.

Bayarjargal, Lkhamsuren and Björn Winkler (2013). "Pressure-Induced Magnetic Phase Transition in Cr_2O_3 Determined by Second Harmonic Generation Measurements". In: *Applied Physics Letters* 102, p. 182403. DOI: 10.1063/1.4804424.

Beaurepaire, E. et al. (1996). "Ultrafast Spin Dynamics in Ferromagnetic Nickel". In: *Physical Review Letters* 76, pp. 4250–4253. DOI: `10.1103/PhysRevLett.76.4250`.

Benedek, Nicole A. and Turan Birol (2016). "'Ferroelectric' metals reexamined: fundamental mechanisms and design considerations for new materials". In: *Journal of Materials Chemistry C* 4, pp. 4000–4015. DOI: `10.1039/C5TC03856A`.

Bloch, F. and A. Siegert (1940). "Magnetic Resonance for Nonrotating Fields". In: *Physical Review* 57, pp. 522–527. DOI: `10.1103/PhysRev.57.522`.

Bloembergen, N., R. K. Chang, et al. (1968). "Optical Second-Harmonic Generation in Reflection from Media with Inversion Symmetry". In: *Physical Review* 174, pp. 813–822. DOI: `10.1103/PhysRev.174.813`.

Bloembergen, N. and P. S. Pershan (1962). "Light Waves at the Boundary of Nonlinear Media". In: *Physical Review* 128, pp. 606–622. DOI: `10.1103/PhysRev.128.606`.

Boyd, Robert W. (2020). *Nonlinear Optics*. Cambridge: Academic Press.

Cao, Yuan et al. (2018). "Unconventional superconductivity in magic-angle graphene superlattices". In: *Nature* 556, pp. 43–50. DOI: `10.1038/nature26160`.

Chan, M. K. et al. (2016). "Single reconstructed Fermi surface pocket in an underdoped single-layer cuprate superconductor". In: *Nature Communications* 7, p. 12244. DOI: `10.1038/ncomms12244`.

Chaudhary, S., D. Hsieh, and Gil Refael (2019). "Orbital Floquet Engineering of Exchange Interactions in Magnetic Materials". In: *Physical Review B* 100, p. 220403. DOI: `10.1103/PhysRevB.100.220403`.

Chaudhary, S., A. Ron, et al. (2020). "Controlling ligand-mediated exchange interactions in periodically driven magnetic materials". In: *arXiv:2009.00813 [cond-mat]*.

Choi, H. S. et al. (1999). "Anomalous temperature dependence of charge-transfer excitation in the undoped cuprate $Sr_2CuO_2Cl_2$". In: *Physical Review B* 60, pp. 4646–4652. DOI: `10.1103/PhysRevB.60.4646`.

Chou, F. C. et al. (1997). "Ferromagnetic moment and spin rotation transitions in tetragonal antiferromagnetic $Sr_2Cu_3O_4Cl_2$". In: *Physical Review Letters* 78, pp. 535–538. DOI: `10.1103/PhysRevLett.78.535`.

Chu, Hao et al. (2020). "Linear Magnetoelectric Phase in Ultrathin $MnPS_3$ Probed by Optical Second Harmonic Generation". In: *Physical Review Letters* 124, p. 027601. DOI: `10.1103/PhysRevLett.124.027601`.

Claassen, Martin et al. (2017). "Dynamical Time-Reversal Symmetry Breaking and Photo-Induced Chiral Spin Liquids in Frustrated Mott Insulators". In: *Nature Communications* 8, p. 1192. DOI: `10.1038/s41467-017-00876-y`.

de la Torre, A. et al. (2022). "Decoupling of static and dynamic criticality in a driven Mott insulator". In: *Communications Physics* 5, pp. 1–8. DOI: `10.1038/s42005-022-00813-6`.

Disa, Ankit S. et al. (2020). "Polarizing an antiferromagnet by optical engineering of the crystal field". In: *Nature Physics* 16, pp. 937–941. DOI: `10.1038/s41567-020-0936-3`.

Dolino, G. (1972). "Effects of Domain Shapes on Second-Harmonic Scattering in Triglycine Sulfate". In: *Physical Review B* 6, pp. 4025–4035. DOI: `10.1103/PhysRevB.6.4025`.

Drozdov, A. P. et al. (2015). "Conventional superconductivity at 203 kelvin at high pressures in the sulfur hydride system". In: *Nature* 525, pp. 73–76. DOI: `10.1038/nature14964`.

Dunlap, D. H. and V. M. Kenkre (1986). "Dynamic localization of a charged particle moving under the influence of an electric field". In: *Physical Review B* 34, pp. 3625–3633. DOI: `10.1103/PhysRevB.34.3625`.

Fei, Zaiyao et al. (2018). "Ferroelectric switching of a two-dimensional metal". In: *Nature* 560, pp. 336–339. DOI: `10.1038/s41586-018-0336-3`.

Fiebig, Manfred, Victor V. Pavlov, and Roman V. Pisarev (2005). "Second-Harmonic Generation as a Tool for Studying Electronic and Magnetic Structures of Crystals: Review". In: *Journal of the Optical Society of America B* 22, p. 96. DOI: `10.1364/JOSAB.22.000096`.

Görg, Frederik et al. (2018). "Enhancement and sign change of magnetic correlations in a driven quantum many-body system". In: *Nature* 553, pp. 481–485. DOI: `10.1038/nature25135`.

Grasso, V. et al. (1991). "Optical-Absorption Spectra of Crystal-Field Transitions in $MnPS_3$ at Low Temperatures". In: *Physical Review B* 44, pp. 11060–11066. DOI: `10.1103/PhysRevB.44.11060`.

Guarise, M. et al. (2010). "Measurement of magnetic excitations in the two-dimensional antiferromagnetic $Sr_2CuO_2Cl_2$ insulator using resonant x-ray scattering: Evidence for extended interactions". In: *Physical Review Letters* 105, p. 157006. DOI: `10.1103/PhysRevLett.105.157006`.

Harter, J. W. et al. (2015). "High-speed measurement of rotational anisotropy nonlinear optical harmonic generation using position-sensitive detection". In: *Optics Letters* 40, p. 4671. DOI: `10.1364/OL.40.004671`.

Hoegen, A. von et al. (2018). "Probing the interatomic potential of solids with strong-field nonlinear phononics". In: *Nature* 555, pp. 79–82. DOI: `10.1038/nature25484`.

Hübener, Hannes et al. (2017). "Creating stable Floquet–Weyl semimetals by laser-driving of 3D Dirac materials". In: *Nature Communications* 8, p. 13940. DOI: `10.1038/ncomms13940`.

Jiang, Puqing and Heng Ban (2020). "Transient and steady-state temperature rise in three-dimensional anisotropic layered structures in pump-probe thermoreflectance experiments". In: *Journal of Physics D: Applied Physics* 54, p. 035304. DOI: 10.1088/1361-6463/abbd64.

Jin, Feng, Le Wang, et al. (2019). "Raman interrogation of the ferroelectric phase transition in polar metal $LiOsO_3$". In: *Proceedings of the National Academy of Sciences* 116, pp. 20322–20327. DOI: 10.1073/pnas.1908956116.

Jin, Feng, Anmin Zhang, et al. (2016). "Raman phonons in the ferroelectric-like metal $LiOsO_3$". In: *Physical Review B* 93, p. 064303. DOI: 10.1103/PhysRevB.93.064303.

Kampfrath, Tobias et al. (2011). "Coherent terahertz control of antiferromagnetic spin waves". In: *Nature Photonics* 5, pp. 31–34. DOI: 10.1038/nphoton.2010.259.

Kim, Y. J. et al. (2001). "Neutron scattering study of $Sr_2Cu_3O_4Cl_2$". In: *Physical Review B* 64, p. 024435. DOI: 10.1103/PhysRevB.64.024435.

Kimel, A. V. et al. (2005). "Ultrafast non-thermal control of magnetization by instantaneous photomagnetic pulses". In: *Nature* 435, pp. 655–657. DOI: 10.1038/nature03564.

Kirilyuk, Andrei, A. V. Kimel, and Theo Rasing (2010). "Ultrafast optical manipulation of magnetic order". In: *Reviews of Modern Physics* 82, pp. 2731–2784. DOI: 10.1103/RevModPhys.82.2731.

Kitagawa, Takuya et al. (2011). "Transport properties of nonequilibrium systems under the application of light: Photoinduced quantum Hall insulators without Landau levels". In: *Physical Review B* 84, p. 235108. DOI: 10.1103/PhysRevB.84.235108.

Kurosawa, Ko, Shozo Saito, and Yasuo Yamaguchi (1983). "Neutron Diffraction Study on $MnPS_3$ and $FePS_3$". In: *Journal of the Physical Society of Japan* 52, pp. 3919–3926. DOI: 10.1143/JPSJ.52.3919.

Laurita, N. J. et al. (2019). "Evidence for the weakly coupled electron mechanism in an Anderson-Blount polar metal". In: *Nature Communications* 10, p. 3217. DOI: 10.1038/s41467-019-11172-2.

Li, Hongyuan et al. (2021). "Imaging two-dimensional generalized Wigner crystals". In: *Nature* 597, pp. 650–654. DOI: 10.1038/s41586-021-03874-9.

Li, Tingxin et al. (2021). "Continuous Mott transition in semiconductor moiré superlattices". In: *Nature* 597, pp. 350–354. DOI: 10.1038/s41586-021-03853-0.

Liu, H. M. et al. (2015). "Metallic ferroelectricity induced by anisotropic unscreened Coulomb interaction in $LiOsO_3$". In: *Physical Review B* 91, p. 064104. DOI: 10.1103/PhysRevB.91.064104.

Liu, Jianpeng, Kasra Hejazi, and Leon Balents (2018). "Floquet Engineering of Multiorbital Mott Insulators: Applications to Orthorhombic Titanates". In: *Physical Review Letters* 121, p. 107201. DOI: 10.1103/PhysRevLett.121.107201.

Lo Vecchio, I. et al. (2016). "Electronic correlations in the ferroelectric metallic state of $LiOsO_3$". In: *Physical Review B* 93, p. 161113. DOI: 10.1103/PhysRevB.93.161113.

Ma, Qiong et al. (2017). "Direct optical detection of Weyl fermion chirality in a topological semimetal". In: *Nature Physics* 13, pp. 842–847. DOI: 10.1038/nphys4146.

Mashkovich, Evgeny A. et al. (2021). "Terahertz light–driven coupling of antiferromagnetic spins to lattice". In: *Science* 374, pp. 1608–1611. DOI: 10.1126/science.abk1121.

McIver, J. W. et al. (2020). "Light-induced anomalous Hall effect in graphene". In: *Nature Physics* 16, pp. 38–41. DOI: 10.1038/s41567-019-0698-y.

Melnikov, A. V., A. A. Nikulin, and O. A. Aktsipetrov (2003). "Hyper-Rayleigh scattering by inhomogeneous thin films of $Pb_x(Zr_{0.53}Ti_{0.47})O_3$: Disorder effects". In: *Physical Review B* 67, p. 134104. DOI: 10.1103/PhysRevB.67.134104.

Mentink, J. H., K. Balzer, and M. Eckstein (2015). "Ultrafast and Reversible Control of the Exchange Interaction in Mott Insulators". In: *Nature Communications* 6, p. 6708. DOI: 10.1038/ncomms7708.

Mitrano, M. et al. (2016). "Possible light-induced superconductivity in K_3C_60 at high temperature". In: *Nature* 530, pp. 461–464. DOI: 10.1038/nature16522.

Muthukumar, V. N., Roser Valentí, and Claudius Gros (1995). "Microscopic Model of Nonreciprocal Optical Effects in Cr_2O_3". In: *Physical Review Letters* 75, pp. 2766–2769. DOI: 10.1103/PhysRevLett.75.2766.

Nadj-Perge, Stevan et al. (2014). "Observation of Majorana fermions in ferromagnetic atomic chains on a superconductor". In: *Science* 346, pp. 602–607. DOI: 10.1126/science.1259327.

Němec, P. et al. (2018). "Antiferromagnetic opto-spintronics". In: *Nature Physics* 14, pp. 229–241. DOI: 10.1038/s41567-018-0051-x.

Ning, H. et al. (2020). "Signatures of Ultrafast Reversal of Excitonic Order in Ta_2NiSe_5". In: *Physical Review Letters* 125, p. 267602. DOI: 10.1103/PhysRevLett.125.267602.

Nova, T. F. et al. (2019). "Metastable ferroelectricity in optically strained $SrTiO_3$". In: *Science* 364, pp. 1075–1079. DOI: 10.1126/science.aaw4911.

Oka, Takashi and Hideo Aoki (2009). "Photovoltaic Hall Effect in Graphene". In: *Physical Review B* 79, p. 081406. DOI: 10.1103/PhysRevB.79.081406.

Oka, Takashi and Sota Kitamura (2019). "Floquet Engineering of Quantum Materials". In: *Annual Review of Condensed Matter Physics* 10, pp. 387–408. DOI: `10.1146/annurev-conmatphys-031218-013423`.

Orenstein, J. et al. (2021). "Topology and Symmetry of Quantum Materials via Nonlinear Optical Responses". In: *Annual Review of Condensed Matter Physics* 12, pp. 247–272. DOI: `10.1146/annurev-conmatphys-031218-013712`.

Padmanabhan, Haricharan et al. (2018). "Linear and nonlinear optical probe of the ferroelectric-like phase transition in a polar metal, $LiOsO_3$". In: *Applied Physics Letters* 113, p. 122906. DOI: `10.1063/1.5042769`.

Pershan, P. S. (1963). "Nonlinear Optical Properties of Solids: Energy Considerations". In: *Physical Review* 130, pp. 919–929. DOI: `10.1103/PhysRev.130.919`.

Piryatinskaya, V. G. et al. (2012). "Temperature Behavior of the Fundamental Optical Absorption Band in Quasi-Two-Dimensional Crystalline $MnPS_3$". In: *Low Temperature Physics* 38, pp. 870–873. DOI: `10.1063/1.4752090`.

Powell, G. D., J.-F. Wang, and D. E. Aspnes (2002). "Simplified bond-hyperpolarizability model of second harmonic generation". In: *Physical Review B* 65, p. 205320. DOI: `10.1103/PhysRevB.65.205320`.

Pugachev, A. M. et al. (2012). "Broken Local Symmetry in Paraelectric $BaTiO_3$ Proved by Second Harmonic Generation". In: *Physical Review Letters* 108, p. 247601. DOI: `10.1103/PhysRevLett.108.247601`.

Puggioni, Danilo and James M. Rondinelli (2014). "Designing a robustly metallic noncenstrosymmetric ruthenate oxide with large thermopower anisotropy". In: *Nature Communications* 5, p. 3432. DOI: `10.1038/ncomms4432`.

Rees, Dylan et al. (2020). "Helicity-dependent photocurrents in the chiral Weyl semimetal RhSi". In: *Science Advances* 6, eaba0509. DOI: `10.1126/sciadv.aba0509`.

Ron, A., S. Chaudhary, et al. (2020). "Ultrafast Enhancement of Ferromagnetic Spin Exchange Induced by Ligand-to-Metal Charge Transfer". In: *Physical Review Letters* 125, p. 197203. DOI: `10.1103/PhysRevLett.125.197203`.

Ron, A., E. Zoghlin, et al. (2019). "Dimensional crossover in a layered ferromagnet detected by spin correlation driven distortions". In: *Nature Communications* 10, p. 1654. DOI: `10.1038/s41467-019-09663-3`.

Rubio-Marcos, Fernando et al. (2018). "Reversible optical control of macroscopic polarization in ferroelectrics". In: *Nature Photonics* 12, pp. 29–32. DOI: `10.1038/s41566-017-0068-1`.

Rudner, Mark S. and Netanel H. Lindner (2020). "Band Structure Engineering and Non-Equilibrium Dynamics in Floquet Topological Insulators". In: *Nature Review Physics* 2, pp. 229–244. DOI: `10.1038/s42254-020-0170-z`.

Ruzicka, Brian A. et al. (2012). "Second-Harmonic Generation Induced by Electric Currents in GaAs". In: *Physical Review Letters* 108, p. 077403. DOI: `10.1103/PhysRevLett.108.077403`.

Sartorello, Giovanni et al. (2016). "Ultrafast Optical Modulation of Second- and Third-Harmonic Generation from Cut-Disk-Based Metasurfaces". In: *ACS Photonics* 3, pp. 1517–1522. DOI: `10.1021/acsphotonics.6b00108`.

Satoh, Takuya et al. (2007). "Ultrafast Spin and Lattice Dynamics in Antiferromagnetic Cr_2O_3". In: *Physical Review B* 75, p. 155406. DOI: `10.1103/PhysRevB.75.155406`.

Seifert, Urban F. P. and Leon Balents (2019). "Optical excitation of magnons in an easy-plane antiferromagnet: Application to Sr2IrO4". In: *Physical Review B* 100, p. 125161. DOI: `10.1103/PhysRevB.100.125161`.

Sentef, Michael A. et al. (2020). "Quantum to Classical Crossover of Floquet Engineering in Correlated Quantum Systems". In: *Physical Review Research* 2, p. 033033. DOI: `10.1103/PhysRevResearch.2.033033`.

Seyler, Kyle L. et al. (2015). "Electrical Control of Second-Harmonic Generation in a WSe_2 Monolayer Transistor". In: *Nature Nanotechnology* 10, pp. 407–411. DOI: `10.1038/nnano.2015.73`.

Shan, Jun-Yi, A. de la Torre, et al. (2020). "Evidence for an extended critical fluctuation region above the polar ordering transition in $LiOsO_3$". In: *Physical Review Research* 2, p. 033174. DOI: `10.1103/PhysRevResearch.2.033174`.

Shan, Jun-Yi, M. Ye, et al. (2021). "Giant modulation of optical nonlinearity by Floquet engineering". In: *Nature* 600, pp. 235–239. DOI: `10.1038/s41586-021-04051-8`.

Shi, Youguo et al. (2013). "A ferroelectric-like structural transition in a metal". In: *Nature Materials* 12, pp. 1024–1027. DOI: `10.1038/nmat3754`.

Shirley, Jon H. (1965). "Solution of the Schrödinger Equation with a Hamiltonian Periodic in Time". In: *Physical Review* 138, B979–B987. DOI: `10.1103/PhysRev.138.B979`.

Sie, Edbert J., J. W. McIver, et al. (2015). "Valley-Selective Optical Stark Effect in Monolayer WS_2". In: *Nature Materials* 14, pp. 290–294. DOI: `10.1038/nmat4156`.

Sie, Edbert J., Timm Rohwer, et al. (2019). "Time-resolved XUV ARPES with tunable 24–33 eV laser pulses at 30 meV resolution". In: *Nature Communications* 10, p. 3535. DOI: `10.1038/s41467-019-11492-3`.

Sim, Hyunsu and Bog G. Kim (2014). "First-principles study of octahedral tilting and ferroelectric-like transition in metallic $LiOsO_3$". In: *Physical Review B* 89, p. 201107. DOI: `10.1103/PhysRevB.89.201107`.

Sivadas, Nikhil et al. (2015). "Magnetic ground state of semiconducting transition-metal trichalcogenide monolayers". In: *Physical Review B* 91, p. 235425. DOI: 10.1103/PhysRevB.91.235425.

Slater, J. C. (1950). "The Lorentz Correction in Barium Titanate". In: *Physical Review* 78, pp. 748–761. DOI: 10.1103/PhysRev.78.748.

Snider, Elliot et al. (2020). "Room-temperature superconductivity in a carbonaceous sulfur hydride". In: *Nature* 586, pp. 373–377. DOI: 10.1038/s41586-020-2801-z.

Soavi, Giancarlo et al. (2018). "Broadband, Electrically Tunable Third-Harmonic Generation in Graphene". In: *Nature Nanotechnology.* 13, pp. 583–588. DOI: 10.1038/s41565-018-0145-8.

Stanciu, C. D. et al. (2007). "All-Optical Magnetic Recording with Circularly Polarized Light". In: *Physical Review Letters* 99, p. 047601. DOI: 10.1103/PhysRevLett.99.047601.

Terhune, R. W., P. D. Maker, and C. M. Savage (1962). "Optical Harmonic Generation in Calcite". In: *Physical Review Lett.* 8, pp. 404–406. DOI: 10.1103/PhysRevLett.8.404.

Tokunaga, M. (1974). "Range of Validity of Landau Theory in Ferroelectric Critical Phenomena". In: *Progress of Theoretical Physics* 51, pp. 1002–1018. DOI: 10.1143/PTP.51.1002.

Tokunaga, M. and Toshio Mitsui (1976). "Critical phenomena in ferroelectric phase transitions". In: *Ferroelectrics* 11, pp. 451–467. DOI: 10.1080/00150197608237778.

Torchinsky, Darius H. et al. (2014). "A low temperature nonlinear optical rotational anisotropy spectrometer for the determination of crystallographic and electronic symmetries". In: *Review of Scientific Instruments* 85, p. 083102. DOI: 10.1063/1.4891417.

Ukhanov, Yu. I. (1977). *Optical properties of semiconductors*. Moscow: Nauka.

Vigliotti, Franco et al. (2004). "Ultrafast Electron Crystallography of Surface Structural Dynamics with Atomic-Scale Resolution". In: *Angewandte Chemie International Edition* 43, pp. 2705–2709. DOI: 10.1002/anie.200453983.

Wang, Y. H. et al. (2013). "Observation of Floquet-Bloch States on the Surface of a Topological Insulator". In: *Science* 342, pp. 453–457. DOI: 10.1126/science.1239834.

Wildes, A. R. et al. (2006). "Static and Dynamic Critical Properties of the Quasi-Two-Dimensional Antiferromagnet $MnPS_3$". In: *Physical Review B* 74, p. 094422. DOI: 10.1103/PhysRevB.74.094422.

Xiang, H. J. (2014). "Origin of polar distortion in $LiNbO_3$-type "ferroelectric" metals: Role of A-site instability and short-range interactions". In: *Physical Review B* 90, p. 094108. DOI: 10.1103/PhysRevB.90.094108.

Xu, Su-Yang et al. (2020). "Spontaneous gyrotropic electronic order in a transition-metal dichalcogenide". In: *Nature* 578, pp. 545–549. DOI: 10.1038/s41586-020-2011-8.

Yang, Shengyuan A. et al. (2009). "Second harmonic generation from tetragonal centrosymmetric crystals". In: *Physical Review B* 80, p. 165306. DOI: 10.1103/PhysRevB.80.165306.

Zhang, M. Y. et al. (2019). "Light-Induced Subpicosecond Lattice Symmetry Switch in MoTe$_2$". In: *Physical Review X* 9, p. 021036. DOI: 10.1103/PhysRevX.9.021036.

Zhang, Yu et al. (2019). "Doping-Induced Second-Harmonic Generation in Centrosymmetric Graphene from Quadrupole Response". In: *Physical Review Letters* 122, p. 047401. DOI: 10.1103/PhysRevLett.122.047401.

Zhao, Hong Jian et al. (2018). "Meta-screening and permanence of polar distortion in metallized ferroelectrics". In: *Physical Review B* 97, p. 054107. DOI: 10.1103/PhysRevB.97.054107.

Zibold, A. et al. (1996). "Optical properties of single-crystal Sr$_2$CuO$_2$Cl$_2$". In: *Physical Review B* 53, pp. 11734–11743. DOI: 10.1103/PhysRevB.53.11734.

A p p e n d i x   A

AN EXAMPLE OF USING THE BILBAO DATABASE

In this Appendix, we run through procedures for finding the type-1 MD SHG tensor for the magnetic point group m'm'm.

First, we log onto the Bilbao database https://www.cryst.ehu.es/. Since our point group is a magnetic point group, we choose the MTENSOR under "Magnetic symmetry and Applications." (Figure A.1) If our point group is purely crystallographic, we choose the TENSOR under "Solid State Theory Applications."

Magnetic Symmetry and Applications	
MGENPOS	General Positions of Magnetic Space Groups
MWYCKPOS	Wyckoff Positions of Magnetic Space Groups
MKVEC	The k-vector types and Brillouin zones of Magnetic Space Groups
IDENTIFY MAGNETIC GROUP	Identification of a Magnetic Space Group from a set of generators in an arbitrary setting
BNS2OG	Transformation of symmetry operations between BNS and OG settings
mCIF2PCR	Transformation from mCIF to PCR format (FullProf).
MPOINT	Magnetic Point Group Tables
MAGNEXT	Extinction Rules of Magnetic Space Groups
MAXMAGN	Maximal magnetic space groups for a given space group and a propagation vector
MAGMODELIZE	Magnetic structure models for any given magnetic symmetry
STRCONVERT	Convert & Edit Structure Data (supports the CIF, mCIF, VESTA, VASP formats -- with magnetic information where available)
k-SUBGROUPSMAG	Magnetic subgroups consistent with some given propagation vector(s) or a supercell
MAGNDATA	A collection of magnetic structures with portable cif-type files
MVISUALIZE	3D Visualization of magnetic structures with Jmol
MTENSOR ⚠	Symmetry-adapted form of crystal tensors in magnetic phases
MAGNETIC REP.	Decomposition of the magnetic representation into irreps
Get_mirreps	Irreps and order parameters in a paramagnetic space group- magnetic subgroup phase transition

Figure A.1: Bilbao Step 1.

Then, we select "choose it" to select the magnetic point group (Figure A.2). We then select the point group m'm'm (Figure A.3). Note that for other equivalent point groups, including mm'm' and m'mm', we can also select the m'm'm point group here, but we need to manually switch the coordinates later.

Please, enter a magnetic point group or a magnetic space group:

Magnetic Point or Space Group number: [choose it]

Figure A.2: Bilbao Step 2.

Magnetic Point Group Selection

Please select the magnetic point group from the list:

1.1.1. *1*	1.2.2. *11'*	2.1.3. *-1*	2.2.4. *-11'*	2.3.5. *-1'*	3.1.6. *2*	3.2.7. *21'*
3.3.8. *2'*	4.1.9. *m*	4.2.10. *m1'*	4.3.11. *m'*	5.1.12. *2/m*	5.2.13. *2/m1'*	5.3.14. *2'/m*
5.4.15. *2/m'*	5.5.16. *2'/m'*	6.1.17. *222*	6.2.18. *2221'*	6.3.19. *2'2'2*	7.1.20. *mm2*	7.2.21. *mm21'*
7.3.22. *m'm2'*	7.4.23. *m'm'2*	8.1.24. *mmm*	8.2.25. *mmm1'*	8.3.26. *m'mm*	8.4.27. *m'm'm*	8.5.28. *m'm'm'*
9.1.29. *4*	9.2.30. *41'*	9.3.31. *4'*	10.1.32. *-4*	10.2.33. *-41'*	10.3.34. *-4'*	11.1.35. *4/m*
11.2.36. *4/m1'*	11.3.37. *4'/m*	11.4.38. *4/m'*	11.5.39. *4'/m'*	12.1.40. *422*	12.2.41. *4221'*	12.3.42. *4'22*
12.4.43. *42'2'*	13.1.44. *4mm*	13.2.45. *4mm1'*	13.3.46. *4'm'm*	13.4.47. *4m'm'*	14.1.48. *-42m*	14.2.49. *-42m1'*
14.3.50. *-4'2'm*	14.4.51. *-4'2m'*	14.5.52. *-42'm'*	15.1.53. *4/mmm*	15.2.54. *4/mmm1'*	15.3.55. *4/m'mm*	15.4.56. *4'/mm'm*
15.5.57. *4'/m'm'm*	15.6.58. *4/mm'm'*	15.7.59. *4/m'm'm'*	16.1.60. *3*	16.2.61. *31'*	17.1.62. *-3*	17.2.63. *-31'*
17.3.64. *-3'*	18.1.65. *32*	18.2.66. *321'*	18.3.67. *32'*	19.1.68. *3m*	19.2.69. *3m1'*	19.3.70. *3m'*
20.1.71. *-3m*	20.2.72. *-3m1'*	20.3.73. *-3'm*	20.4.74. *-3'm'*	20.5.75. *-3m'*	21.1.76. *6*	21.2.77. *61'*
21.3.78. *6'*	22.1.79. *-6*	22.2.80. *-61'*	22.3.81. *-6'*	23.1.82. *6/m*	23.2.83. *6/m1'*	23.3.84. *6'/m*
23.4.85. *6/m'*	23.5.86. *6'/m'*	24.1.87. *622*	24.2.88. *6221'*	24.3.89. *6'22'*	24.4.90. *62'2'*	25.1.91. *6mm*
25.2.92. *6mm1'*	25.3.93. *6'mm'*	25.4.94. *6m'm'*	26.1.95. *-6m2*	26.2.96. *-6m'2'*	26.3.97. *-6'm'2*	26.4.98. *-6'm2'*
26.5.99. *-6m'2'*	27.1.100. *6/mmm*	27.2.101. *6/mmm1'*	27.3.102. *6'/m'mm*	27.4.103. *6'/mmm'*	27.5.104. *6'/m'm'm*	27.6.105. *6/mm'm'*
27.7.106. *6/m'm'm'*	28.1.107. *23*	28.2.108. *231'*	29.1.109. *m-3*	29.2.110. *m-31'*	29.3.111. *m'-3'*	30.1.112. *432*
30.2.113. *4321'*	30.3.114. *4'32'*	31.1.115. *-43m*	31.2.116. *-43m1'*	31.3.117. *-4'3m'*	32.1.118. *m-3m*	32.2.119. *m-3m1'*
32.3.120. *m'-3'm*	32.4.121. *m-3m'*	32.5.122. *m'-3'm'*				

Figure A.3: Bilbao Step 3.

We then select "Build your own tensor" and enter the Jahn's symbol for the type-1 MD SHG process, V2eV (FigureA.4). If we are looking for the *i*-type tensor, we just enter V2eV. If we are looking for the *c*-type tensor, we add an "a" in front of the Jahn's symbol, which makes it aV2eV. We then select "Get results" to get the final tensor form.

◉ **Build your own tensor**

- Introduce Jahn's symbol without superscripts. Examples: (1) [[V2][V2]], (2) a{V2}*, (3) (V2[V2])*

[aV2eV]

[Get results]

Figure A.4: Bilbao Step 4.

INDEX

POCKET MATERIAL
THE OPTICAL SPECTRUM IN HSIEH LAB:
PHYSICS AND TECHNIQUES

Electromagnetic waves come with a wide range of frequencies, from gamma rays to microwaves. Different frequencies serve different roles in the condensed matter physics research, and require different generation methods and different optical elements for manipulation. Here I would like to make a list for future reference. During my PhD I mainly worked with near/mid infrared and visible lasers, but for completeness, I will also include discussions of ultraviolet and THz. Note that the generation methods discussed here are based on the conditions in Hsieh lab at Caltech (Ti:sapphire laser, e.g., Coherent Astrella, with OPA and DFG extensions, e.g., from Light Conversion).

The Hsieh lab uses ultraviolet pulses to perform time-resolved angle-resolved photoemission spectroscopy (tr-ARPES) measurements in order to overcome the work function of the materials. We generate the fourth harmonic of the 1.55 eV ($\sim$ 800 nm) fundamental output in order to get a photon energy above 6 eV. Depending on the exact photon energy of the fundamental ouput, one would need to choose from either doubling the fundamental frequency twice in order to get the fourth harmonic (e.g., for 808 nm fundamental), or doubling the fundamental once, then mixing the fundamental with the SHG to get THG, then mixing the fundamental and THG to get the fourth harmonic (e.g., for our 797 nm laser). These different approaches are due to the efficiency of the BBO crystal. One would also need to buy different cuts of the BBO crystal for different specific nonlinear processes.

For some of the visible spectrum (580 to 750 nm and 400 nm) we can obtain the colors by doubling either the output from the OPA or the 800 nm fundamental beam using BBO crystals (EKSMA Optics). When the BBO angles are optimized, a conversion efficiency more than 10% can be expected. These wavelengths can correspond to charge transfer transition (photodoping), excitons, or *d-d* transitions in 3*d* Mott or charge-transfer insulators. We used dielectric mirrors (Thorlabs BB1 series) for the visible colors, and chose the broadband coatings based on the actual wavelengths. Note that the BBO-generated beams can have weak but broad tails in the spectrum, so in certain sensitive measurements (like SHG measurements), we used both short-pass and long-pass filters (e.g., Thorlabs FESH1000 and FELH500) after the BBO to select the desired wavelengths. Note that the visible colors seem

more intense than IR beams, so one needs a power meter to measure their actual power.

For 800-nm light we can directly use the fundamental output of the Ti:sapphire laser. If one only needs 800 nm in their experiments and desires better signal-to-noise ratio and shorter data acquisition time, they can use the 80 MHz output from the oscillator. This photon energy ($\sim$ 1.5 eV) corresponds to the band gap of GaAs, a widely used semiconductor. We used standard coated mirrors (Thorlabs BB1-E03) and lenses for 800-nm beams. This wavelength is our go-to wavelength as SHG and reflectivity probes due to its readiness, unless we need to take special considerations.

We generated the near-infrared wavelengths through an OPA pumped by the 800-nm laser. These colors are suitable for photodoping in iridates, pumping zone-boundary magnons in cuprates, and performing sub-gap driving in Floquet experiments. These wavelengths are also good for exciting electrons in metals. Wavelengths from 1150 to 1600 nm are generated as the signal beam and wavelengths from 1600 to 2500 nm are generated as the idler beam. Normally the signal beam is more intense than the idler beam. A 1600/1500 short/long pass filter (Edmund Optics 84-656 and Thorlabs FEL1500) is used to select the signal/idler (though they can also be spatially separated). Normal IR detector cards (Thorlabs VRC2) can view up to 1700 nm and longer wavelengths need liquid crystal detector cards (Thorlabs VRC6S). However, for initial alignment of the idler beam one can tune its wavelength to below 1700 nm for better visibility. We used mirrors with silver coating (Thorlabs PF10-03-P01) for beam steering and specially coated lenses (e.g., Thorlabs N-BK7 -C coated lenses) in order to increase transmission.

Though mid infrared wavelengths can also be generated by an OPA in theory, we used a DFG to generate them (2.5 to 20 μm) for better efficiency. We used the DFG wavelengths in order to access lower-energy magnons and to pump the materials deeper sub-gap in order to avoid multi-photon absorption. Silver mirrors (Thorlabs PF10-03-P01) suffice to reflect DFG beams, but one can also use gold mirrors (Thorlabs PF10-03-M01). We viewed the beams via a liquid crystal detector card (Thorlabs VRC6S). For beam focusing we used lenses of special material (such as BaF$_2$) or off-axis parabolic mirrors (e.g., Thorlabs MPD119-P01). For polarization control we used wire grid polarizers.

We generated THz pulses by shining the 800 nm beam on GaP or ZnTe, through a DFG process. THz spectroscopy can detect phonons, magnons, or the Drude response from free electrons. We used special optics from THz beams—wire grid

polarizers for polarization control, off-axis parabolic mirrors for beam focusing and beam shaping, and silicon for beam splitting.